

NUMERICAL INVESTIGATION OF THE VISCOELASTIC FLUIDS

A THESIS SUBMITTED TO
THE GRADUATE SCHOOL OF NATURAL AND APPLIED SCIENCES
OF
MIDDLE EAST TECHNICAL UNIVERSITY

BY

KERİM YAPICI

IN PARTIAL FULFILLMENT OF THE REQUIREMENTS
FOR
THE DEGREE OF DOCTOR OF PHILOSOPHY
IN
CHEMICAL ENGINEERING

JUNE 2008

Approval of the thesis:

NUMERICAL INVESTIGATION OF THE VISCOELASTIC FLUIDS

submitted by **KERIM YAPICI** in partial fulfillment of the requirements for the degree of
**Doctor of Philosophy in Chemical Engineering Department, Middle East
Technical University** by,

Prof. Dr. Canan Özgen
Dean, Graduate School of **Natural and Applied Sciences**

Prof. Dr. Gürkan Karakaş
Head of Department, **Chemical Engineering**

Assoc. Prof. Dr. Yusuf Uludağ
Supervisor, **Chemical Engineering Dept., METU**

Prof. Dr. Bülent Karasözen
Co-Supervisor, **Mathematics Dept., METU**

Examining Committee Members:

Prof. Dr. Ünver Kaynak
Electrical and Electronic Engineering Dept., TOBB ETU

Assoc. Prof. Dr. Yusuf Uludağ
Chemical Engineering Dept., METU

Assoc. Prof. Dr. Serkan Özgen
Aerospace Engineering Dept., METU

Assoc. Prof. Dr. İsmail Aydın
Civil Engineering Dept., METU

Assoc. Prof. Dr. Göknur Bayram
Chemical Engineering Dept., METU

Date: 20/06/2008

I hereby declare that all information in this document has been obtained and presented in accordance with academic rules and ethical conduct. I also declare that, as required by these rules and conduct, I have fully cited and referenced all material and results that are not original to this work.

Name, Last name: Kerim Yapıcı

Signature :

ABSTRACT

NUMERICAL INVESTIGATION OF THE VISCOELASTIC FLUIDS

Yapıcı, Kerim

Ph.D., Department of Chemical Engineering

Supervisor: Assoc. Prof. Dr. Yusuf Uludağ

Co-Supervisor: Prof. Dr. Bülent Karasözen

June 2008, 136 pages

Most materials used in many industries such as plastic, food, pharmaceuticals, electronics, dye, etc. exhibit viscoelastic properties under their processing or flow conditions. Due to the elasticity of such materials, deformation-stress in addition to their hydrodynamic behavior differ from simple Newtonian fluids in many important respects. Rod climbing, siphoning, secondary flows are all common examples to how a viscoelastic fluid can exhibit quite distinctive flow behavior than a Newtonian fluid would do under similar flow conditions. In industrial processes involving flow of viscoelastic materials, understanding complexities associated with the viscoelasticity can lead to both design and development of hydrodynamically efficient processes and to improved quality of the final products.

In the present study, the main objective is to develop two dimensional finite volume based convergent numerical algorithm for the simulation of viscoelastic flows using nonlinear differential constitutive equations. The constitutive models adopted are Oldroyd-B, Phan-Thien Tanner (PTT) and White-Metzner models. The semi-implicit method for the pressure-linked equation (SIMPLE) and SIMPLE consistent (SIMPLEC) are used to solve the coupled continuity, momentum and constitutive equations. Extra stress terms in momentum

equations are solved by decoupled strategy. The schemes to approximate the convection terms in the momentum equations adopted are first order upwind, hybrid, power-law second order central differences and finally third order quadratic upstream interpolation for convective kinematics QUICK schemes. Upwind and QUICK schemes are used in the constitutive equations for the stresses. Non-uniform collocated grid system is employed to discretize flow geometries. As test cases, three problems are considered: flow in entrance of planar channel, stick-slip and lid driven cavity flow.

Detailed investigation of the flow field is carried out in terms of velocity and stress fields. It is found that range of convergence of numerical solutions is very sensitive to the type of rheological model, Reynolds number and polymer contribution of viscosity as well as mesh refinement. Use of White-Metzner constitutive differential model gives smooth, non oscillatory solutions to much higher Weissenberg number than Oldroyd-B and PTT models. Differences between the behavior of Newtonian and viscoelastic fluids for lid-driven cavity, such as the normal stress effects and secondary eddy formations, are highlighted.

In addition to the viscoelastic flow simulations, steady incompressible Newtonian flow of lid-driven cavity flow at high Reynolds numbers is also solved by finite volume approach. Effect of the solution procedure of pressure correction equation cycles, which is called inner loop, on the solution is discussed in detail and results are compared with the available data in literature.

Keywords: Finite volume method, Collocated grid, Non-linear differential constitutive equations, Viscoelastic fluids, Stick-slip, Lid-driven cavity.

ÖZ

VİSKOELASTİK AKIŞKANLARIN SAYISAL OLARAK İNCELENMESİ

Yapıcı, Kerim

Doktora, Kimya Mühendisliği Bölümü

Tez Yöneticisi: Doç. Dr. Yusuf Uludağ

Yardımcı Tez Yöneticisi: Prof. Dr. Bülent Karasözen

Haziran 2008, 136 sayfa

Endüstride kullanılan birçok malzeme örneğin, plastik, gıda, ilaç, elektronik ve boya gibi, üretim süreci ya da akış koşullar altında viskoelastik özellik gösterirler. Bu malzemelerin, viskoelastik özellik göstermelerinden dolayı, gerilim deformasyonları ayrıca akış hidrodinamiği Newton'su akış özelliği gösteren akışkanlardan birçok yönüyle farklılıklar gösterirler. Tırmanma, "siphoning" ve ikincil akışlar bir viskoelastik sıvının aynı akış koşulları altında Newton'su akışkandan nasıl farklılık gösterdiğini belirten bilinen özelliklerdir. Viskoelastik malzemelerin akışını içeren endüstriyel süreçler içerisinde, elastik özelliklerinden kaynaklanan karmaşık davranışlarını anlamak, daha verimli süreçlerin tasarlanmasını ve geliştirilmesini, son ürün kalitesinin arttırılmasına yardımcı olabilecektir.

Bu çalışmanın temel amacı viskoelastik akışkanların sayısal çözümü için, sonlu hacimler metoduna dayalı, doğrusal olmayan diferansiyel yardımcı eşitlik modellerini kullanan ve iki boyutlu sayısal yöntem geliştirmektir. Yardımcı gerilim eşitlikleri için üç model; Oldroyd-B, Phan-Thien Tanner (PTT) and White-Metzner benimsenmiştir. Birbirleri ile kuvvetli bağlantılı durumdaki süreklilik, hız ve gerilim eşitlikleri "SIMPLE" ve "SIMLEC" algoritması kullanılarak çözümlenmiştir. Süreklilik eşitliklerindeki ilave gerilim terimlerinin birbirleri ile olan bağlantısının giderildiği "decoupled" yöntemi ile çözümlenmiştir. Süreklilik eşitlikleri

içerisindeki konveksiyon terimleri için birinci derece yaklaşım şemaları ("upwind", "hybrid", "power-law"), ikinci derece yaklaşım şeması ("central differences") ve son olarak üçüncü derece yaklaşım şeması ("QUICK") kullanılmıştır. Buna karşın yardımcı eşitlik modellerindeki gerilimler için "upwind" ve "QUICK" şemaları kullanılmıştır. Düzgün aralıklı olmayan ve "collocated" yapıdaki ızgara sistemi akış geometrilerin çözümünde kullanılmıştır. Üç farklı test geometrisi; kanal içerisinde akış, aniden sınır koşullarının değiştiği "stick-slip" ve kapalı kutu içerisinde akış olarak bilinen "lid-driven cavity" ele alınmıştır.

Akış alanının detaylı incelenmesi, hız ve gerilimin dağılımının incelenmesiyle gerçekleştirilmiştir. Sayısal çözümün yakınsama davranışının, reolojik modelin türüne, Reynolds sayısına, polimer katkılı viskoziteye ve ayrıca kontrol hacmi sayısına çok duyarlı olduğu bulunmuştur. Yüksek Weissenberg sayılarında, White-Metzner yardımcı diferansiyel eşitliği kullanıldığında Oldroyd-B ve PTT modellerine göre çok daha düzgün, salınım yapmayan bir çözüm elde edildiği gözlemlenmiştir. "Lid-driven cavity" geometrisinde Newton'su ve viskoelastik akışkanların davranışları arasındaki gerilim ve ikincil girdap oluşumu vb. farklar vurgulanmıştır.

Viskoelastik akış simülasyonlarına ilaveten ayrıca yüksek Reynolds sayılarında sıkıştırılmayan, yatışkın durumda, Newton'su akışkanların çözümünde sonlu hacimler metodu kullanılarak gerçekleştirildi. Basınç düzeltme eşitliği döngü sayısının çözüm üzerine olan etkisi detaylı bir şekilde tartışılarak, elde edilen sonuçlar literatürle karşılaştırıldı.

Anahtar Kelimeler: Sonlu hacimler metodu, "Collocated" ızgara sistemi, Doğrusal olmayan diferansiyel yardımcı eşitlikler, Viskoelastik akışkanlar, Stick-slip, Lid-driven cavity.

To my family, for their love and encouragement...

ACKNOWLEDGMENTS

First of all, I wish to express my sincere gratitude to my supervisor Assoc. Prof. Dr. Yusuf Uludağ for his valuable suggestions and guidance throughout my study. I express sincere appreciation to Prof. Dr. Bülent Karasözen for his guidance and insight through the study.

I am grateful to Prof. Dr. R. J. Phillips and R. L. Powell and other staffs from UC Davis. I am grateful to Salih Obut for his help in the preparation and editing of thesis report.

I would like to acknowledge the financial support provided by the TUBITAK under grant number 105M087 (MAG-HD-17).

Last but not least, I wish to express my deepest thanks to my parents for their great support and patience throughout my all education and to my wife for her encouragement and moral support to me and for being with me all the time.

TABLE OF CONTENTS

| | |
|-----------------------------------------------------------------------------------------------------------------------------------|-------|
| ABSTRACT | iv |
| ÖZ | vi |
| ACKNOWLEDGMENTS | ix |
| TABLE OF CONTENTS | x |
| LIST OF TABLES | xii |
| LIST OF FIGURES | xiii |
| NOMENCLATURE | xviii |
| CHAPTER | |
| 1. INTRODUCTION | 1 |
| 1.1. SCOPE | 1 |
| 1.2. OBJECTIVE of THIS STUDY | 4 |
| 2. GOVERNING EQUATIONS | 5 |
| 2.1. THE OLDROYD-B CONSTITUTIVE EQUATION | 5 |
| 2.2. THE PHAN-THIEN-TANNER (PTT) CONSTITUTIVE EQUATION | 6 |
| 2.3. THE WHITE-METZNER TYPE CONSTITUTIVE EQUATION | 7 |
| 2.4. DIMENSIONLESS FORM OF GOVERNING EQUATIONS | 8 |
| 3. NUMERICAL METHOD | 12 |
| 3.1. FINITE VOLUME FORMULATION | 12 |
| 3.2. DISCRETIZATION OF THE GOVERNING EQUATIONS | 14 |
| 3.2.1. Collocated Grids | 16 |
| 3.2.2. Discretization of Two-Dimensional Momentum Equations | 16 |
| 3.2.3. Discretization Two-Dimensional Constitutive Equations | 22 |
| 3.3. SOLUTION ALGORITHM | 23 |
| 3.4. MOMENTUM INTERPOLATION METHOD (MIM) | 24 |
| 3.5. SIMPLE ALGORITHM FOR COLLOCATED GRID | 27 |
| 3.6. SIMPLE-C ALGORITHM FOR COLLOCATED GRID | 30 |
| 4. SIMULATION OF STEADY LID-DRIVEN CAVITY FLOW AT HIGH REYNOLDS NUMBERS BY FINITE VOLUME APPROACH USING COLLOCATED GRIDS | 32 |
| 4.1 INTRODUCTION | 32 |

| | |
|---------------------------------------------------------------------------------------------|-----|
| 4.2. GOVERNING EQUATIONS AND NUMERICAL METHODOLOGY | 33 |
| 4.3. NUMERICAL RESULTS AND DISCUSSION | 35 |
| 5. RESULTS AND DISCUSSION | 46 |
| 5.1. FLOW IN ENTRANCE OF PLANNER CHANNEL | 46 |
| 5.2. STICK-SLIP FLOW | 56 |
| 5.3. LID DRIVEN CAVITY FLOW | 63 |
| 5.3.1. Boundary Conditions For Stresses | 65 |
| 5.3.2. Results at $Re \ll 1$ | 66 |
| 5.3.3. Results at $Re=100$ | 79 |
| 5.3.4. Results at $Re=400$ | 89 |
| 6. PARTICLE MIGRATION AND SUSPENSION STRUCTURE IN STEADY AND OSCILLATORY CHANNEL FLOW | 99 |
| 6.1. INTRODUCTION | 99 |
| 6.2. A MODEL FOR STRUCTURE, STRESS AND FLOW | 101 |
| 6.2.1 The Migration Model..... | 101 |
| 6.2.2 The SPP Model | 104 |
| 6.3. NUMERICAL SOLUTION | 107 |
| 6.3.1 The MacCormack Method..... | 110 |
| 6.3.2 The Finite Volume Method | 111 |
| 6.4 RESULTS AND DISCUSSION | 112 |
| 7. CONCLUSIONS | 124 |
| REFERENCES | 127 |

LIST OF TABLES

TABLES

| | |
|-------------------------------------------------------------------------------------------------------------------------------------------------------------------|-----|
| Table 3.1. Definition of the constants and function in equation (3.1) for two dimensional flow. | 15 |
| Table 4.1. Intensities of the primary eddies and vorticity and their locations. | 44 |
| Table 4.2. Horizontal minimum velocity, vertical minimum and maximum velocity through the centerlines of the cavity. | 44 |
| Table 4.3. Comparison of the stream function and vorticity values. | 45 |
| Table 5.1. Material parameters used in White-Metzner model..... | 55 |
| Table 5.2. Horizontal minimum velocity, vertical minimum and maximum velocity through the centerlines of the cavity at Re=0. | 75 |
| Table 5.3. Intensities of the primary eddies as a function of Weissenberg number at Re=0. | 76 |
| Table 5.4. Horizontal minimum velocity, vertical minimum and maximum velocity through the centerlines of the cavity with three different mesh at Re=0..... | 79 |
| Table 5.5. Horizontal minimum velocity, vertical minimum and maximum velocity through the centerlines of the cavity at Re=100. | 82 |
| Table 5.6. Intensities of the primary eddies as a function of Weissenberg number at Re=100. | 87 |
| Table 5.7. Horizontal minimum velocity, vertical minimum and maximum velocity through the centerlines of the cavity at Re=400. | 93 |
| Table 5.8. Intensities of the primary eddies as a function of Weissenberg number at Re = 400. | 94 |
| Table 6.1. Values of c_k in equation 6.2.2.6..... | 106 |
| Table 6.2. Values of k_i in equation 6.2.2.8..... | 106 |

LIST OF FIGURES

FIGURES

| | |
|----------------------------------------------------------------------------------------------------------------------------------------------------------------------------|----|
| Figure 3.1. Schematic diagram of a control volume..... | 14 |
| Figure 3.2. Location of the flow variables on non-uniform collocated grids..... | 17 |
| Figure 3.3. Grid points in the x direction..... | 25 |
| Figure 4.1. Square lid-driven cavity geometry with boundary conditions. | 33 |
| Figure 4.2. Non-uniform graded meshes of 257x257 grid points with enlargement view of right top corner. | 36 |
| Figure 4.3. Stream functions at various Reynolds numbers. | 37 |
| Figure 4.4. Vorticity contours at various Reynolds numbers. Contour levels are shown from -10 to 10 with increment of 1..... | 39 |
| Figure 4.5. The pressure contour for various Reynolds numbers..... | 41 |
| Figure 4.6. Profiles of horizontal velocity (u) at vertical centerline (x=0.5)..... | 42 |
| Figure 4.7. Profiles of vertical velocity (v) at horizontal centerline (y=0.5)..... | 43 |
| Figure 5.1. Planar channel flow geometry. | 47 |
| Figure 5.2. Inlet velocity profile. | 47 |
| Figure 5.3. Comparison of the centerline velocity for three different schemes at We=1 and Re<<1 with Oldroyd-B model. | 50 |
| Figure 5.4. Stress components τ_{xx} at the centerline at We=1 and Re<<1 by Oldroyd-B model..... | 50 |
| Figure 5.5. Comparison of computed and analytical profiles of (a) normal and (b) shear stresses near exit of the channel at We=1 and Re<<1 by Oldroyd-B model. | 51 |
| Figure 5.6. Centerline velocity for We=1 and Re=1 with Oldroyd-B model..... | 52 |
| Figure 5.7. Centerline velocity at We=1 and Re=10 with channel length of a) 12H and b) 16H with Oldroyd-B model. | 52 |
| Figure 5.8. Effect of the We on centerline velocity for Re<<1 with PTT model. | 53 |
| Figure 5.9. Computed profiles of (a) normal and (b) shear stresses at near the exit of the channel for Re<<1 at two different We for PTT model..... | 53 |
| Figure 5.10. Centerline velocity profiles between constitutive models Oldroyd-B and PTT at We=1 for Re<<1..... | 54 |

| | |
|---------------------------------------------------------------------------------------------------------------------------------------------------------------------------------------------------------------------------|----|
| Figure 5.11. Effect of the We on centerline velocity for $Re \ll 1$ with White-Metzner model. | 55 |
| Figure 5.12. Profiles of (a) normal and (b) shear stresses near channel exit for $Re \ll 1$ at various We with White-Metzner model. | 55 |
| Figure 5.13. Effect of the constitutive models on predicted centerline velocity profiles at $We=1$ for $Re \ll 1$ | 56 |
| Figure 5.14. Stick-slip flow geometry | 57 |
| Figure 5.15. Velocity profiles along the a) top boundary b) center line at various values of We for $Re \ll 1$ by Oldroyd-B model..... | 58 |
| Figure 5.16. Normal stresses, τ_{xx} , profiles along a) top boundary b) close to top boundary ($y= 0.9923$) at various values of We for $Re \ll 1$ by Oldroyd-B model. | 59 |
| Figure 5.17. Shear stresses, τ_{xy} , profile along top boundary at various values of We for $Re \ll 1$ by Oldroyd-B model. | 59 |
| Figure 5.18. Normal stresses, τ_{xx} , profiles along top boundary using two different uniform mesh M1 and M2 having 66 and 33 grid points in y-direction at $We=1.5$ and $Re \ll 1$ by Oldroyd-B model. | 60 |
| Figure 5.19. Velocity profiles along the a) top boundary b) center line at two values of We for $Re \ll 1$ with PTT model. | 61 |
| Figure 5.20. Profiles of (a) normal and (b) shear stresses along the top boundary for $Re \ll 1$ at two different We with PTT model..... | 61 |
| Figure 5.21. Velocity profile along the a) top boundary b) center line at two values of We for $Re \ll 1$ by White-Metzner model..... | 62 |
| Figure 5.22. Profiles of (a) normal and (b) shear stresses along the top boundary at two We for $Re \ll 1$ using White-Metzner model..... | 63 |
| Figure 5.23. Non-uniform graded meshes with enlargements of right top corner (a) Mesh M1, 129x129 (b) Mesh M2, 193x193 (c) Mesh M3 257x257 grid points. | 64 |
| Figure 5.24. The stream functions at top $w_r = 0.875$, middle $w_r = 0.8$, bottom $w_r = 0.7$, for different We and at $Re = 0$ | 67 |
| Figure 5.25. The vorticity contour a) $w_r = 0.875$, b) $w_r = 0.8$, c) $w_r = 0.7$, for different We and at $Re=0$. Contour levels are shown from -10 to 10 with increment of 1..... | 68 |
| Figure 5.25. The vorticity contour a) $w_r = 0.875$, b) $w_r = 0.8$, c) $w_r = 0.7$, for different We and at $Re=0$. Contour levels are shown from -10 to 10 with increment of 1. (continued) ... | 69 |
| Figure 5.25. The vorticity contour a) $w_r = 0.875$, b) $w_r = 0.8$, c) $w_r = 0.7$, for different We and at $Re=0$. Contour levels are shown from -10 to 10 with increment of 1. (continued) ... | 70 |
| Figure 5.26. Primary vortex center location as a function of We and w_r for $Re=0$ | 71 |

| | |
|------------------------------------------------------------------------------------------------------------------------------------------------------------------------------------------------------------|----|
| Figure 5.27. Effects of We on u at vertical centerline ($x=0.5$) for (a) $w_r = 0.875$ (b) $w_r = 0.8$ (c) $w_r = 0.7$ at $Re=0$ | 72 |
| Figure 5.28. Effects of We on v at horizontal centerline ($y=0.5$) for (a) $w_r = 0.875$ (b) $w_r = 0.8$ (c) $w_r = 0.7$ at $Re=0$ | 73 |
| Figure 5.29. Comparison of the eddy sizes USE and DSE as a function of We in terms of contour level at top $w_r = 0.875$, middle $w_r = 0.8$, bottom $w_r = 0.7$ for $Re=0$ | 74 |
| Figure 5.30. Normal stresses, τ_{xx} , near the downstream ($x=0.9987$) (a) $w_r = 0.875$ (b) $w_r = 0.8$ (c) $w_r = 0.7$ at different We for $Re=0$ | 78 |
| Figure 5.31. Normal stresses, τ_{xx} , stresses near the downstream ($x=0.9987$) for three different meshes at $We=0.8$ and $w_r=0.8$ | 79 |
| Figure 5.32. Effects of We on u at vertical centerline ($x=0.5$) for (a) $w_r = 0.875$ (b) $w_r = 0.8$ (c) $w_r = 0.7$ for $Re=100$ | 80 |
| Figure 5.33. Effects of We on v at horizontal centerline ($y=0.5$) for (a) $w_r = 0.875$ (b) $w_r = 0.8$ (c) $w_r = 0.7$ for $Re=100$ | 81 |
| Figure 5.34. The stream functions at top $w_r = 0.875$, middle $w_r = 0.8$, bottom $w_r = 0.7$, for different We and for $Re=100$ | 84 |
| Figure 5.35. The vorticity contour a) $w_r = 0.875$, b) $w_r = 0.8$, c) $w_r = 0.7$, for different We and at $Re=100$. Contour levels are shown from -10 to 10 with increment of 1..... | 85 |
| Figure 5.35. The vorticity contour a) $w_r = 0.875$, b) $w_r = 0.8$, c) $w_r = 0.7$, for different We and at $Re=100$. Contour levels are shown from -10 to 10 with increment of 1. (continued) | 86 |
| Figure 5.36. Primary vortex center location as a function of We and w_r at $Re=100$ | 88 |
| Figure 5.37. Comparison of the eddy sizes USE and DSE as a function of We in terms of contour level at top $w_r = 0.8$, bottom $w_r = 0.7$ for $Re=100$ | 88 |
| Figure 5.38. Normal stresses, τ_{xx} , near the downstream ($x = 0.9987$) (a) $w_r = 0.875$ (b) $w_r = 0.8$ (c) $w_r = 0.7$ for different We at $Re = 100$ | 89 |
| Figure 5.39. Effects of We on u at vertical centerline ($x = 0.5$) for (a) $w_r = 0.875$ (b) $w_r = 0.8$ (c) $w_r = 0.7$ for $Re = 400$ | 91 |
| Figure 5.40. Effects of We on v at horizontal centerline ($y=0.5$) for (a) $w_r = 0.875$ (b) $w_r = 0.8$ (c) $w_r = 0.7$ for $Re=400$ | 92 |
| Figure 5.41. The stream functions at top $w_r = 0.8$, bottom $w_r = 0.7$, for different We and for $Re = 400$ | 95 |
| Figure 5.42. The vorticity contour a) $w_r = 0.8$, b) $w_r = 0.7$, for different We and at $Re=400$. Contour levels are shown from -10 to 10 with increment of 1..... | 96 |
| Figure 5.43. Primary vortex center location as a function of We and w_r at $Re=400$ | 97 |

| | |
|----------------------------------------------------------------------------------------------------------------------------------------------------------------------------------|-----|
| Figure 5.44. Normal stresses, τ_{xx} , near the downstream ($x = 0.9987$) (a) $wr = 0.875$ (b) $wr = 0.8$ (c) $wr = 0.7$ for different We for $Re = 400$. | 98 |
| Figure 6.1. Profiles of dimensionless diffusion coefficient curve fit obtained from experimental data. | 104 |
| Figure 6.2. 1-D control volume | 112 |
| Figure 6.3. Particle volume fraction versus position at steady state. Data are experimentally measurements reported by Koh et al. [86] and Lyon and Leal [87]. | 114 |
| Figure 6.4. Profiles of predicted dimensionless steady velocity are shown for various ϕ . | 115 |
| Figure 6.5. Profiles of predicted structure component tensors are shown for a) $\zeta_s = \frac{1}{3} tr(\underline{Y})$ b) Y_{12} at steady state for various ϕ . | 115 |
| Figure 6.6. Profiles of predicted are shown dimensionless a) particle contributed stress b) migration flux at steady state for various. | 116 |
| Figure 6.7. Profiles of different initial concentration distributions for $\phi = 0.3$ | 116 |
| Figure 6.8. Effect of the different initial distribution on steady particle concentration profile for $\phi_{bulk} = 0.3$ | 117 |
| Figure 6.9. Short time trace of structure tensors components profiles a) close to the wall b) close to the center for $\phi = 0.4$. | 118 |
| Figure 6.10. Long time trace of structure tensors components profiles a) close to the wall b) close to the center for $\phi = 0.4$. | 118 |
| Figure. 6.11. Concentration profiles after $N=1000$ cycles, with full hydrodynamic dispersion included. | 120 |
| Figure. 6.12. Concentration profiles at average volume fraction, $\phi = 0.4$ after $N=50000$ oscillations. | 121 |
| Figure. 6.13. Concentration profiles at average volume fraction, $\phi = 0.4$ after $N=150000$ oscillations. | 121 |
| Figure. 6.14. Concentration profiles at average volume fraction, $\phi = 0.4$ after $N=200000$ oscillations. | 122 |
| Figure. 6.15. Concentration profiles at average volume fraction, $\phi = 0.4$ for $\hat{\omega} = 250$. | 122 |
| Figure. 6.16. Time step size dependency on the solution for $\hat{\omega} = 250$ after $N=10^5$ cycles. | 123 |

Figure. 6.17. Time averaged values of $\left\langle \hat{\Sigma}_{22}^P \right\rangle$ for $\hat{\omega} = 50$, $\hat{\omega} = 100$ and $\hat{\omega} = 250$ after $N=10^4$ cycles..... 123

NOMENCLATURE

| | |
|---|-------------------------------------------|
| A | Area, m ² |
| D | Deformation tensor |
| f | Interpolation factor |
| H | Characteristic length, m |
| U | Characteristic velocity, ms ⁻¹ |
| u | Horizontal velocity, ms ⁻¹ |
| v | Vertical velocity, ms ⁻¹ |
| V | Volume, m ³ |
| p | Pressure, Pa |
| w | Polymer contribution viscosity |
| x | Rectangular coordinates of x-direction |
| y | Rectangular coordinates of y-direction |

Greek Letters:

| | |
|---------------|-------------------------------------------|
| α | Under-relaxation factor |
| β | Ratio of retardation and relaxation time |
| ρ | Density kgm ⁻³ |
| η | Zero shear rate viscosity |
| ε | Elongation factor |
| Γ | Diffusion coefficient |
| ω | Vorticity |
| ψ | Stream function |
| σ | Material constant for White-Metzner model |
| Φ | Dependent variable |
| λ | Relaxation time |
| τ | Stress tensor |
| Δ | Space step |

Subscripts:

| | |
|---|---------------------------|
| i | i th component |
| j | j th component |

| | |
|------|------------------------------|
| min | Minimum |
| max | Maximum |
| E, e | East face of control volume |
| N, n | North face of control volume |
| S, s | South face of control volume |
| W, w | West face of control volume |

Superscripts:

| | |
|----------|-----------------------------------------|
| 0 | Previous iteration value |
| * | Dimensionless quantity and guess values |
| Δ | Upper convected derivative |
| ' | Correction values |
| T | Transpose |

Abbreviations:

| | |
|---------|------------------------------------------------------------|
| ADI | Alternative Direction Implicit |
| CD | Central Differences scheme |
| CFD | Computation Fluid Dynamics |
| DSE | Down Stream Secondary Eddy |
| FV | Finite Volume |
| MIM | Momentum Interpolation Method |
| NONSOL | Non-Newtonian flow Solver |
| QUICK | Quadratic Upstream Interpolation for convective Kinematics |
| PTT | Phan-Thien-Tanner |
| PISO | Pressure-Implicit with Splitting of Operators |
| Re | Reynolds number |
| S | Source term |
| SIMPLE | Semi-Implicit Method for Pressure Linked Equation |
| SIMPLEC | SIMPLE Consistent |
| SIMPLER | SIMPLE Revised |
| UCM | Upper Convected Maxwell |
| USE | Upstream Secondary Eddy |
| TDMA | Tridiagonal Matrix Algorithm |
| We | Weissenberg number |

CHAPTER 1

INTRODUCTION

1.1. SCOPE

Most materials used in many industries such as plastic, food, pharmaceuticals, electronics, dye, etc. exhibit viscoelastic properties under their processing or flow conditions. Viscoelasticity stems from partial memory of the material on the deformation history fading away over material dependent relaxation time, which is at least comparable to the observed time scales in the flow. Due to the elasticity of such materials, deformation-stress in addition to their hydrodynamic behavior differs from simple Newtonian fluids in many important respects. Rod climbing, siphoning, secondary flows are all common examples to how a viscoelastic fluid can exhibit quite distinctive flow behavior than a Newtonian fluid would do under similar flow conditions. In industrial processes involving flow of viscoelastic materials, understanding complexities associated with the viscoelasticity can lead to both design and development of hydrodynamically efficient processes and improved quality control of the final products. Numbers of experimental techniques have been employed to study influence of the viscoelasticity on the flow kinematics in complicated geometries [1-4].

With the advances in digital computer technology and with the numerical methods of enhanced accuracy, stability, efficiency and robustness, number of studies based on the computer simulation of the viscoelastic flows has steadily increased. Therefore, it has been possible to attack complex viscoelastic flows using computer simulations instead of experiments which can be labor intensive, expensive, hazardous and even impossible to conduct in a laboratory [5].

Computing this type of flow phenomena requires viscoelastic rheological models or constitutive equations that provide relation between stress and material deformation rates [6]. A large number of constitutive equations have been developed to describe the behavior of viscoelastic fluids. Some of the nonlinear differential type equations are Upper Convected

Maxwell (UCM), Oldroyd-B, Phan-Thien Tanner (PTT) and White-Metzner models. These are commonly used in the numerical simulation of complex geometries. So far many researches have been conducted to developed robustness and stable numerical algorithm to solve viscoelastic fluids for moderately large values of Weissenberg number, We , which has introduced main challenge in the simulations. The loss of convergence of numerical simulation at some critical value of Weissenberg number is called in literature as high Weissenberg number problem [7-9]. Most of the previous numerical studies agree with that numerical implementation has been the main cause of failure in iterative solution [8, 10, 11]. Common causes are: extremely large stress components associated with abrupt change of boundary [12-13], use of unsuitable boundary conditions [11], and changing equation characteristic from hyperbolic to elliptic or hyperbolic to parabolic when inertia terms are considerable [14, 15], and constitutive models [8].

So far various numerical techniques have been developed to predict accurately flow kinematics of viscoelastic fluids by using number of rheological models. Finite difference [16-18], finite element [19-20], spectral finite element [21] and finite volume [6, 22-26] techniques have been used in the discretization of the non-linear flow systems. Finite difference method applications are generally restricted to simple geometries. Finite volume approximation of fluid flow systems, on the other hand, can be advantageous in terms of computer space and time requirements as well as in terms of numerical stability compared to the finite element method [26].

Extra stress terms in momentum equations can be handled by coupled or decoupled strategy. Description of both approaches is reported by R.I. Tanner and S-C. Xue [27]. Moreover implementation of decoupled strategy for finite volume method in steady and transient discretization form can be found elsewhere [23, 27]. Most numerical simulations of viscoelastic fluids using finite volume technique are based on staggered grids arrangements [6, 23, 24, 28]. Here pressure and stress components τ_{xx} and τ_{yy} are located at the center of the control volume, while generally τ_{xy} is located on corners and velocities are placed on the faces of the control volume. To avoid checkerboard or zig-zag pressure distribution, staggered grid arrangements are also preferred in Newtonian flow simulations.

The other kind of arrangement is nonstaggered grid in which all flow variables are located at the center of the control volume. These two kinds of grids arrangements are compared in detail by M. Peric et al. [29]. They consider three different test cases; lid driven cavity,

backward facing step and flow through a pipe with sudden contraction involving a Newtonian fluid at low Reynolds numbers. They conclude that in sudden contraction pipe flow problem nonstaggered grids converge faster compared to staggered grids. Moreover, treatment of the boundary conditions and implementation of higher order schemes like QUICK is easier. However, nonstaggered grids produce checkerboard pressure with coarse grid [30]. To overcome this problem, Rhie and Chow [31] first proposed the well known and popular momentum interpolation method (MIM). Although this approach removes the undesired pressure distribution, under-relaxation parameter dependency occurs [32]. Majumdar [32] proposed a new algorithm to overcome this problem. Detailed derivations of the proposed algorithm along with two new momentum interpolation methods are well documented by Yu et al. [33].

Simulations based on finite volume method with nonstaggered grids are also used in the computation of viscoelastic fluids [25, 34-36]. Oliveira et al. [35] performed MIM interpolation method of [31] to remove pressure-velocity-stress decoupling for non-orthogonal grid. Several schemes have been developed and used to approximate the convection term, such as hybrid differencing scheme [37], power-law differencing scheme [38], skew upwind differencing scheme (SUDS) [39], central difference scheme (CD) [40], quadratic upstream interpolation for convective kinematics (QUICK) [41] and sharp and monotonic algorithm for realistic transport (SMART) [42].

Most of the computational studies involving viscoelastic materials consider sudden expansion or contraction flows. Few studies on the lid driven cavity geometry exist in the literature [43-48] even fewer involving viscoelastic flows. Despite its simple geometry, lid driven cavity offers many challenges that are encountered in industrial applications in the form of singularity points, circulations and bifurcations in the flow. Therefore it is highly likely that a numerical methodology efficiently simulating flow of viscoelastic material in this benchmark geometry, may handle complex flows associated with the industrial applications such as agitation.

Grillet et al. [47] used finite element method to analyze stability of the recirculating flows in two dimensional cavity geometry. In order to eliminate the effect of the corner singularities they introduced small leakages in the upstream and downstream corners of the cavity. Setting the amount of leakage was critical due to its strong impact on the stresses and kinematics at the lid corners hence on the entire flow field. Setting the amount the leakage, however, suffers from experimental verification making the value used in the study

ambiguous. They also investigated the effect of the cavity aspect ratio on the flow field and proposed dual elastic instability criterion. They suggested a mechanism for elastic instability based on the convected elastic stresses either from upstream corner to the down stream corner or from downstream corner to the lid bottom depending on the height/length ratio of the cavity.

Fattal and Kupferman [49] employed second order finite difference scheme and converted the algebraic equations into logarithmic form which enabled them to decrease the impact of the Weissenberg instability. Their results, on the other hand, need to be experimentally verified especially at challenging conditions, i.e. at high We .

Pak et al. [4] investigated both laminar and turbulent flow of viscoelastic fluid through a circular pipe with a sudden expansion. They observed that reattachment length for viscoelastic fluids in the laminar regime was shorter than that of Newtonian fluid. On the other hand, in turbulent flow regime, the reattachment length for viscoelastic fluids turned out to be two or three times longer.

The hydrodynamic behavior of viscoelastic fluids in lid driven cavity was also reported in the literature for creeping flow cases. However, the effect of the high Reynolds number on the flow field in the literature is not available to the best knowledge of the author.

1.2. OBJECTIVE of THIS STUDY

In the present study, the main objective is to develop a two dimensional finite volume based convergent numerical algorithm for the simulation of viscoelastic flows using nonlinear differential constitutive equations. The constitutive models adopted are Oldroyd-B, Phan-Thien Tanner (PTT) and White-Metzner models. The semi-implicit method for the pressure-linked equation (SIMPLE) and SIMPLE consistent (SIMPLEC) are used to solve the coupled continuity, momentum and constitutive equations. Extra stress terms in momentum equations are solved by decoupled strategy. The schemes to approximate the convection terms in the momentum equations adopted are first order upwind, hybrid, power-law second order central differences and finally third order quadratic upstream interpolation for convective kinematics QUICK schemes. While upwind and QUICK schemes are used in the constitutive equations for the stresses. Non-uniform collocated grid system is used. As test case, three problems are considered: flow in entrance of planar channel, stick-slip and lid driven cavity flow.

CHAPTER 2

GOVERNING EQUATIONS

It was considered steady, incompressible and isothermal flow of a viscoelastic fluid in the two dimensional Cartesian coordinate system (x,y) . The continuity and momentum equations can be written as follows:

$$\nabla \cdot \mathbf{u} = 0 \quad (2.1)$$

$$\rho \frac{\partial \mathbf{u}}{\partial t} + \rho \mathbf{u} \cdot \nabla \mathbf{u} = -\nabla p + \nabla \cdot \boldsymbol{\tau} + \eta_2 \nabla^2 \mathbf{u} \quad (2.2)$$

Here velocity \mathbf{u} has two components that are u in the x -direction and v in the y -direction. Derivations of differential type constitutive equations which are used in this study are given separately.

2.1. THE OLDROYD-B CONSTITUTIVE EQUATION

The constitutive equation for Oldroyd-B is given by [50, 51],

$$\boldsymbol{\tau} + \lambda_1 \overset{\nabla}{\boldsymbol{\tau}} = 2\eta \left(D + \lambda_2 \overset{\nabla}{D} \right) \quad (2.3)$$

where λ_1 is the material dependent relaxation time, λ_2 is the retardation time, η is the zero shear rate viscosity and $\boldsymbol{\tau}$ is the extra stress tensor. The upper convected derivative of $\overset{\nabla}{\boldsymbol{\tau}}$ is defined by

$$\overset{\nabla}{\boldsymbol{\tau}} = \frac{\partial \boldsymbol{\tau}}{\partial t} + \mathbf{u} \cdot \nabla \boldsymbol{\tau} - \boldsymbol{\tau} \cdot \nabla \mathbf{u} - \nabla \mathbf{u}^T \cdot \boldsymbol{\tau} \quad (2.4)$$

and the rate of deformation tensor D is given by,

$$D = \frac{1}{2}(\nabla \mathbf{u} + \nabla \mathbf{u}^T) \quad (2.5)$$

The stress tensor τ can be decomposed into two parts as follows:

$$\tau = \tau_1 + \tau_2 \quad (2.6)$$

where τ_1 and τ_2 are the non-Newtonian and the Newtonian contributions to τ , respectively, such that

$$\tau_1 + \lambda \overset{\nabla}{\tau}_1 = 2\eta_1 D \quad (2.7)$$

$$\tau_2 = 2\eta_2 D \quad (2.8)$$

where η_1 is the viscosity of the viscoelastic contribution and η_2 is the viscosity of the Newtonian contribution. The relationship between the constants can be expressed as

$$\eta = \eta_1 + \eta_2 \quad (2.9)$$

and

$$\lambda_2 = \frac{\eta_2 \lambda_1}{(\eta_1 + \eta_2)} \quad (2.10)$$

Substitution of eqn. (2.7) into eqn. (2.4) results in the constitutive equation for the Oldroyd-B fluid which is expressed as

$$\tau_1 + \lambda_1 \left(\frac{\partial \tau_1}{\partial t} + \mathbf{u} \cdot \nabla \tau_1 - \nabla \mathbf{u}^T \cdot \tau_1 - \tau_1 \cdot \nabla \mathbf{u} \right) = \eta_1 (\nabla \mathbf{u} + \nabla \mathbf{u}^T) \quad (2.11)$$

2.2. THE PHAN-THIEN-TANNER (PTT) CONSTITUTIVE EQUATION

The constitutive equation Phan-Thien-Tanner (PTT) is given by [52],

$$f(tr(\tau))\tau + \lambda \overset{\nabla}{\tau} = 2\eta D \quad (2.12)$$

where η is the zero shear rate viscosity and τ is the extra stress tensor, λ is the relaxation time and D is the rate of deformation tensor. The upper convected derivative of τ is defined by equation 2.4. The function in equation 2.12 is given by

$$f(tr(\tau)) = 1 + \frac{\varepsilon\lambda}{\eta} tr(\tau) \quad (2.13)$$

where ε is the constant related to the elongational behavior. When ε goes to zero equation (2.12) becomes Oldroyd-B model [53].

2.3. THE WHITE-METZNER TYPE CONSTITUTIVE EQUATION

The constitutive equation of White-Metzner is given by [54, 55],

$$\frac{\tau}{\lambda_H} + (\mathbf{u} \cdot \nabla) \tau + \beta(\tau, \nabla \mathbf{u}) = 2w_r \mu_H D \quad (2.14)$$

where,

$$\beta(\tau, \nabla \mathbf{u}) = 2\varepsilon [D \cdot \tau + \tau \cdot D] - [(\nabla \mathbf{u}) \tau + \tau (\nabla \mathbf{u})^T] \quad (2.15)$$

$$D = \frac{1}{2} (\nabla \mathbf{u} + \nabla \mathbf{u}^T) \quad (2.16)$$

$$\lambda_H = We \frac{\sigma}{[1 + 4\varepsilon(1 - \varepsilon)We^2 \Pi]^\beta}, \quad 0 \leq \beta \leq 1 \quad (2.17)$$

$$We = \frac{\lambda_1 U}{H} \quad (2.18)$$

$$\eta_{II} = \frac{1 + 4\varepsilon(1 - \varepsilon)\lambda_{II}^2 II}{[1 + 4\varepsilon(1 - \varepsilon)We^2 II]^\alpha}, \quad 0 \leq \alpha \leq 1 \quad (2.19)$$

$$II = \frac{1}{2} tr(D^2) = \frac{1}{2} \left[\left(\frac{\partial u}{\partial x} \right)^2 + \left(\frac{\partial v}{\partial y} \right)^2 + \frac{1}{2} \left(\frac{\partial u}{\partial y} + \frac{\partial v}{\partial x} \right)^2 \right] \quad (2.20)$$

$$\mu_{II} = \frac{\eta_{II}}{\lambda_{II}} \quad (2.21)$$

2.4. DIMENSIONLESS FORM OF GOVERNING EQUATIONS

The set of equations which are derived above are converted into their dimensionless form by using the following dimensionless variables.

$$x^* = \frac{x}{H}, y^* = \frac{y}{H}, u^* = \frac{u}{U}, p^* = \frac{pH}{\eta U}, \tau^* = \frac{\tau H}{\eta U} \quad (2.22)$$

where H and U are the characteristic length and velocity in the flow, respectively. In the subsequent sections of the text, quantities without asterisk will be used to express dimensionless quantities for the sake of simplicity.

For a two dimensional system of rectangular coordinates (x,y), the dimensionless steady state problem can be written as:

Continuity

$$\frac{\partial u}{\partial x} + \frac{\partial v}{\partial y} = 0 \quad (2.23)$$

x-momentum

$$\frac{\partial}{\partial x} \left(Re uu - (1 - w_r) \frac{\partial u}{\partial x} \right) + \frac{\partial}{\partial y} \left(Re vu - (1 - w_r) \frac{\partial u}{\partial y} \right) = - \frac{\partial p}{\partial x} + \frac{\partial \tau_{xx}}{\partial x} + \frac{\partial \tau_{xy}}{\partial y} \quad (2.24)$$

y-momentum

$$\begin{aligned} \frac{\partial}{\partial x} \left(\text{Re}uv - (1-w_r) \frac{\partial v}{\partial x} \right) + \frac{\partial}{\partial y} \left(\text{Re}v^2 - (1-w_r) \frac{\partial v}{\partial y} \right) = -\frac{\partial p}{\partial y} \\ + \frac{\partial \tau_{yy}}{\partial y} + \frac{\partial \tau_{xy}}{\partial x} \end{aligned} \quad (2.25)$$

Oldroyd-B constitutive equation:

Stress components of τ_{xx}

$$\begin{aligned} \tau_{xx} + \frac{\partial}{\partial x} (Weu\tau_{xx}) + \frac{\partial}{\partial y} (Wev\tau_{xx}) = We \left(\frac{\partial u}{\partial y} - \frac{\partial v}{\partial x} \right) \tau_{xy} + 2We \frac{\partial u}{\partial x} \tau_{xx} \\ + We \left(\frac{\partial u}{\partial y} + \frac{\partial v}{\partial x} \right) \tau_{xy} + 2w_r \frac{\partial u}{\partial x} \end{aligned} \quad (2.26)$$

Stress components of τ_{yy}

$$\begin{aligned} \tau_{yy} + \frac{\partial}{\partial x} (Weu\tau_{yy}) + \frac{\partial}{\partial y} (Wev\tau_{yy}) = We \left(\frac{\partial v}{\partial x} - \frac{\partial u}{\partial y} \right) \tau_{xy} + 2We \frac{\partial v}{\partial y} \tau_{yy} \\ + We \left(\frac{\partial u}{\partial y} + \frac{\partial v}{\partial x} \right) \tau_{xy} + 2w_r \frac{\partial v}{\partial x} \end{aligned} \quad (2.27)$$

Stress components of τ_{xy}

$$\begin{aligned} \tau_{xy} + \frac{\partial}{\partial x} (Weu\tau_{xy}) + \frac{\partial}{\partial y} (Wev\tau_{xy}) = -\frac{1}{2} We (\tau_{xx} - \tau_{yy}) \left(\frac{\partial u}{\partial y} - \frac{\partial v}{\partial x} \right) \\ + w_r \left(\frac{\partial u}{\partial y} + \frac{\partial v}{\partial x} \right) \\ + \frac{1}{2} We (\tau_{xx} + \tau_{yy}) \left(\frac{\partial u}{\partial y} + \frac{\partial v}{\partial x} \right) \end{aligned} \quad (2.28)$$

The parameter β is the ratio of the retardation and relaxation time and is defined by

$$\beta = \frac{\lambda_2}{\lambda_1} \quad (2.29)$$

$$w_r = 1 - \beta \quad (2.30)$$

The Reynolds number and the Weissenberg number which is defined as the ratio of characteristic fluid relaxation time to characteristic time scale in the flow are given through

$$\text{Re} = \frac{\rho U H}{\eta} \quad (2.31)$$

$$\text{We} = \frac{\lambda_1 U}{H} \quad (2.32)$$

Phan-Thien-Tanner (PTT) constitutive equation:

Stress components of τ_{xx}

$$\begin{aligned} \left(1 + \varepsilon \frac{\text{We}}{w_r} (\tau_{xx} + \tau_{yy})\right) \tau_{xx} + \frac{\partial}{\partial x} (\text{We} u \tau_{xx}) + \frac{\partial}{\partial y} (\text{We} v \tau_{xx}) = \text{We} \left(\frac{\partial u}{\partial y} - \frac{\partial v}{\partial x} \right) \tau_{xy} \\ + 2\text{We} \frac{\partial u}{\partial x} \tau_{xx} + \text{We} \left(\frac{\partial u}{\partial y} + \frac{\partial v}{\partial x} \right) \tau_{xy} + 2w_r \frac{\partial u}{\partial x} \end{aligned} \quad (2.33)$$

Stress components of τ_{yy}

$$\begin{aligned} \left(1 + \varepsilon \frac{\text{We}}{w_r} (\tau_{xx} + \tau_{yy})\right) \tau_{yy} + \frac{\partial}{\partial x} (\text{We} u \tau_{yy}) + \frac{\partial}{\partial y} (\text{We} v \tau_{yy}) = \text{We} \left(\frac{\partial v}{\partial x} - \frac{\partial u}{\partial y} \right) \tau_{xy} \\ + 2\text{We} \frac{\partial v}{\partial y} \tau_{yy} + \text{We} \left(\frac{\partial u}{\partial y} + \frac{\partial v}{\partial x} \right) \tau_{xy} + 2w_r \frac{\partial v}{\partial x} \end{aligned} \quad (2.34)$$

Stress components of τ_{xy}

$$\begin{aligned} \left(1 + \varepsilon \frac{\text{We}}{w_r} (\tau_{xx} + \tau_{yy})\right) \tau_{xy} + \frac{\partial}{\partial x} (\text{We} u \tau_{xy}) + \frac{\partial}{\partial y} (\text{We} v \tau_{xy}) \\ = -\frac{1}{2} \text{We} (\tau_{xx} - \tau_{yy}) \left(\frac{\partial u}{\partial y} - \frac{\partial v}{\partial x} \right) + w_r \left(\frac{\partial u}{\partial y} + \frac{\partial v}{\partial x} \right) \\ + \frac{1}{2} \text{We} (\tau_{xx} + \tau_{yy}) \left(\frac{\partial u}{\partial y} + \frac{\partial v}{\partial x} \right) \end{aligned} \quad (2.35)$$

White-Metzner constitutive equation:Stress components of τ_{xx}

$$\begin{aligned} \frac{\tau_{xx}}{\lambda_{II}} + \frac{\partial}{\partial x}(u\tau_{xx}) + \frac{\partial}{\partial y}(v\tau_{xx}) = -\varepsilon \left[2 \frac{\partial u}{\partial x} \tau_{xx} + \left(\frac{\partial u}{\partial y} + \frac{\partial v}{\partial x} \right) \tau_{xy} \right] \\ + 2 \left[\frac{\partial u}{\partial x} \tau_{xx} + \frac{\partial u}{\partial y} \tau_{xy} \right] + 2 \frac{\eta_{II}}{\lambda_{II}} w_r \frac{\partial u}{\partial x} \end{aligned} \quad (2.36)$$

Stress components of τ_{yy}

$$\begin{aligned} \frac{\tau_{yy}}{\lambda_{II}} + \frac{\partial}{\partial x}(u\tau_{yy}) + \frac{\partial}{\partial y}(v\tau_{yy}) = -\varepsilon \left[2 \frac{\partial v}{\partial y} \tau_{yy} + \left(\frac{\partial u}{\partial y} + \frac{\partial v}{\partial x} \right) \tau_{xy} \right] \\ + 2 \left[\frac{\partial v}{\partial y} \tau_{yy} + \frac{\partial v}{\partial x} \tau_{xy} \right] + 2 \frac{\eta_{II}}{\lambda_{II}} w_r \frac{\partial v}{\partial y} \end{aligned} \quad (2.37)$$

Stress components of τ_{xy}

$$\begin{aligned} \frac{\tau_{xy}}{\lambda_{II}} + \frac{\partial}{\partial x}(u\tau_{xy}) + \frac{\partial}{\partial y}(v\tau_{xy}) = -\varepsilon \left[\frac{1}{2} (\tau_{xx} + \tau_{yy}) \left(\frac{\partial u}{\partial y} + \frac{\partial v}{\partial x} \right) \right] \\ + \left[\frac{\partial v}{\partial x} \tau_{xx} + \frac{\partial u}{\partial y} \tau_{yy} \right] + \frac{\eta_{II}}{\lambda_{II}} w_r \left(\frac{\partial u}{\partial y} + \frac{\partial v}{\partial x} \right) \end{aligned} \quad (2.38)$$

CHAPTER 3

NUMERICAL METHOD

In this section numerical method and tools used in the non-Newtonian flow simulations are explained in detail. Computational Fluid Dynamics (CFD) is a tool for solving conservation equations for mass, momentum, energy and other rheological models or constitutive equations that provide relation between stress and material deformation rates [6]. With the advances in computer speed and memory, number of studies based on computer simulation has steadily increased.

3.1. FINITE VOLUME FORMULATION

Finite Volume (FV) method uses the integral form of the conservation equations, which are discretized over the control volumes. Here the discretization of the governing set of PDEs derived in the previous chapter is outlined. The momentum equations of viscoelastic equations contain both hyperbolic terms (the convection term) and elliptic terms (the diffusion terms) and their relative impact on the momentum equation depends on the Reynolds number [6]. If the convection terms are dominant, momentum equations behave in a hyperbolic manner. Conversely, if diffusion terms are dominant momentum equations behave in elliptic manner. Viscoelastic constitutive equations include only hyperbolic terms and they introduce further complications to the simulation [6]. The nature of conservation equations and possible changes in type is reported by Gaidos and Darby [20]. They concluded that type classification depend on the solution to flow problem so that possible change in type to be cause of numerical instabilities and convergence difficulties.

So far various numerical techniques have been developed to accurately predict flow kinematics of viscoelastic fluids by using number of rheological models. Finite difference [16-18], finite element [19-20], spectral finite element [21] and finite volume [6, 22-26] techniques have been used in the discretization of the non-linear flow systems. Finite

difference method applications are generally restricted to simple geometries. Finite volume approximation of fluid flow systems, on the other hand, can be advantageous in terms of computer space and time requirements as well as in terms of numerical stability compared to the finite element method [26]. In this study finite volume formulation [38, 56] is preferred due to above mentioned advantages.

Continuity, momentum and constitutive equations can be written in the general form as follows:

$$\frac{\partial}{\partial x} \left(\Lambda u \phi - \Gamma \frac{\partial \phi}{\partial x} \right) + \frac{\partial}{\partial y} \left(\Lambda u \phi - \Gamma \frac{\partial \phi}{\partial y} \right) = S_\phi \quad (3.1)$$

where Λ is either density ρ or relaxation time λ , depending on the conservation or constitutive equation; ϕ is one of the dependent variables; Γ is the diffusion coefficient and S_ϕ is the source term. Corresponding dimensionless quantities of these variables are listed in Table 3.1.

Integrating equation (3.1) over a control volume shown in Figure 3.1, the following equation can be obtained

$$\int_V \frac{\partial}{\partial x} \left(\Lambda u \phi - \Gamma \frac{\partial \phi}{\partial x} \right) dV + \int_V \frac{\partial}{\partial y} \left(\Lambda u \phi - \Gamma \frac{\partial \phi}{\partial y} \right) dV = \int_V S_\phi dV \quad (3.2)$$

Using the divergence theorem

$$\int_A \frac{\partial}{\partial x} \left(\Lambda u \phi - \Gamma \frac{\partial \phi}{\partial x} \right) \cdot \underline{n} dA + \int_A \frac{\partial}{\partial y} \left(\Lambda u \phi - \Gamma \frac{\partial \phi}{\partial y} \right) \cdot \underline{n} dA = \int_V S_\phi dV \quad (3.3)$$

where A is the surface enclosing volume V, and \underline{n} is the unit vector normal to the surface.

Integration equation (3.3) gives

$$\begin{aligned} & \left\{ [(\Lambda u \phi A)_e - (\Lambda u \phi A)_w] - \left[\Gamma_e A_e \left(\frac{\partial \phi}{\partial x} \right)_e - \Gamma_w A_w \left(\frac{\partial \phi}{\partial x} \right)_w \right] \right\} \\ & + \left\{ [(\Lambda u \phi A)_n - (\Lambda u \phi A)_s] - \left[\Gamma_n A_n \left(\frac{\partial \phi}{\partial x} \right)_n - \Gamma_s A_s \left(\frac{\partial \phi}{\partial x} \right)_s \right] \right\} = S_\phi \Delta V \end{aligned} \quad (3.4)$$

where each quantity in the brackets is calculated on the corresponding face of the control volume.

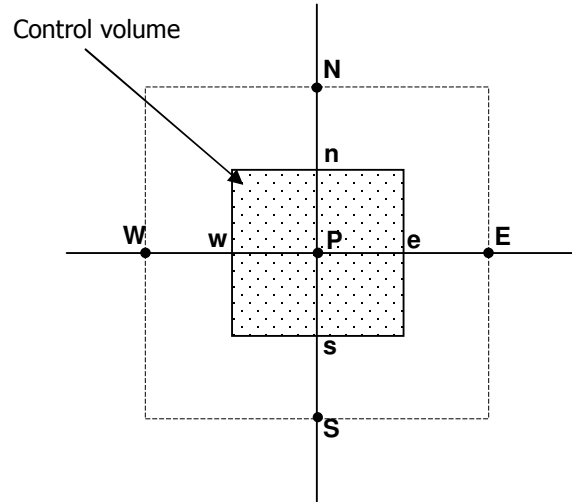


Figure 3.1. Schematic diagram of a control volume

3.2. DISCRETIZATION OF THE GOVERNING EQUATIONS

Equation (3.4) contains both diffusion and convective terms. Central difference scheme is used for the approximation of the gradients which are diffusion terms, in equation (3.4).

Several schemes have been developed and used to approximate the convection terms, such as first order upwind differencing scheme [57], hybrid differencing scheme [37], power-law differencing scheme [38], second order central difference scheme (CD) [40] and third order with uniform grid; quadratic upstream interpolation for convective kinematics (QUICK) [41]. In our calculations, all of these schemes are employed for the discretization of convective terms in the momentum equations. Upwind differencing scheme and QUICK are used in the constitutive equations for the stresses.

Table 3.1. Definition of the constants and function in equation (3.1) for two dimensional flow.

| Equation | Λ | Γ | S_ϕ |
|---------------------------|-----------|--------------|---------------------------------------------------------------------------------------------------------------------------------------------------------------------------------------------------------------------------------------------------------------------------------------------------------------------------------------------------------------------------------------------------------------|
| Continuity | 1 | 0 | 0 |
| u-momentum | Re | $1-\omega_r$ | $-\frac{\partial p}{\partial x} + \frac{\partial \tau_{xx}}{\partial x} + \frac{\partial \tau_{xy}}{\partial y}$ |
| v-momentum | Re | $1-\omega_r$ | $-\frac{\partial p}{\partial y} + \frac{\partial \tau_{yy}}{\partial y} + \frac{\partial \tau_{xy}}{\partial x}$ |
| Oldroyd-B [58] | | | |
| Normal stress T_{xx} | We | 0 | $We \left(\frac{\partial u}{\partial y} - \frac{\partial v}{\partial x} \right) \tau_{xy} + 2We \frac{\partial u}{\partial x} \tau_{xx} + We \left(\frac{\partial u}{\partial y} + \frac{\partial v}{\partial x} \right) \tau_{xy} + 2w_r \frac{\partial u}{\partial x} - \tau_{xx}$ |
| Normal stress T_{yy} | We | 0 | $We \left(\frac{\partial v}{\partial x} - \frac{\partial u}{\partial y} \right) \tau_{xy} + 2We \frac{\partial v}{\partial y} \tau_{yy} + We \left(\frac{\partial u}{\partial y} + \frac{\partial v}{\partial x} \right) \tau_{xy} + 2w_r \frac{\partial v}{\partial x} - \tau_{yy}$ |
| Shear stress T_{xy} | We | 0 | $-\frac{1}{2}We(\tau_{xx} - \tau_{yy}) \left(\frac{\partial u}{\partial y} - \frac{\partial v}{\partial x} \right) + w_r \left(\frac{\partial u}{\partial y} + \frac{\partial v}{\partial x} \right) + \frac{1}{2}We(\tau_{xx} + \tau_{yy}) \left(\frac{\partial u}{\partial y} + \frac{\partial v}{\partial x} \right) - \tau_{xy}$ |
| PTT [28] | | | |
| Normal stress T_{xx} | We | 0 | $We \left(\frac{\partial u}{\partial y} - \frac{\partial v}{\partial x} \right) \tau_{xy} + 2We \frac{\partial u}{\partial x} \tau_{xx} + We \left(\frac{\partial u}{\partial y} + \frac{\partial v}{\partial x} \right) \tau_{xy} + 2w_r \frac{\partial u}{\partial x} - \left(1 + \varepsilon \frac{We}{w_r} (\tau_{xx} + \tau_{yy}) \right) \tau_{xx}$ |
| Normal stress T_{yy} | We | 0 | $We \left(\frac{\partial v}{\partial x} - \frac{\partial u}{\partial y} \right) \tau_{xy} + 2We \frac{\partial v}{\partial y} \tau_{yy} + We \left(\frac{\partial u}{\partial y} + \frac{\partial v}{\partial x} \right) \tau_{xy} + 2w_r \frac{\partial v}{\partial x} - \left(1 + \varepsilon \frac{We}{w_r} (\tau_{xx} + \tau_{yy}) \right) \tau_{yy}$ |
| Shear stress T_{xy} | We | 0 | $-\frac{1}{2}We(\tau_{xx} - \tau_{yy}) \left(\frac{\partial u}{\partial y} - \frac{\partial v}{\partial x} \right) + w_r \left(\frac{\partial u}{\partial y} + \frac{\partial v}{\partial x} \right) + \frac{1}{2}We(\tau_{xx} + \tau_{yy}) \left(\frac{\partial u}{\partial y} + \frac{\partial v}{\partial x} \right) - \left(1 + \varepsilon \frac{We}{w_r} (\tau_{xx} + \tau_{yy}) \right) \tau_{xy}$ |
| White-Metzner [55] | | | |
| Normal stress T_{xx} | 1 | 0 | $-\frac{\tau_{xx}}{\lambda_{II}} - \varepsilon \left[2 \frac{\partial u}{\partial x} \tau_{xx} + \left(\frac{\partial u}{\partial y} + \frac{\partial v}{\partial x} \right) \tau_{xy} \right] + 2 \left[\frac{\partial u}{\partial x} \tau_{xx} + \frac{\partial u}{\partial y} \tau_{xy} \right] + 2 \frac{\eta_{II}}{\lambda_{II}} w_r \frac{\partial u}{\partial x}$ |
| Normal stress T_{yy} | 1 | 0 | $-\frac{\tau_{yy}}{\lambda_{II}} - \varepsilon \left[2 \frac{\partial v}{\partial y} \tau_{yy} + \left(\frac{\partial u}{\partial y} + \frac{\partial v}{\partial x} \right) \tau_{xy} \right] + 2 \left[\frac{\partial v}{\partial y} \tau_{yy} + \frac{\partial v}{\partial x} \tau_{xy} \right] + 2 \frac{\eta_{II}}{\lambda_{II}} w_r \frac{\partial v}{\partial y}$ |
| Shear stress T_{xy} | 1 | 0 | $-\frac{\tau_{xy}}{\lambda_{II}} - \varepsilon \left[\frac{1}{2} (\tau_{xx} + \tau_{yy}) \left(\frac{\partial u}{\partial y} + \frac{\partial v}{\partial x} \right) \right] + \left[\frac{\partial v}{\partial x} \tau_{xx} + \frac{\partial u}{\partial y} \tau_{yy} \right] + \frac{\eta_{II}}{\lambda_{II}} w_r \left(\frac{\partial u}{\partial y} + \frac{\partial v}{\partial x} \right)$ |

3.2.1. Collocated Grids

There are two kinds of grid arrangements used in CFD; staggered grids and nonstaggered or collocated grids. In staggered grid arrangements stress components τ_{xx} and τ_{yy} are located at the center of the control volume, while generally τ_{xy} is located at corners and velocities are placed on the faces of the control volume. Whereas in collocated grids, all flow variables are located at the center of the control volumes as shown in Figure 3.2. It was used non-uniform collocated grid arrangements to discretize the governing sets of equations in the computing domain. It was preferred collocated arrangements because of the some obvious advantages over the staggered grids as reported by Peric et al. [29]. They compared these two types of grid arrangements by performing three test cases involving a Newtonian fluid; lid driven cavity, backward facing step and flow through a pipe with sudden contraction. Some advantages of collocated grids are listed as follows [29]: (a) because all variables stored at the same location, the coefficients in the discretization equations are identical for all velocities. The stress coefficients in the equations are also the same. This feature reduces computer time and required memory when higher order schemes like QUICK discretization method are employed in both Newtonian and viscoelastic flow simulations. (b) Treatment of the boundary conditions is also easy. (c) Implementation of the multigrid method is simpler than that of staggered since the same interpolation is used for all variables. Therefore collocated grids have been used in many studies for computation of viscoelastic fluids [25, 34-36].

3.2.2. Discretization of Two-Dimensional Momentum Equations

Central difference scheme is used for the approximation of the gradients in equation (3.4) which is associated with the diffusion term. We can write expressions for diffusion fluxes through control volume surfaces in the following form (see Figure 3.1):

$$\text{East face} \quad \Gamma_e A_e \left(\frac{\partial \phi}{\partial x} \right)_e = \frac{(1-w_r)}{(x_E - x_P)} (\phi_E - \phi_P)(y_n - y_s) \quad (3.5)$$

$$\text{West Face} \quad \Gamma_w A_w \left(\frac{\partial \phi}{\partial x} \right)_w = \frac{(1-w_r)}{(x_P - x_W)} (\phi_P - \phi_W)(y_n - y_s) \quad (3.6)$$

$$\text{North Face} \quad \Gamma_n A_n \left(\frac{\partial \phi}{\partial x} \right)_n = \frac{(1-w_r)}{(y_N - y_P)} (\phi_N - \phi_P) (x_e - x_w) \quad (3.7)$$

$$\text{South Face} \quad \Gamma_s A_s \left(\frac{\partial \phi}{\partial x} \right)_s = \frac{(1-w_r)}{(y_P - y_S)} (\phi_P - \phi_S) (x_e - x_w) \quad (3.8)$$

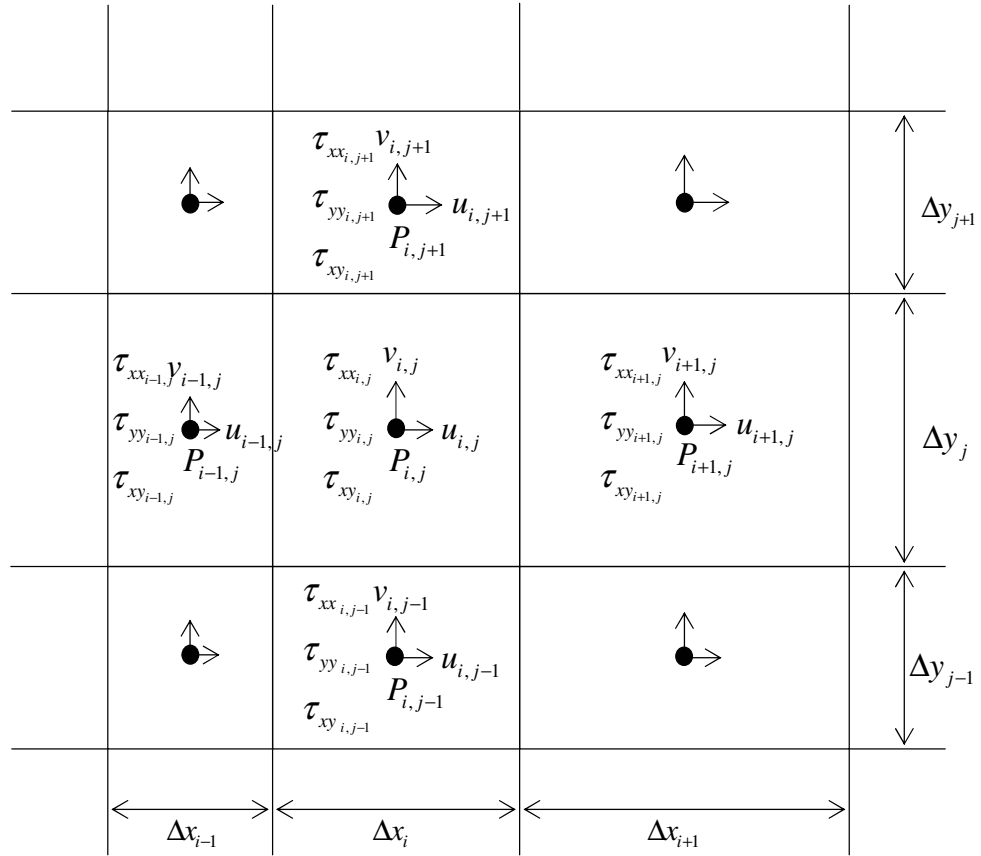


Figure 3.2. Location of the flow variables on non-uniform collocated grids

Here for the sake of convenience, constant coefficients in diffusive fluxes are grouped as:

$$D_e = \frac{(1-w_r)}{(x_E - x_P)}(y_n - y_s) \quad D_w = \frac{(1-w_r)}{(x_P - x_W)}(y_n - y_s) \quad (3.9)$$

$$D_n = \frac{(1-w_r)}{(y_N - x_P)}(x_e - x_w) \quad D_s = \frac{(1-w_r)}{(y_P - y_S)}(x_e - x_w) \quad (3.10)$$

In this study we used several first and high order schemes to discretize convective part in the momentum equations. The details of the central difference scheme as follows. First we establish a new symbol for the convective terms in equation (3.4) as follows:

$$F_e = \text{Re} u_e A_e \quad F_w = \text{Re} u_w A_w \quad (3.11)$$

$$F_n = \text{Re} u_n A_n \quad F_s = \text{Re} u_s A_s \quad (3.12)$$

Equations from (3.5) to (3.8) are inserted in to the equations (3.4) to yield the convection-diffusion equations:

$$\begin{aligned} & \{[F_e \phi_e - F_w \phi_w] - [D_e(\phi_E - \phi_P) - D_w(\phi_P - \phi_W)]\} \\ & + \{[F_n \phi_n - F_s \phi_s] - [D_n(\phi_N - \phi_P) - D_s(\phi_P - \phi_S)]\} = S_\phi \Delta V \end{aligned} \quad (3.13)$$

In equation (3.13) face values of the transported properties are approximated by central difference scheme.

$$\phi_e = f_e \phi_E + (1 - f_e) \phi_P \quad (3.14)$$

$$\phi_n = f_n \phi_N + (1 - f_n) \phi_P \quad (3.15)$$

where f_e, f_w, f_n and f_s , are linear interpolation factors that are defined as

$$f_e = \frac{x_e - x_P}{x_E - x_P} \quad f_w = \frac{x_w - x_W}{x_P - x_W} \quad (3.16)$$

$$f_n = \frac{x_n - x_P}{x_N - x_P} \quad f_s = \frac{x_s - x_S}{x_P - x_S} \quad (3.17)$$

When the expressions (3.14) and (3.15) are substituted into equations (3.13) following expression can be obtained.

$$\begin{aligned}
& F_e[f_e\phi_E + (1-f_e)\phi_P] - F_w[f_w\phi_P + (1-f_w)\phi_W] \\
& - D_e[(\phi_E - \phi_P)] + D_w[(\phi_P - \phi_W)] \\
& + F_n[f_n\phi_N + (1-f_n)\phi_P] - F_s[f_s\phi_P + (1-f_s)\phi_S] \\
& - D_n[(\phi_N - \phi_P)] + D_s[(\phi_P - \phi_S)] = S_\phi\Delta V
\end{aligned} \tag{3.18}$$

We rearrange equation (3.18) to the form

$$\begin{aligned}
& \phi_P[(1-f_e)F_e - f_wF_w + D_e + D_w + (1-f_n)F_n - f_sF_s + D_n + D_n] = \\
& + \phi_E[-f_eF_e + D_e] + \phi_W[(1-f_w)F_w] \\
& + \phi_N[-f_nF_n + D_n] + \phi_S[(1-f_s)F_s] \\
& + S_\phi\Delta V
\end{aligned} \tag{3.19}$$

The next step is to solve the set of algebraic equations which are non-linear due to the source term in the constitutive equations. To make the equations linear, first, source term S_ϕ is assumed to be a linear function of variable ϕ such that,

$$S_\phi = S_C + S_P\phi_P \tag{3.20}$$

where S_C is constant part of the S_ϕ that is independent of ϕ while S_P is the coefficient of ϕ_P which is set as negative to enhance the numerical stability [38].

The final form of the two dimensional discretized governing equation (see 3.19) over the control volume can be expressed symbolically as follows:

$$A_P\phi_P = A_E\phi_E + A_W\phi_W + A_N\phi_N + A_S\phi_S + b \tag{3.21}$$

Discretized form of the x-momentum equation is considered as

$$A_P u_{i,j} = A_E u_{i+1,j} + A_W u_{i-1,j} + A_N u_{i,j+1} + A_S u_{i,j-1} + b u_{i,j} \tag{3.22}$$

where the coefficients are expressed through the following relations in the case of central differences scheme

$$A_E = -f_e F_e + D_e \tag{3.23}$$

$$A_W = (1 - f_w)F_w + D_w \quad (3.24)$$

$$A_N = -f_n F_n + D_n \quad (3.25)$$

$$A_S = (1 - f_s)F_s + D_s \quad (3.26)$$

$$A_p = [A_E + A_W + A_N + A_S + (F_e - F_w) + (F_n - F_s)] / \alpha_u \quad (3.27)$$

Convective terms are

$$F_e = \text{Re} [f_e u_{i+1,j} + (1 - f_e) u_{i,j}] \Delta y_j \quad (3.28)$$

$$F_w = \text{Re} [f_w u_{i,j} + (1 - f_w) u_{i-1,j}] \Delta y_j \quad (3.29)$$

$$F_n = \text{Re} [f_n v_{i,j+1} + (1 - f_n) v_{i,j}] \Delta x_i \quad (3.30)$$

$$F_s = \text{Re} [f_s v_{i,j} + (1 - f_s) v_{i,j-1}] \Delta x_i \quad (3.31)$$

Because of the sharing the same location of the control volume, coefficients of the y-momentum equations are identical to x-momentum equations.

Source terms of the x and y-momentum are

$$b u_{i,j} = -\frac{dp}{dx} \Big|_{i,j} \Delta x_i \Delta y_j + \frac{d\tau_{xx}}{dx} \Big|_{i,j} \Delta x_i \Delta y_j + \frac{d\tau_{xy}}{dy} \Big|_{i,j} \Delta x_i \Delta y_j + (1 - \alpha_u) A_p u_{i,j}^0 \quad (3.32)$$

$$b v_{i,j} = -\frac{dp}{dy} \Big|_{i,j} \Delta x_i \Delta y_j + \frac{d\tau_{yy}}{dy} \Big|_{i,j} \Delta x_i \Delta y_j + \frac{d\tau_{xy}}{dx} \Big|_{i,j} \Delta x_i \Delta y_j + (1 - \alpha_v) A_p v_{i,j}^0 \quad (3.33)$$

where superscript 0 denotes the values obtained at previous iteration. Here, under-relaxation factors α_u and α_v are introduced implicitly in equations (3.27), (3.32) and (3.33) to the x and y-momentum equations respectively. Furthermore, gradients of the

pressure and stresses should be evaluated at the location (i,j). These gradients are obtained by linear interpolation.

$$-\left. \frac{dp}{dx} \right|_{i,j} = \frac{[f_w p_{i,j} + (1-f_w) p_{i-1,j}] - [f_e p_{i+1,j} + (1-f_e) p_{i,j}]}{\Delta x_i} \quad (3.34)$$

$$-\left. \frac{dp}{dy} \right|_{i,j} = \frac{[f_s p_{i,j} + (1-f_s) p_{i,j-1}] - [f_n p_{i,j+1} + (1-f_n) p_{i,j}]}{\Delta y_j} \quad (3.35)$$

$$\left. \frac{d\tau_{xx}}{dx} \right|_{i,j} = \frac{[f_e \tau_{xy_{i+1,j}} + (1-f_e) \tau_{xx_{i,j}}] - [f_w \tau_{xx_{i,j}} + (1-f_w) \tau_{xx_{i-1,j}}]}{\Delta x_i} \quad (3.36)$$

$$\left. \frac{d\tau_{xy}}{dy} \right|_{i,j} = \frac{[f_n \tau_{xy_{i,j+1}} + (1-f_n) \tau_{xy_{i,j}}] - [f_s \tau_{xy_{i,j}} + (1-f_s) \tau_{xy_{i,j-1}}]}{\Delta y_j} \quad (3.37)$$

$$\left. \frac{d\tau_{yy}}{dy} \right|_{i,j} = \frac{[f_n \tau_{yy_{i,j+1}} + (1-f_n) \tau_{yy_{i,j}}] - [f_s \tau_{yy_{i,j}} + (1-f_s) \tau_{yy_{i,j-1}}]}{\Delta y_j} \quad (3.38)$$

$$\left. \frac{d\tau_{xy}}{dx} \right|_{i,j} = \frac{[f_e \tau_{xy_{i+1,j}} + (1-f_e) \tau_{xy_{i,j}}] - [f_w \tau_{xy_{i,j}} + (1-f_w) \tau_{xy_{i-1,j}}]}{\Delta x_i} \quad (3.39)$$

Aforementioned discretized two dimensional momentum equations are written for interior nodal points. Boundary nodes, however, require special treatment [56]. In collocated grid arrangement, to eliminate checkerboard pressure distribution, cell face velocities are evaluated by momentum interpolation method (MIM) suggested by Majumdar [32]. MIM was first proposed by Rhio and Chow [31]. Detailed procedure of the original MIM and two new interpolation methods, called MMIM1 and MMIM2 were well documented by Yu et al. [33].

3.2.3. Discretization Two-Dimensional Constitutive Equations

Upwind differencing and QUICK schemes are used in the constitutive equations for the stresses. Here an Oldroyd-B constitutive equation is discretised in detail by using upwind scheme. The final form of the two dimensional discretised model equations over the control volume can be expressed symbolically as follows:

$$A_P \phi_P = A_E \phi_E + A_W \phi_W + A_N \phi_N + A_S \phi_S + b \quad (3.40)$$

Discretized form of the τ_{xx} equation is considered as

$$A_P \tau_{xxi,j} = A_E \tau_{xxi+1,j} + A_W \tau_{xxi-1,j} + A_N \tau_{xxi,j+1} + A_S \tau_{xxi,j-1} + b \tau_{xxi,j} \quad (3.41)$$

where the coefficients are expressed through following relations in the case of upwind differencing scheme as:

$$A_E = \max[-F_e, 0] \quad A_W = \max[F_w, 0] \quad (3.42)$$

$$A_N = \max[-F_n, 0] \quad A_S = \max[F_s, 0] \quad (3.43)$$

where convective terms are

$$F_e = We [f_e u_{i+1,j} + (1 - f_e) u_{i,j}] \Delta y_j \quad (3.44)$$

$$F_w = We [f_w u_{i,j} + (1 - f_w) u_{i-1,j}] \Delta y_j \quad (3.45)$$

$$F_n = We [f_n v_{i,j+1} + (1 - f_n) v_{i,j}] \Delta x_i \quad (3.46)$$

$$F_s = We [f_s v_{i,j} + (1 - f_s) v_{i,j-1}] \Delta x_i \quad (3.47)$$

$$A_P = [A_E + A_W + A_N + A_S + (F_e - F_w) + (F_n - F_s)] / \alpha_\tau + \Delta x_i \Delta y_j \quad (3.48)$$

Because of the sharing the same location of the control volume, coefficients of the τ_{yy} and

τ_{xy} equations are identical to τ_{xx} equation.

Source term of τ_{xx} equations:

$$\begin{aligned}
b\tau_{xx}|_{i,j} &= 2We \frac{\partial u}{\partial y} \tau_{xy}^0 \Big|_{i,j} \Delta x_i \Delta y_j + 2We \frac{\partial u}{\partial x} \tau_{xx}^0 \Big|_{i,j} \Delta x_i \Delta y_j \\
&+ 2w_r \frac{\partial u}{\partial x} \Big|_{i,j} \Delta x_i \Delta y_j + (1 - \alpha_\tau) A_p \tau_{xxi,j}^0
\end{aligned} \tag{3.49}$$

Source term of τ_{yy} equations:

$$\begin{aligned}
b\tau_{yy}|_{i,j} &= 2We \frac{\partial v}{\partial x} \tau_{xy}^0 \Big|_{i,j} \Delta x_i \Delta y_j + 2We \frac{\partial v}{\partial y} \tau_{yy}^0 \Big|_{i,j} \Delta x_i \Delta y_j \\
&+ 2w_r \frac{\partial v}{\partial x} \Big|_{i,j} \Delta x_i \Delta y_j + (1 - \alpha_\tau) A_p \tau_{yyi,j}^0
\end{aligned} \tag{3.50}$$

Source term of τ_{xy} equations:

$$\begin{aligned}
b\tau_{xy}|_{i,j} &= \frac{\partial v}{\partial x} \left(We \tau_{xx}^0 + w_r \right) \Big|_{i,j} \Delta x_i \Delta y_j + \frac{\partial u}{\partial y} \left(We \tau_{yy}^0 + w_r \right) \Big|_{i,j} \Delta x_i \Delta y_j \\
&+ (1 - \alpha_\tau) A_p \tau_{xyi,j}^0
\end{aligned} \tag{3.51}$$

where superscript 0 denotes the values obtained at previous iteration. Gradients of velocities are computed by central differences at interior domain, however near the boundary they are calculated by introducing a polynomial function such as:

$$\begin{aligned}
v &= ax^2 + bx + c & \frac{\partial v}{\partial x} &= 2ax + b \\
u &= ay^2 + by + c & \frac{\partial u}{\partial y} &= 2ay + b
\end{aligned} \tag{3.52}$$

3.3. SOLUTION ALGORITHM

To date various algorithms have been developed to calculate pressure field. Semi-Implicit Method for the Pressure-Linked Equation (SIMPLE) was the first proposed by Patankar and Spalding [59] and widely used in the literature. After that several modifications have been made to enhance its efficiency, such as SIMPLE revised (SIMPLER) [38], SIMPLE consistent (SIMPLEC) [60] and pressure-implicit with splitting of operators (PISO) [61]. In this study, the SIMPLE and SIMPLEC are employed to solve the coupled system of the continuity,

momentum and constitutive equations. Source terms of the momentum equations contain extra stresses which are nonlinearly coupled with the stress equations. Here, the decoupling technique is adopted in such a way that source term of the momentum equations is treated as pseudo-body forces that are already determined in the previous iteration [23]. The set of linearized algebraic equations are solved using the Line-by-Line technique based on the TDMA (Thomas algorithm or the tridiagonal matrix algorithm) and the alternative direction implicit (ADI) scheme. For pressure correction equation, four ADI sweeps are made [29] before correcting pressure and velocities. To stabilize the calculations, global under-relaxation factors are used depending on values of the Reynolds and Weissenberg Numbers. The solution process is reiterated until the maximum relative change of flow variables ($u, v, p, \tau_{xx}, \tau_{yy}, \tau_{xy}$) are less than a prescribed tolerance or residual as:

$$\text{res} = \text{MAX} \left\{ \frac{|\phi^{n+1} - \phi^n|}{|\phi^{n+1}|} \right\} \leq 1 \times 10^{-5} \quad (3.53)$$

where $\phi = (u, v, p, \tau_{xx}, \tau_{yy}, \tau_{xy})^T$.

3.4. MOMENTUM INTERPOLATION METHOD (MIM)

The final form of the discretized governing x-momentum equation with the under-relaxation factor over the control volume can be expressed symbolically as follows:

$$\frac{A_p}{\alpha_u} u_p = \sum_i A_i u_i - \Delta y (p_e - p_w) + \frac{(1 - \alpha_u) A_p}{\alpha_u} u_p^0 \quad (3.54)$$

Equation (3.54) can be written for u velocity at nodes P and E (see Figure 3.3) as follows:

$$u_p = \frac{\alpha_u \left(\sum_i A_i u_i + (1 - \alpha_u) A_p u_p^0 \right)}{A_p|_p} - \frac{\alpha_u \Delta y}{A_p|_p} (p_e - p_w) \quad (3.55)$$

$$u_E = \frac{\alpha_u \left(\sum_i A_i u_i + (1 - \alpha_u) A_p u_E^0 \right)}{A_p|_E} - \frac{\alpha_u \Delta y}{A_p|_E} (p_{ee} - p_e) \quad (3.56)$$

Face velocity u_e can be formulated by equations (3.55) and (3.56)

$$u_e = \frac{\alpha_u \left(\sum_i A_i u_i + (1 - \alpha_u) A_p u_e^0 \right)}{A_p|_e} - \frac{\alpha_u \Delta y}{A_p|_e} (p_E - p_P) \quad (3.57)$$

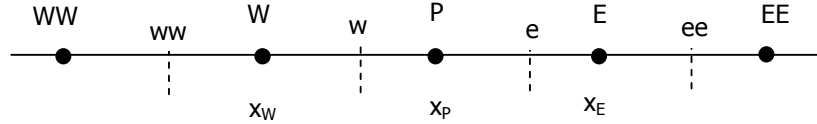


Figure 3.3. Grid points in the x direction

First term of the right hand side of equation (3.57) can be obtained using equations (3.55) and (3.56) by linear interpolation.

$$\frac{\alpha \left(\sum_i A_i u_i + (1 - \alpha_u) A_p u_e^0 \right)}{A_p|_e} = A \left[\frac{\alpha \left(\sum_i A_i u_i + (1 - \alpha_u) A_p u_E^0 \right)}{A_p|_E} \right] + (1 - A) \left[\frac{\alpha \left(\sum_i A_i u_i + (1 - \alpha_u) A_p u_P^0 \right)}{A_p|_P} \right] \quad (3.58)$$

where A is the linear interpolation factor and defined as

$$A = \frac{x_e - x_P}{x_E - x_P} \quad (3.59)$$

From equation (3.55)

$$\left[\frac{\alpha_u \left(\sum_i A_i u_i + (1 - \alpha_u) A_p u_p^0 \right)}{A_p|_p} \right] = u_p + \frac{\alpha_u \Delta y}{A_p|_p} (p_e - p_w) \quad (3.60)$$

From equation (3.56)

$$\left[\frac{\alpha_u \left(\sum_i A_i u_i + (1 - \alpha_u) A_p u_E^0 \right)}{A_p|_E} \right] = u_E + \frac{\alpha_u \Delta y}{A_p|_E} (p_{ee} - p_e) \quad (3.61)$$

Substitution of equations (3.60) and (3.61) into the equation (3.58), yields

$$\begin{aligned} \frac{\alpha \left(\sum_i A_i u_i + (1 - \alpha_u) A_p u_e^0 \right)}{A_p|_e} &= A \left[u_E + \frac{\alpha_u \Delta y}{A_p|_E} (p_{ee} - p_e) \right] \\ &+ (1 - A) \left[u_p + \frac{\alpha_u \Delta y}{A_p|_p} (p_e - p_w) \right] \end{aligned} \quad (3.62)$$

and finally by inserting equation (3.62) into the equation (3.57)

$$\begin{aligned} u_e &= A \left[u_E + \frac{\alpha_u \Delta y}{A_p|_E} (p_{ee} - p_e) \right] + (1 - A) \left[u_p + \frac{\alpha_u \Delta y}{A_p|_p} (p_e - p_w) \right] \\ &- \frac{\alpha_u \Delta y}{A_p|_e} (p_E - p_P) \end{aligned} \quad (3.63)$$

We rearrange equation (3.63) to the form

$$\begin{aligned} u_e &= A u_E + (1 - A) u_p + \left[A \frac{\alpha_u \Delta y}{A_p|_E} (p_{ee} - p_e) + (1 - A) \frac{\alpha_u \Delta y}{A_p|_p} (p_e - p_w) \right] \\ &- \frac{\alpha_u \Delta y}{A_p|_e} (p_E - p_P) \end{aligned} \quad (3.64)$$

Last term of the equation (3.64) contains coefficient $\left(\frac{1}{A_p|_e} \right)$. This term is also obtained

linearly from P and E nodes.

$$\frac{1}{A_p|_e} = A \frac{1}{A_p|_E} + (1-A) \frac{1}{A_p|_P} \quad (3.65)$$

Equation (3.64) first introduced by Rhie and Chow's [31] and is called Momentum Interpolation Method (MIM) after reformulated by Majumdar [32] to avoid dependency on the under-relaxation parameter.

$$u_e = Au_E + (1-A)u_P + \left[A \frac{\alpha_u \Delta y}{A_p|_E} (p_{ee} - p_e) + (1-A) \frac{\alpha_u \Delta y}{A_p|_P} (p_e - p_w) \right] - \frac{\alpha_u \Delta y}{A_p|_e} (p_E - p_P) + (1-\alpha_u) \{u_e^0 - Au_E^0 - (1-A)u_P^0\} \quad (3.66)$$

At this point all formulations which are derived above to find face velocities like staggered arrangement. Now we can derive SIMPLE [60] and SIMPLE-C [61] algorithm by using these face velocities.

3.5. SIMPLE ALGORITHM FOR COLLOCATED GRID

SIMPLE was the first proposed by Patankar and Spalding [59] for staggered grids and has been widely used in both Newtonian and non-Newtonian simulation to predict pressure field.

The final form of the discretized governing x-momentum equation with the under-relaxation factor at the face of the control volume can be expressed symbolically as follows:

$$\frac{A_e}{\alpha_u} u_e = \sum_i A_i u_i + \Delta y (p_P - p_E) + b_e + \left[\frac{(1-\alpha_u)}{\alpha_u} A_e \right] u_e^0 \quad (3.67)$$

Equation (3.67) can be written for initial guess values of pressure p^*

$$\frac{A_e}{\alpha_u} u_e^* = \sum_i A_i u_i^* + \Delta y (p_P^* - p_E^*) + b_e + \left[\frac{(1-\alpha_u)}{\alpha_u} A_e \right] u_e^0 \quad (3.68)$$

u_e^* in equation (3.68) can be calculated from equation (3.66).

We want to improve guess or previous iterate pressure field (p^*) by introducing correction,

$$p = p^* + p' \quad (3.69)$$

$$u = u^* + u' \quad (3.70)$$

If we subtract equation (3.68) from equation (3.67) we obtain

$$\frac{A_e}{\alpha_u} u'_e = \sum_i A_i u'_i + \Delta y (p'_P - p'_E) \quad (3.71)$$

In SIMPLE algorithm main approximation is to cancel out the term $\sum_i A_i u'_i$ such that [57].

$$\frac{A_e}{\alpha_u} u'_e \approx \Delta y (p'_P - p'_E) \Rightarrow u'_e \approx \frac{\alpha_u}{A_e} \Delta y (p'_P - p'_E) \Rightarrow u'_e \approx du (p'_P - p'_E) \quad (3.72)$$

$$du|_e = \frac{\alpha_u}{A_e} \Delta y \Rightarrow du|_e = A \frac{\alpha_u}{A_E} \Delta y + (1-A) \frac{\alpha_u}{A_P} \Delta y \quad (3.73)$$

where A is the interpolation factor defined by equation (3.59).

If we insert u'_e (3.72) in to the equation (3.70),

$$u_e = u_e^* + du|_e (p'_P - p'_E) \quad (3.74)$$

After applying the same procedures for y-momentum we obtain

$$v_n = v_n^* + dv|_n (p'_P - p'_N) \quad (3.75)$$

$$dv|_n = \frac{\alpha_v}{A_n} \Delta x \Rightarrow dv|_n = B \frac{\alpha_v}{A_N} \Delta x + (1-B) \frac{\alpha_v}{A_P} \Delta x \quad (3.76)$$

where B is the interpolation factor for y direction and defined as:

$$B = \frac{y_n - y_P}{y_N - y_P} \quad (3.77)$$

Using the continuity and equations (3.74) and (3.75) we can derive pressure correction equation as

$$\frac{\partial u}{\partial x} + \frac{\partial v}{\partial y} = 0 \quad (3.78)$$

Integrating equation (3.77) over the control volume shown in Figure 3.1, the following discretized form can be obtained

$$(u_e - u_w)\Delta y + (v_n - v_s)\Delta x = 0 \quad (3.79)$$

Equations (3.74) and (3.75) are substituted in to the equation (3.79)

$$\begin{aligned} & [u_e^* + du|_e(p_P' - p_E') - u_w^* - du|_w(p_W' - p_P')] \Delta y \\ & + [v_n^* + dv|_n(p_P' - p_N') - v_s^* - dv|_s(p_S' - p_P')] \Delta x = 0 \end{aligned} \quad (3.80)$$

We rearrange equation (3.80) to the form

$$\begin{aligned} p_P' [(du|_e + du|_w)\Delta y + (dv|_n + dv|_s)\Delta x] = & \\ & + p_E' [du|_e \Delta y] + p_W' [du|_w \Delta y] \\ & + p_N' [dv|_n \Delta x] + p_S' [dv|_s \Delta x] \\ & + [(u_w^* - u_e^*)\Delta y + (v_s^* - v_n^*)\Delta x] \end{aligned} \quad (3.81)$$

Discretized form of the pressure correction, p' equation is considered as

$$A_P p'_{i,j} = A_E p'_{i+1,j} + A_W p'_{i-1,j} + A_N p'_{i,j+1} + A_S p'_{i,j-1} + b p'_{i,j} \quad (3.82)$$

where the coefficients are given by

$$A_E = du|_e \Delta y \quad A_W = du|_w \Delta y \quad (3.83)$$

$$A_N = dv|_n \Delta x \quad A_S = dv|_s \Delta x \quad (3.84)$$

$$A_P = A_E + A_W + A_N + A_S \quad b p'_{i,j} = (u_w^* - u_e^*)\Delta y + (v_s^* - v_n^*)\Delta x \quad (3.85)$$

Velocities in source term are calculated MIM method derived as equation (3.66).

Followings are the summary of the modification of SIMPLE algorithm for collocated grids.

1. Solve equation (3.95) and (3.96) to obtain velocity field at the center point of the control volume (u_p^* and u_E^*).
2. Evaluate face velocities, u_e^* , by solving equation (3.66).
3. Solve equations (3.73) and (3.76) to obtain face correction values $du|_e$ and $dv|_n$
4. Solve pressure correction equation (3.82) by using equations (3.66), (3.73) and (3.76) to obtain pressure correction values at the center of the control volume.
5. Correct pressure by using $p = p^* + p'$
6. Find pressure and pressure correction face values by using linear interpolation.

$$p_e = Ap_E + (1-A)p_p \qquad p'_e = Ap'_E + (1-A)p'_p$$
7. Correct velocities at the center of the control volume by using following equation

$$u_p = u_p^* + du|_p (p'_w - p'_e)$$
8. Calculate face velocities by using equation (3.66) and use these face velocities for calculation convective fluxes (F_e, F_w, F_n, F_s) in momentum and stresses equations.
9. Calculate source term of the momentum equations by solving stresses equations.
10. Check the convergence, if it does not converge, return to step (1).

3.6. SIMPLE-C ALGORITHM FOR COLLOCATED GRID

The main difference between SIMPLE and SIMPLE-C algorithm is the calculation of the correction values. In SIMPLE algorithm correction value is obtained by using equations (3.73) and (3.75). While in SIMPLE-C algorithm correction value is calculated by the following equations.

$$du|_P = \frac{\alpha_u \Delta y}{[A_P - (A_E + A_W + A_N + A_S)]} \Big|_P \tag{3.86}$$

$$du|_E = \frac{\alpha_u \Delta y}{[A_P - (A_E + A_W + A_N + A_S)]} \Big|_E$$

and at the face

$$du|_e = Adu|_E + (1-A)du|_P \quad (3.87)$$

where A is the interpolation factor defined by equation (3.59).

In SIMPLE algorithm, we have used only one correction values only for both evaluation of face velocities (equation 3.65) and calculation pressure correction coefficients (equation 3.79). But in the SIMPLE-C algorithm we define two different correction values:

- a) For calculation of face velocities (equation 3.66) we used the same correction values (3.73) in the SIMPLE.
- b) However for the correction coefficients in pressure calculation we employed equation (3.86)

CHAPTER 4

SIMULATION OF STEADY LID-DRIVEN CAVITY FLOW AT HIGH REYNOLDS NUMBERS BY FINITE VOLUME APPROACH USING COLLOCATED GRIDS

In this chapter, simulations of steady incompressible square lid-driven cavity flow at high Reynolds numbers up to 40000 are presented. Navier-Stokes equations are solved using finite volume approach with central differences scheme. A non-uniform collocated grid arrangement of 257x257 is used. Coupled mass and momentum conservation equations are solved through iterative SIMPLE (Semi-Implicit Method for Pressure-Linked Equation) algorithm. Momentum interpolation method (MIM) is used to evaluate face velocities as well as the evaluation of coefficient of the discretization equation. Effect of the solution procedure of pressure correction equation, which is called inner loop, on the solution is discussed in detail. Results are compared with those in literature.

4.1 INTRODUCTION

Lid-driven cavity flow of a Newtonian fluid is one of the most well-known problems in Computational Fluid Dynamics (CFD) literature [62-70] due to simple geometry, easy boundary condition implementation and available benchmark results. Despite its simple geometry depicted in Figure 4.1, lid driven cavity flow offers many challenges that are encountered in the form of singularity points [67]. Therefore numerical technique that can be handle lid cavity flow is well poised to be used for the simulation of other challenging flows.

Sahin and Owens [65] have introduced a novel implicit cell vertex finite volume method for the solution of the lid-driven cavity flow at high Reynolds numbers. They presented steady and unsteady cavity solution using strongly graded mesh of 257x257 and Reynolds numbers up to 10000. Lid-driven cavity studies in numerical field are discussed and reviewed in detail by Erturk [64]. Recently, Erturk et al. [62] have used stream function-vorticity formulation

for the solution of 2-D steady incompressible flow in a lid-driven cavity. With a uniform grid size 601×601 they have obtained second-order accurate steady solution up to Reynolds number of 21000. This is the largest Reynolds number reported so far in literature. In another report Erturk and Gokcel [63] investigated the same problem with using fourth-order compact formulation. They have obtained accurate solution up to Reynolds numbers of 20000 with uniform grid of 601×601 . Recent studies on the lid-driven cavity flow problem were reviewed by Erturk et al. [62] in terms of used numerical methods and their spatial order of accuracy and highest attainable Reynolds number.

Reports on finite volume solution of high Reynolds number steady lid-driven cavity flow field through collocated grid structure are not in the literature to the best knowledge of the author. Therefore, objective of this chapter has two-folds: One is to demonstrate steady high Reynolds numbers lid-driven cavity solutions available by using collocated structure of even modest 257×257 grids. The other one is to investigate effect of the pressure correction inner iteration loop on numerical solutions.

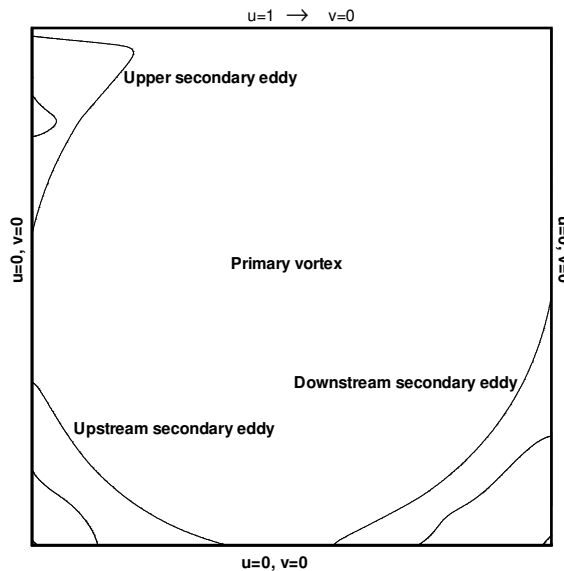


Figure 4.1. Square lid-driven cavity geometry with boundary conditions.

4.2. GOVERNING EQUATIONS AND NUMERICAL METHODOLOGY

For a two dimensional system of rectangular coordinates (x, y) , the dimensionless steady-state, incompressible the governing equations are

Continuity:

$$\frac{\partial u}{\partial x} + \frac{\partial v}{\partial y} = 0 \quad (4.1)$$

x-momentum

$$\frac{\partial uu}{\partial x} + \frac{\partial vu}{\partial y} = -\frac{\partial p}{\partial x} + \frac{1}{\text{Re}} \left(\frac{\partial^2 u}{\partial x^2} + \frac{\partial^2 u}{\partial y^2} \right) \quad (4.2)$$

y-momentum

$$\frac{\partial uv}{\partial x} + \frac{\partial vv}{\partial y} = -\frac{\partial p}{\partial y} + \frac{1}{\text{Re}} \left(\frac{\partial^2 v}{\partial x^2} + \frac{\partial^2 v}{\partial y^2} \right) \quad (4.3)$$

These PDEs are discretized using finite volume method and non-uniform collocated grid arrangement. A second-order central difference scheme is employed to approximate both convective and diffusion terms. Pressure field is obtained by solving pressure-correction procedure of SIMPLE algorithm for collocated grids as outlined in Chapter 3.

Solution procedure of pressure-correction equation and its effect on the performance of the SIMPLE algorithm with staggered grid system was reported by Deng and Tang [71]. Before correcting pressure and velocities, pressure correction equation is iterated to satisfy continuity which is called inner loop. They investigated the role of solving pressure-correction equation by performing three test cases; lid driven cavity, rectangular tank flow and backward facing step on Newtonian fluids. They concluded that generally to increasing number of the inner iterations reduces the required number of iterations for overall convergence hence effectively improves performance of the SIMPLE algorithm. However, it is very difficult to determine optimum cycle number for inner loop. Deng and Tang [71] found that setting number of inner cycle as four is sufficient for all three test cases. Based on their analysis we can define optimum number of inner cycle for any fluid flow problem. When the residual ratio between pressure correction equation and momentum equation is nearly one, the number of cycle number of inner loop can be then considered as optimum. Deng and Tang [71] did not investigate whether the pressure correction inner loop has any effect on attainable maximum Reynolds number. Hence, here, the effect of the pressure correction inner loop on achievable maximum Reynolds number is investigated by considering lid-driven cavity flow.

4.3. NUMERICAL RESULTS AND DISCUSSION

In the present study a non-uniform collocated grid arrangement having 257x257 grid points is employed as shown in Figure 4.2. The smallest cell area of this mesh near the lid is 1.3×10^{-6} . Erturk et al. [62] have presented steady solution up to Reynolds number of 21000. They could not get steady solutions beyond this Reynolds number even they used finer meshes of 601x601 and 1025x1025 [64]. Barragy and Carey [69] have also presented by using p-type finite element method to simulate steady flows with non-uniform element meshes of 257x257 up to Reynolds number of 16000. However, at this Reynolds number their vorticity solutions showed oscillatory behavior due to coarse mesh. These two reported studies show that very fine mesh must be used to obtain converged steady solution at high Reynolds numbers. This study, on the other hand demonstrates that in addition to fine mesh, numerical method and grid type are important to get high Reynolds number solutions. Numerical results at Reynolds numbers ranging from 100 to 40000 are presented.

Figure 4.3 and Figure 4.4 depict the stream function and vorticity at different Reynolds numbers. Stream function, ψ , and vorticity, ω , are obtained through the solution of the following equations.

$$\nabla^2 \psi = -\omega \quad (4.4)$$

$$\omega = -\frac{\partial u}{\partial y} + \frac{\partial v}{\partial x} \quad (4.5)$$

These figures indicate that the numerical implementation employed captures the steady solutions of cavity flow even at 257x257 grids without any oscillation. In the previous section the importance of pressure correction inner loop cycle on numerical iteration was discussed. Then computations were carried out first by four inner cycle iterations. With this number, steady solutions could not be obtained at Reynolds numbers greater than 15000. Increasing the inner cycle iteration from four to six improved the maximum attainable Reynolds number to 25000. This effect of inner cycle iteration number can be expected. As Reynolds number increases, convective terms become dominant in the momentum equations; hence additional pressure correction inner loop cycle is required to satisfy the continuity equation. It was then decided to increase inner loop cycle to twelve for Reynolds number greater than 25000 so that steady solutions up to Reynolds number of 40000 can be obtained.

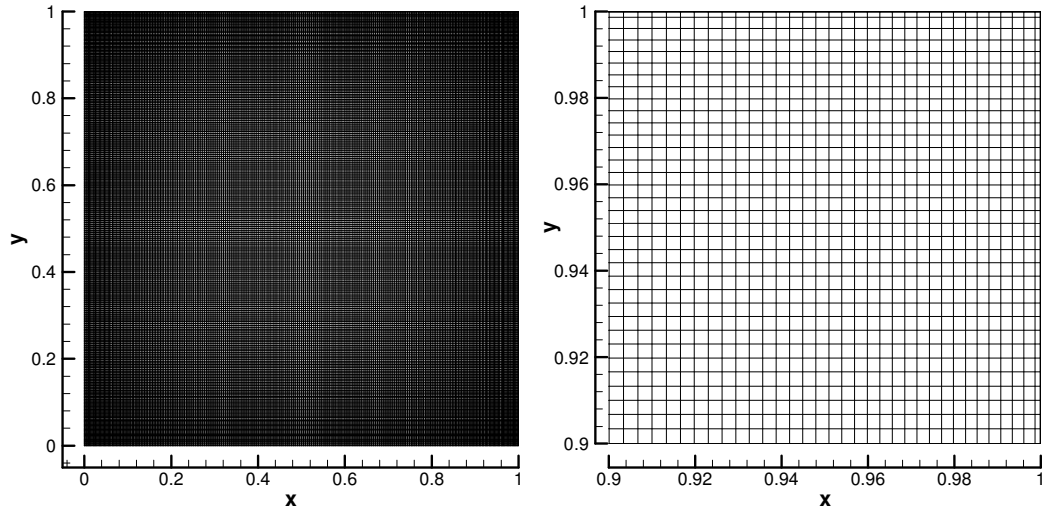
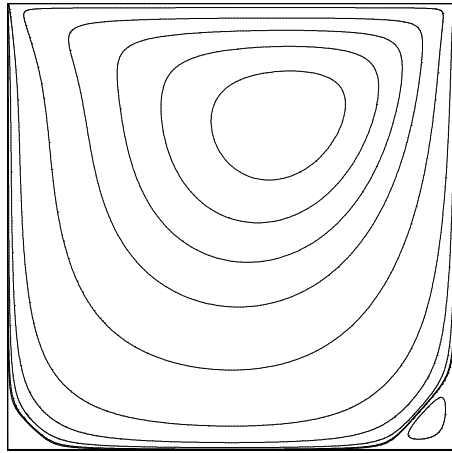


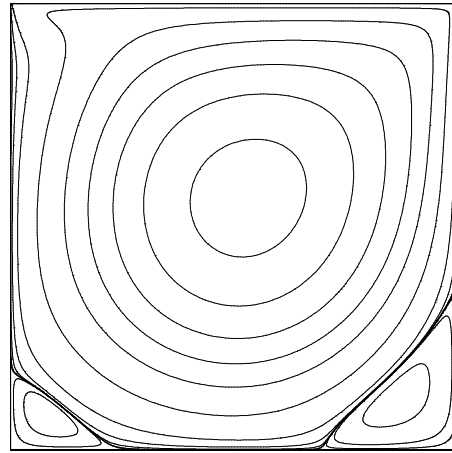
Figure 4.2. Non-uniform graded meshes of 257x257 grid points with enlargement view of right top corner.

In Figure 4.3, as the Reynolds numbers increases primary vortex center moves to the center. After Reynolds numbers of 10000 tertiary vortex [62] starts to appear at the top left corner and it grows with increasing Reynolds numbers. Another feature of these streamline plots is quaternary eddy at Reynolds number of 10000 is visible. However, this eddy was not observed by Erturk et al. [62] with grid size less than 513x513 at Reynolds number of 10000.

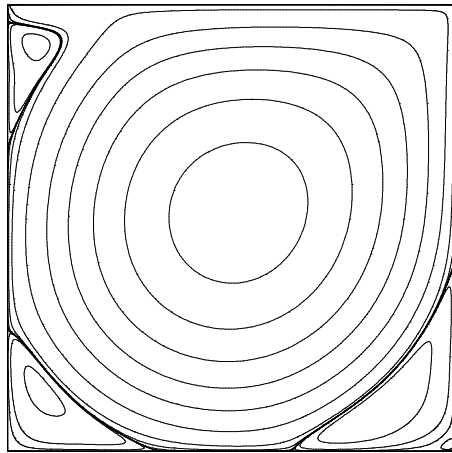
In Figure 4.4, vorticity contour moves towards the wall with increasing Reynolds numbers. For $Re \geq 5000$ very strong vorticity gradients develops on the lid and walls [65]. Values of the stream function and vorticity and their primary locations are tabulated in Table 4.1. It can be seen that beyond Reynolds number 20000 locations of the primary vortex does not change, as would expected. This behavior was also observed by Erturk et al. [62] for $Re \geq 17500$. Figure 4.5 depicts contours of pressure fields. Pressure contours move to the center with increasing Reynolds numbers.



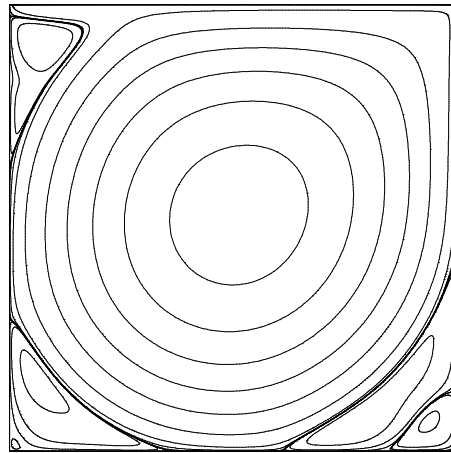
a) $Re = 100$



b) $Re = 1000$

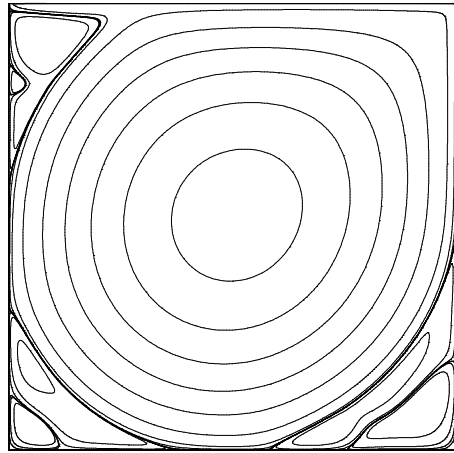


c) $Re = 5000$

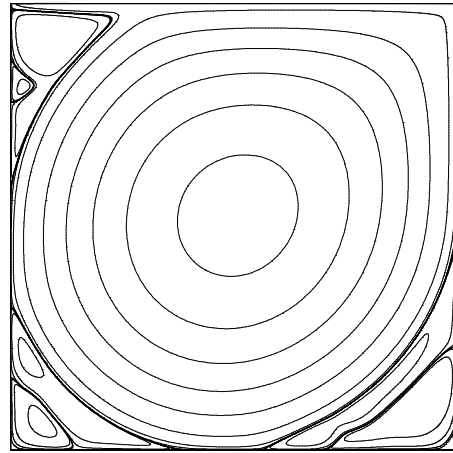


d) $Re = 10000$

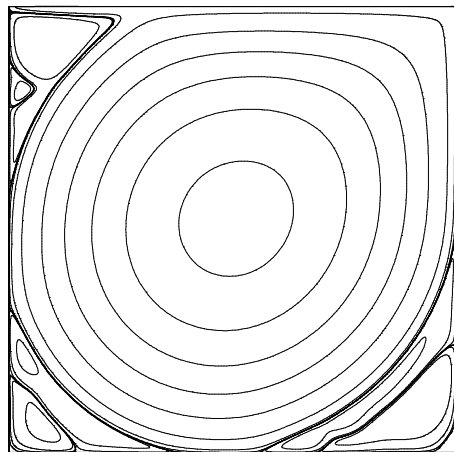
Figure 4.3. Stream functions at various Reynolds numbers.



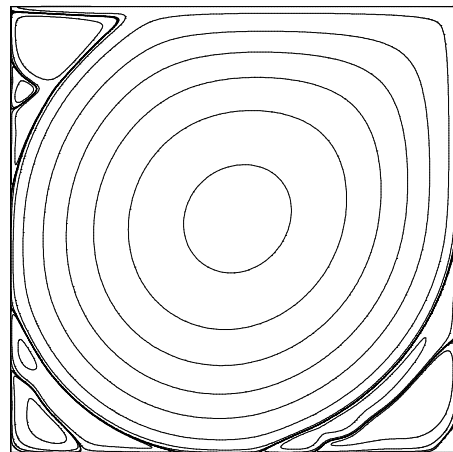
e) $Re = 20000$



f) $Re = 30000$

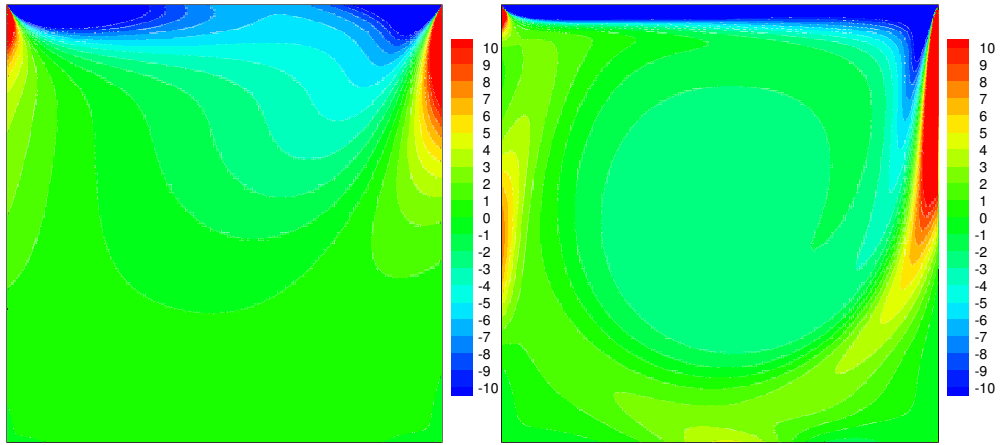


g) $Re = 35000$



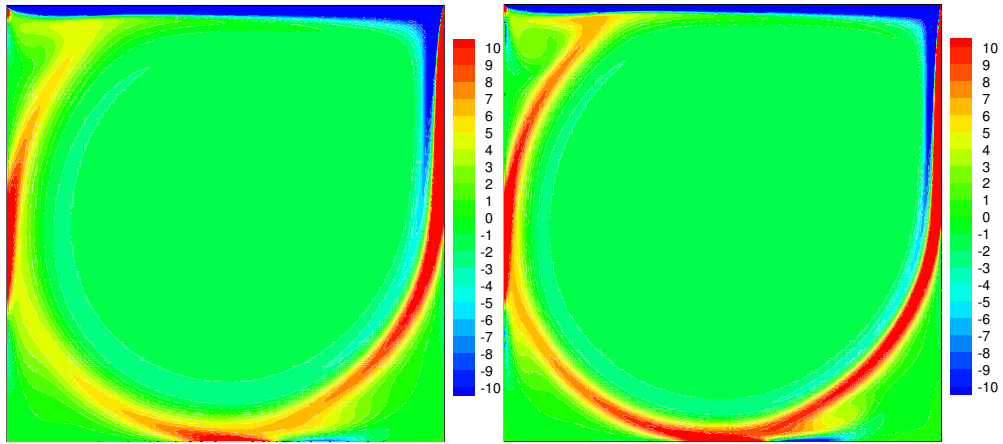
h) $Re = 40000$

Figure 4.3. Stream functions at various Reynolds numbers. (continued).



a) $Re = 100$

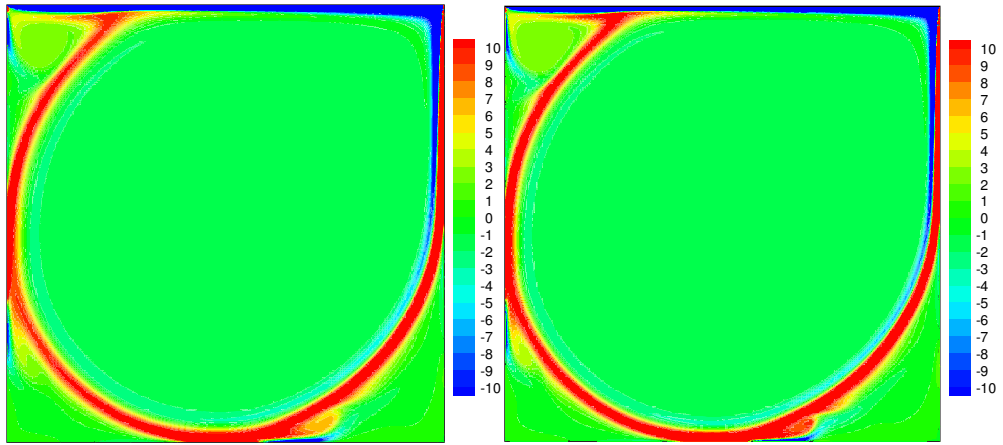
b) $Re = 1000$



c) $Re = 5000$

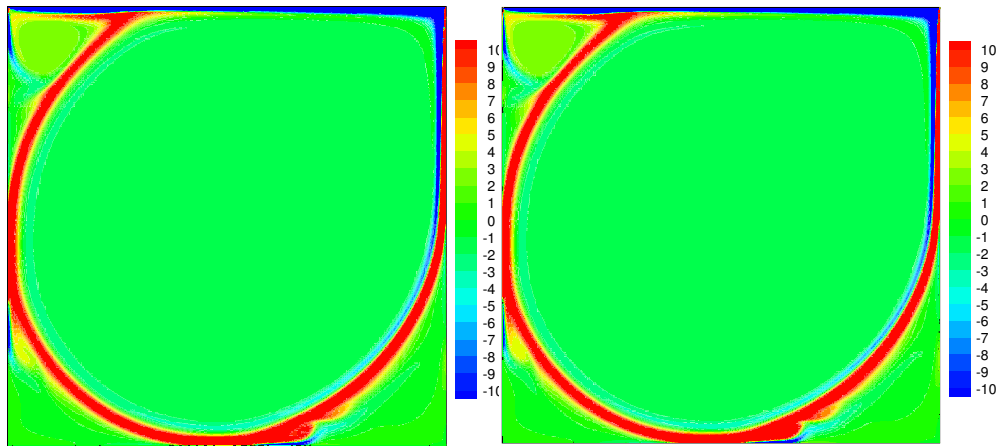
d) $Re = 10000$

Figure 4.4. Vorticity contours at various Reynolds numbers. Contour levels are shown from -10 to 10 with increment of 1.



e) Re = 20000

f) Re = 30000



g) Re = 35000

h) Re = 40000

Figure 4.4. Vorticity contours at various Reynolds numbers. Contour levels are shown from -10 to 10 with increment of 1 (continued).

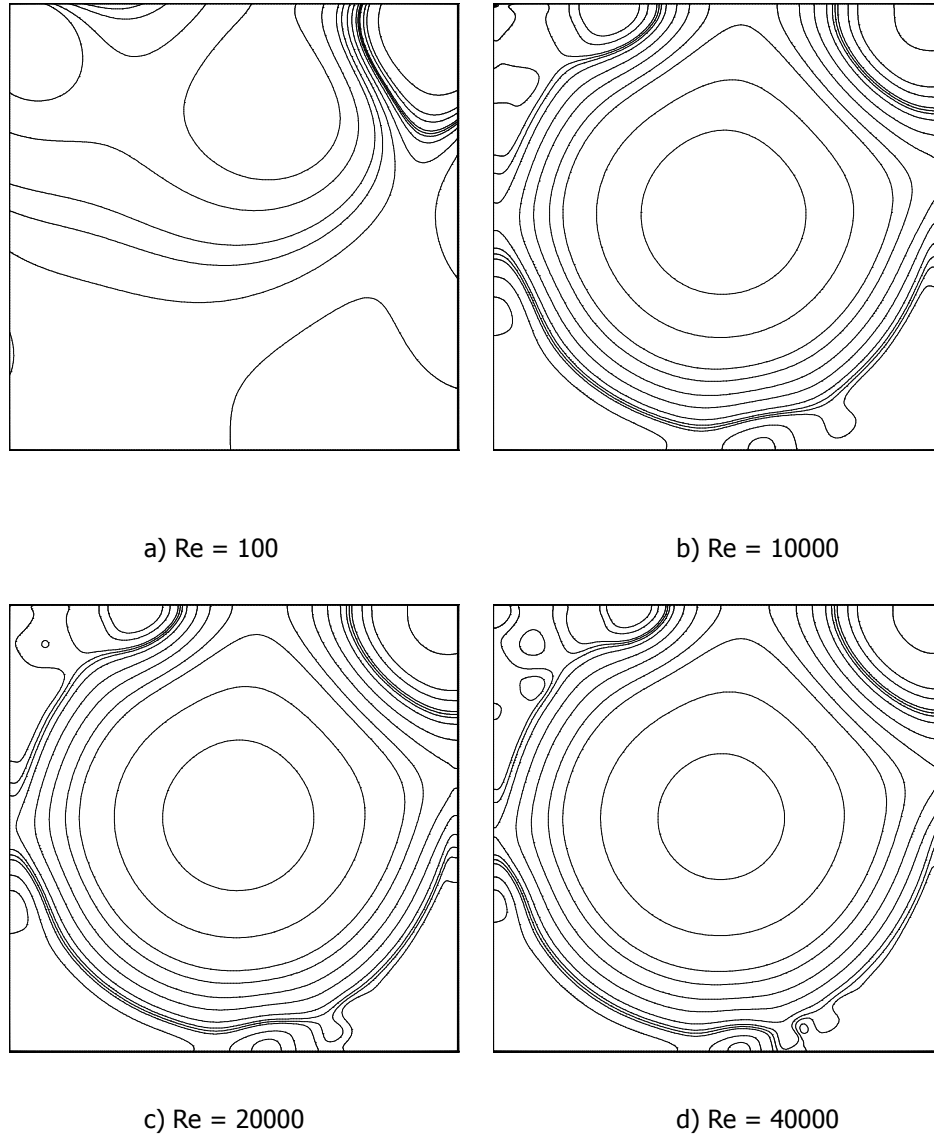


Figure 4.5. The pressure contour for various Reynolds numbers

Figure 4.6 and 4.7 show the effect of Reynolds number on the horizontal (u) and vertical (v) velocity distribution at $x=0.5$ and $y=0.5$, respectively. The maximum and minimum values of the velocity components at the corresponding centerlines are also given in Table 4.2 along with their locations. Here subscripts denote values pertaining to the minimum and maximum velocities. Table 4.3 shows comparison of the intensities of the primary eddy and vorticity results found in the literature. Presented results are in good agreement with second order accuracy results of Erturk et al. [62]. Higher velocities near the top surface or lid than those near the bottom naturally result in smaller flow area for the flow in the lid movement

direction than the flow in the opposite direction. This continuity effect depicts itself in the form of off-centered stream function, vorticity and pressure contour plots especially at low Reynolds number. On the other hand, as inertial terms gain strength, top to bottom distributions of the quantities become more symmetric while gradients in the x or lid movement direction get stronger.

These results demonstrate that steady high Reynolds number flows can be simulated using even coarse grids.

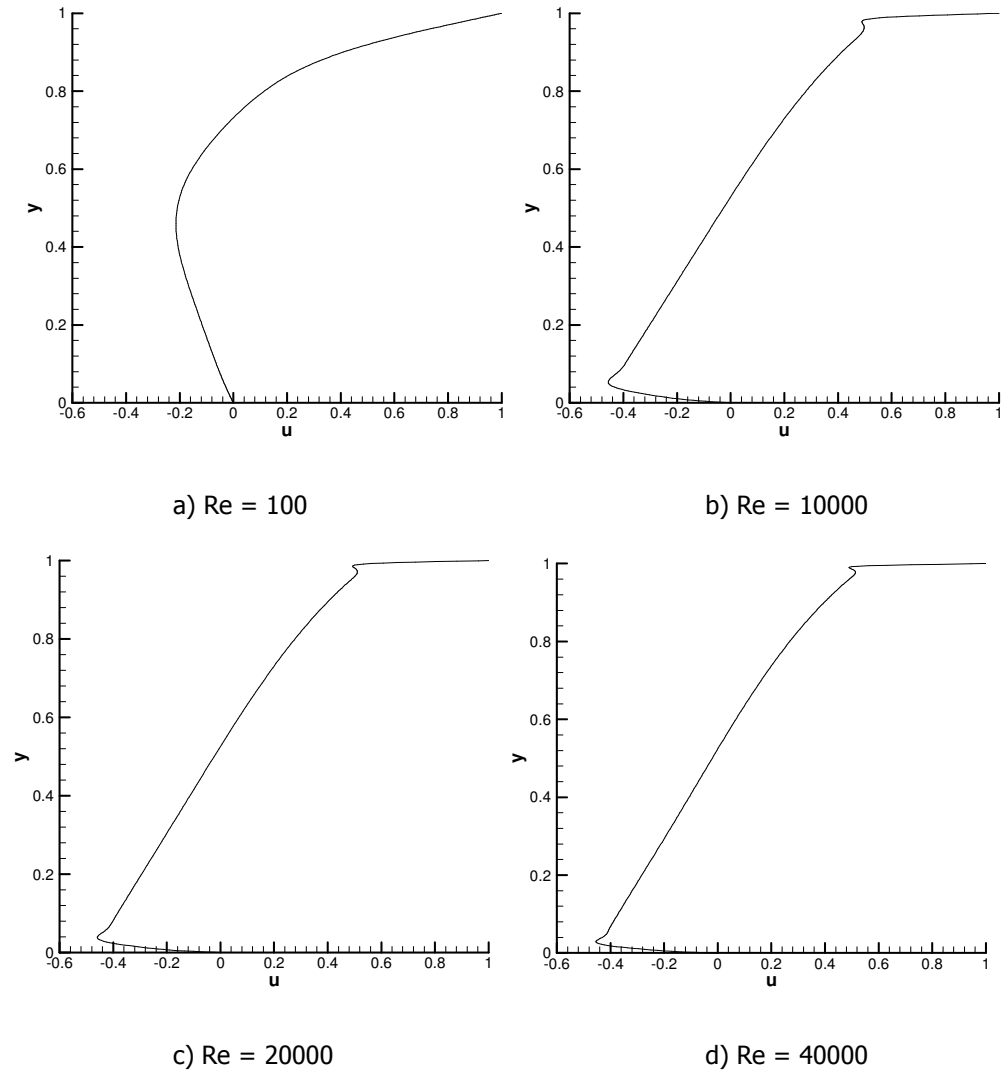
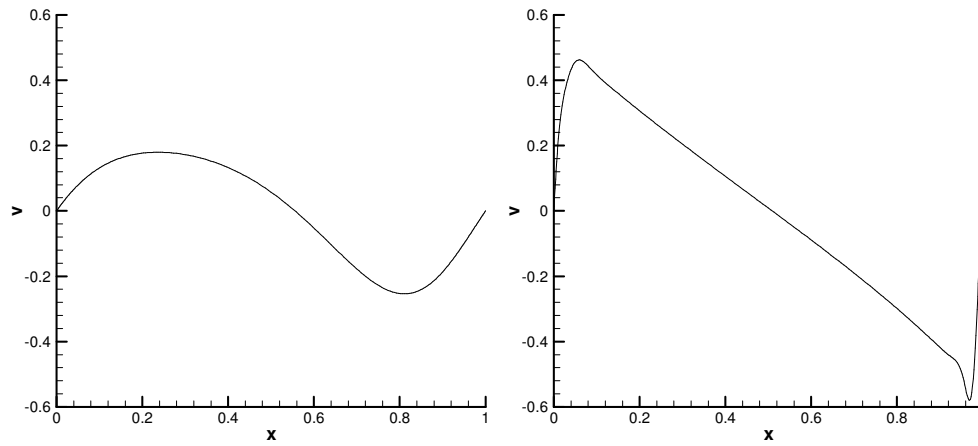
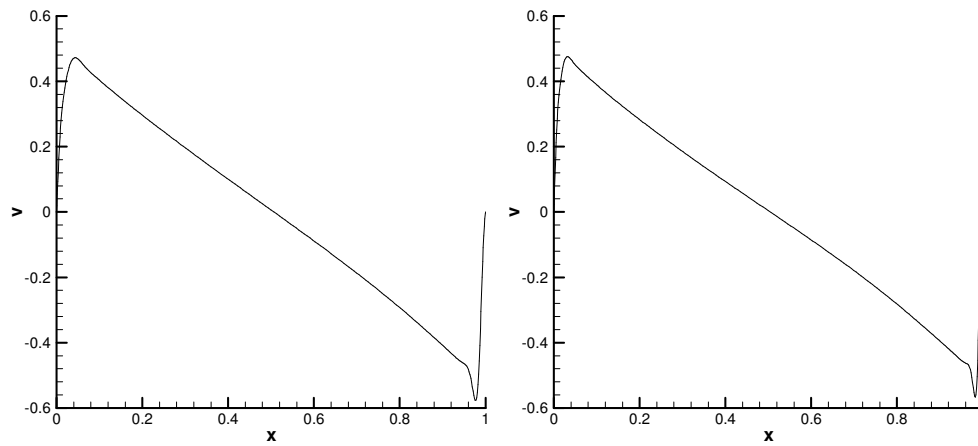


Figure 4.6. Profiles of horizontal velocity (u) at vertical centerline ($x=0.5$).



a) $Re = 100$

b) $Re = 10000$



c) $Re = 20000$

d) $Re = 40000$

Figure 4.7. Profiles of vertical velocity (v) at horizontal centerline ($y=0.5$).

Table 4.1. Intensities of the primary eddies and vorticity and their locations.

| Re | ψ_{\min} | ω | x_{\min} | y_{\min} |
|-------|---------------|------------|------------|------------|
| 100 | -0.10341067 | -3.1647956 | 0.61553348 | 0.73744621 |
| 400 | -0.11382828 | -2.2972451 | 0.55196863 | 0.60301751 |
| 1000 | -0.11873676 | -2.0661868 | 0.53253953 | 0.56485206 |
| 5000 | -0.12169451 | -1.9316066 | 0.51302859 | 0.53253953 |
| 7500 | -0.12161812 | -1.9120721 | 0.51302859 | 0.53253953 |
| 10000 | -0.12136419 | -1.8977556 | 0.51302859 | 0.53253953 |
| 15000 | -0.12068707 | -1.8735867 | 0.51302859 | 0.52604257 |
| 20000 | -0.11990739 | -1.8505587 | 0.50651521 | 0.52604257 |
| 25000 | -0.11906834 | -1.8272159 | 0.50651521 | 0.52604257 |
| 30000 | -0.11818048 | -1.8031062 | 0.50651521 | 0.52604257 |
| 35000 | -0.11725889 | -1.7784594 | 0.50651521 | 0.52604257 |
| 40000 | -0.11630788 | -1.7532791 | 0.50651521 | 0.52604257 |

Table 4.2. Horizontal minimum velocity, vertical minimum and maximum velocity through the centerlines of the cavity.

| Re | u_{\min} | y_{\min} | v_{\max} | x_{\max} | v_{\min} | x_{\min} |
|-------|-------------|------------|------------|------------|-------------|------------|
| 100 | -0.21394837 | 0.46097261 | 0.17952899 | 0.23673843 | -0.25380129 | 0.81058430 |
| 400 | -0.32851626 | 0.27869811 | 0.30367493 | 0.22680746 | -0.45401060 | 0.86327752 |
| 1000 | -0.38822348 | 0.17213964 | 0.37658325 | 0.15980540 | -0.52687868 | 0.90924372 |
| 5000 | -0.44598582 | 0.07421019 | 0.44615107 | 0.07952789 | -0.57472951 | 0.95791870 |
| 7500 | -0.45309198 | 0.06174353 | 0.45634260 | 0.06659128 | -0.57796271 | 0.96374108 |
| 10000 | -0.45650067 | 0.05258204 | 0.46222745 | 0.05938732 | -0.57925323 | 0.96922480 |
| 15000 | -0.45914842 | 0.04410015 | 0.46872173 | 0.04825858 | -0.57841837 | 0.97438591 |
| 20000 | -0.45932000 | 0.03816129 | 0.47213103 | 0.04410015 | -0.57609662 | 0.97603732 |
| 25000 | -0.45847694 | 0.03439419 | 0.47397444 | 0.04010188 | -0.57416247 | 0.97924015 |
| 30000 | -0.45734649 | 0.03256648 | 0.47504879 | 0.03625892 | -0.57141317 | 0.98079270 |
| 35000 | -0.45579347 | 0.03077520 | 0.47540200 | 0.03439419 | -0.56905611 | 0.98079270 |
| 40000 | -0.45409547 | 0.02901977 | 0.47537552 | 0.03256648 | -0.56701321 | 0.98231343 |

Table 4.3. Comparison of the stream function and vorticity values.

| Re | References | ψ_{\min} | ω |
|-------|------------|---------------|-----------|
| 100 | Present | -0.103410 | -3.164795 |
| | [65] | -0.103471 | -3.1655 |
| 400 | Present | -0.113828 | -2.297241 |
| | [65] | -0.113897 | -2.2950 |
| 1000 | Present | -0.118736 | -2.066186 |
| | [65] | -0.118800 | -2.0664 |
| | [62] | -0.118781 | -2.065530 |
| | [63] | -0.118938 | -2.067760 |
| 5000 | Present | -0.121694 | -1.931606 |
| | [65] | -0.122050 | -1.9392 |
| | [62] | -0.121289 | -1.926601 |
| | [63] | -0.122216 | -1.940547 |
| 7500 | Present | -0.121618 | -1.912072 |
| | [65] | -0.122302 | -1.9275 |
| | [62] | -0.120924 | -1.904883 |
| | [63] | -0.122344 | -1.926478 |
| 10000 | Present | -0.121364 | -1.897755 |
| | [65] | -0.122248 | -1.9231 |
| | [62] | -0.120403 | -1.888987 |
| | [63] | -0.122306 | -1.918187 |
| 15000 | Present | -0.120687 | -1.873586 |
| | [62] | -0.119240 | -1.863618 |
| | [63] | -0.122060 | -1.907651 |
| 20000 | Present | -0.119907 | -1.850558 |
| | [62] | -0.118039 | -1.841814 |
| | [63] | -0.121694 | -1.900032 |

CHAPTER 5

RESULTS AND DISCUSSION

All the simulations presented were carried out on single computer platform, including an AMD Athlon 64 FX-57 processor and 1GB Ram. The computer code, which we name as NONSOL (NON-Newtonian flow SOLver), was written based on the aforementioned algorithms. The code is applied to three different test cases: a) laminar steady flow in entrance planar channel, b) laminar steady flow in stick-slip and c) laminar steady flow in lid-driven square cavity. Oldroyd-B, Phan-Thien Tanner (PTT) and White-Metzner models are the constitutive models considered. To approximate of the convection terms in the momentum equations first order upwind, power-law second order central difference schemes are adopted. Besides third order quadratic upstream interpolation is used for convective kinematics QUICK schemes.

In order to test the computational methodology followed in this study first a simple geometry, flow through a channel, is considered. Satisfactory agreement between the simulation and analytical results indicate that the computational methodology followed in this study captures the non-Newtonian laminar flows.

Following the channel flow geometry, steady slip-stick and steady lid-driven flow in a square cavity are investigated. Various constitutive models are compared together with the numerical schemes. Loss of convergence at some critical value of Weissenberg number is also discussed as outlined Chapter 1.

Details and results of these three different flow geometries are presented in the following sections.

5.1. FLOW IN ENTRANCE OF PLANNER CHANNEL

As shown in Figure 5.1, we first consider channel Poiseuille flow problem to investigate constitutive model effect on the numerical solutions. Steady incompressible constitutive models given in Chapter 2 are applied to a planar channel, which has a length of $8H$ and a

width of $2H$ ($H=1$). At the inlet, the flow is assumed to be plug flow except in the immediate vicinity of the wall is shown in Figure 5.2, as described first by Gaidos and Darby [20] and reformulated by Na and Yoo [51].

$$u(y) = \begin{cases} 1.0448 & \text{for } y \leq 0.8714 \\ (-46.92 + 110.09y - 63.17y^2) & \text{for } y > 0.8714 \end{cases} \quad (5.1)$$

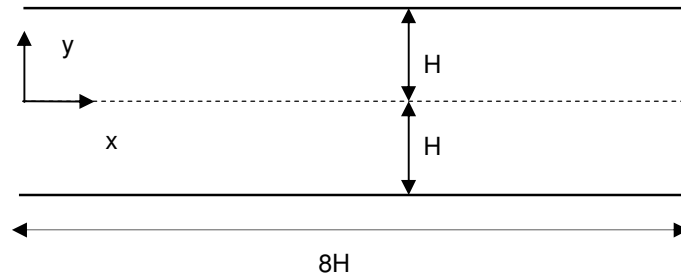


Figure 5.1. Planar channel flow geometry.

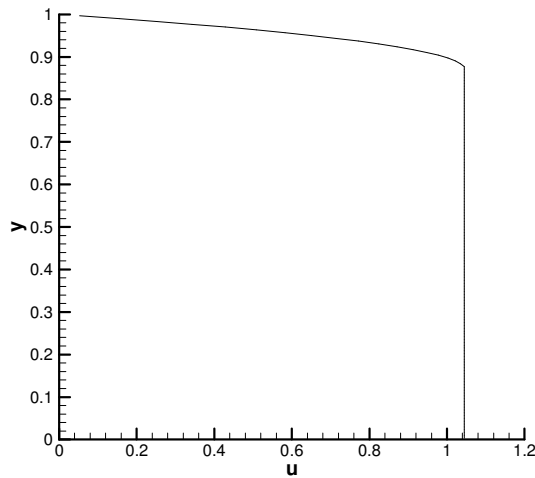


Figure 5.2. Inlet velocity profile.

Because of the hyperbolic structure of the constitutive equations, the stress components must be specified at the entrance. They are calculated by using the assumed entrance flow distribution and by the following relations:

$$\tau_{xx} = 2We(1-\beta)\left(\frac{\partial u}{\partial y}\right)^2 \quad (5.2)$$

$$\tau_{yy} = 0 \quad (5.3)$$

$$\tau_{xy} = (1-\beta)\frac{\partial u}{\partial y} \quad (5.4)$$

No slip boundary conditions are assumed at the solid wall for velocity,

$$u = 0, v = 0, \frac{\partial v}{\partial x} = 0, \frac{\partial v}{\partial y} = 0, \frac{\partial u}{\partial x} = 0 . \quad (5.5)$$

The stress components at the wall are obtained by solving constitutive equations and by applying known velocity boundary conditions in equation (5.5).

At the centerline

$$\frac{\partial u}{\partial y} = 0, v = 0, \frac{\partial v}{\partial x} = 0 \quad (5.6)$$

Similarly the stress components at the symmetry line are obtained by solving constitutive equations and by using equation (5.6)

At the exit the Neumann boundary conditions are imposed for the flow variables

$$\frac{\partial u}{\partial x} = 0, \frac{\partial v}{\partial x} = 0, \frac{\partial \tau_{xx}}{\partial x} = 0, \frac{\partial \tau_{yy}}{\partial x} = 0, \frac{\partial \tau_{xy}}{\partial x} = 0, \frac{\partial p}{\partial x} = 0 \quad (5.7)$$

Boundary values for pressure-correction equations are determined by considering velocity boundary conditions [71]. For instance, if the velocity boundary conditions are of Dirichlet type, Neumann type boundary conditions are applied to the pressure- correction equations. Conversely, if the velocity boundary conditions are of Neumann type, Dirichlet boundary conditions are used for pressure-correction equations.

The simple channel flow geometry was investigated previously by Gaidos and Darby [20] and Na and Yoo [51]. Na and Yoo [51] employed finite volume method with SIMPLER algorithm on a non-uniform staggered grid arrangement to simulate the flow of a Oldroyd-B fluid. They found that attainable maximum value of Weissenberg number increases with increasing Reynolds number. However, Gaidos and Darby [20] observed an opposite trend, as Reynolds number decreases, the maximum attainable Weissenberg number increases. This contradiction is discussed in this chapter for all constitutive equations.

To compare our results with Na and Yoo [51], we have chosen polymer viscosity, $w_r = (1 - \beta)$, as 0.8 in the Oldroyd-B model. Centerline velocity profiles are shown in Figures 5.3 at Re of 1×10^{-4} and $We = 1$. We used uniform collocated grids of 65 points in y -direction. Figure 5.3 illustrates that all schemes used for approximation of the convective terms in momentum equations produce close results with almost the same iteration number. However, QUICK scheme is the most expensive one in all schemes in terms of computing requirements. It almost needs 50% more computer time to achieve a prescribed tolerance than others. At this low Reynolds number, maximum attainable Weissenberg number for all schemes is obtained as 1. This critical value has not been exceeded by any of available schemes either. Na and Yoo [51] used the same constitutive model and polymer viscosity with non-uniform staggered mesh. They presented their results at different Reynolds numbers by using 20 graded grid points in y -direction. Their algorithm converged up to Weissenberg number of 0.4 which is considerably smaller than that of presented study for $Re \ll 1$. Figures 5.3 and Figure 5.4 show that velocity and stress first overshoot before to the fully developed flow values. At least channel length of $8H$ is needed for the relaxation of the stress. In other words, in order to obtain converged solution under described conditions, channel length should be set larger than $6H$.

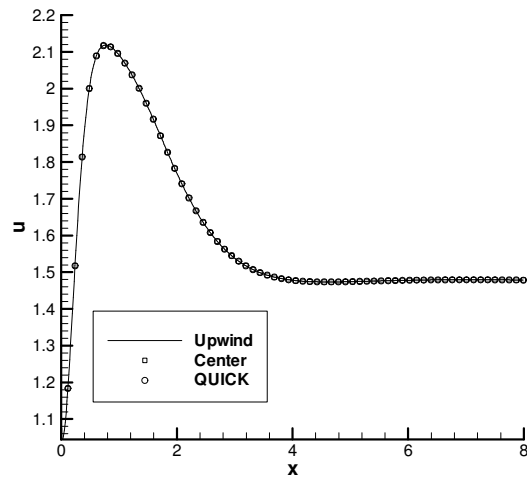


Figure 5.3. Comparison of the centerline velocity for three different schemes at $We=1$ and $Re \ll 1$ with Oldroyd-B model.

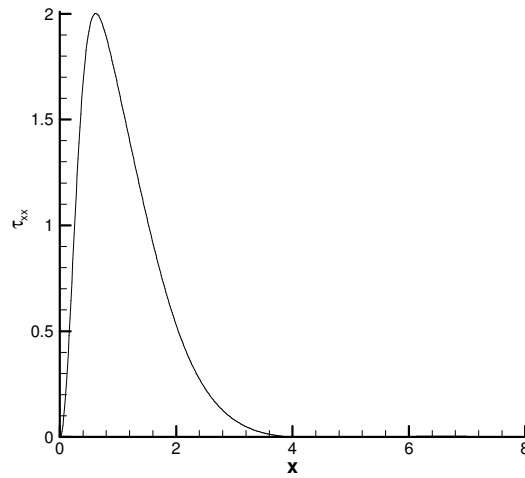


Figure 5.4. Stress components τ_{xx} at the centerline at $We=1$ and $Re \ll 1$ by Oldroyd-B model.

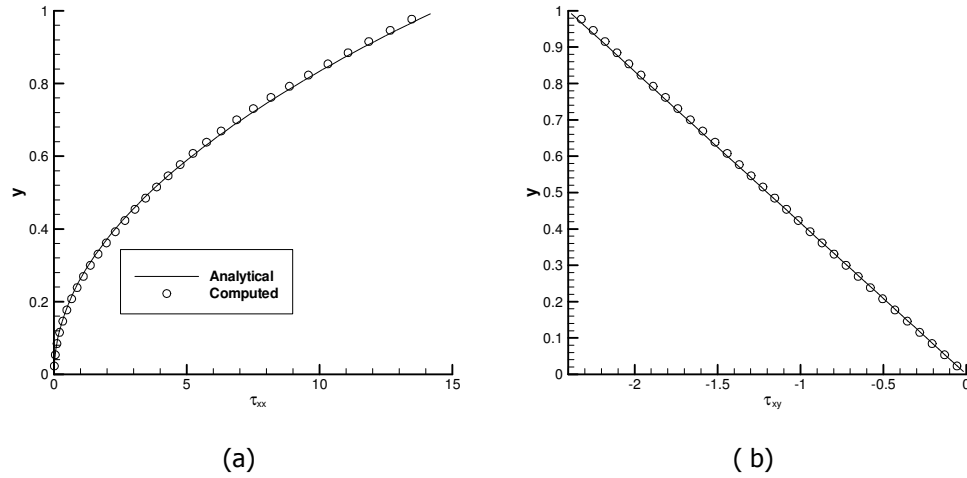


Figure 5.5. Comparison of computed and analytical profiles of (a) normal and (b) shear stresses near exit of the channel at $We=1$ and $Re \ll 1$ by Oldroyd-B model.

Numerical results of the developed normal and shear stresses are shown in Figures 5.5a-b along with their corresponding analytical solutions [72]. The results show that excellent agreement between the simulation results and those of the analytical solutions is obtained. In order to demonstrate effect of the fluid inertia on the numerical solution, simulations are carried out over a wide range of Re including 1 and 10. We were able to obtain converged solution at Re and $We=1$ (see Figure 5.6) with all schemes. At $Re=10$ and $We=1$, on the other hand, no schemes yielded a converged solution for the same channel length. Increasing the channel length to $12H$ and $16H$ did not improve the solutions in terms of converge, either. The numerical results of centerline velocity at Reynolds number 10 are presented for two different channel length in Figure 5.7 a) and b). We concluded that maximum attainable Weissenberg number is strongly dependent on Reynolds number. This is in parallel with the results of Gaidos and Darby [20] while is in contrast with that of Na and Yoo [51].

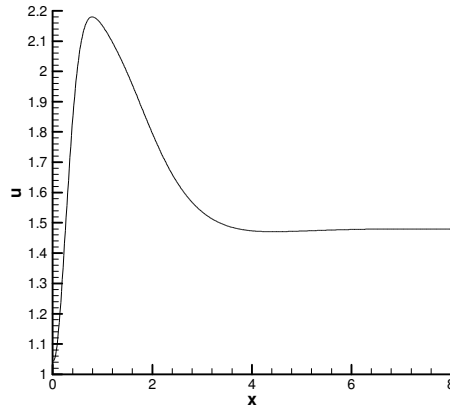


Figure 5.6. Centerline velocity for $We=1$ and $Re=1$ with Oldroyd-B model.

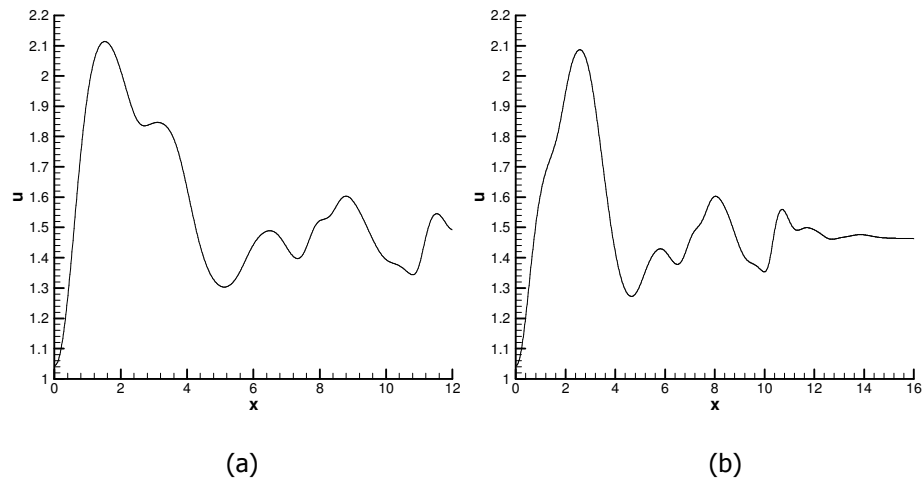


Figure 5.7. Centerline velocity at $We=1$ and $Re=10$ with channel length of a) $12H$ and b) $16H$ with Oldroyd-B model.

The viscoelastic entry length flow was also investigated using the equations governing the flow of single-mode PTT model. In addition to Oldroyd-B model, simulations using PTT model were also carried out. Polymer viscosity term, $w_r = (1 - \beta)$, in the model was set as 0.8. Also, the material parameter, ε , which controls both shear-thinning and extension properties [24] is chosen as 0.25. The centerline velocity and stress profiles obtained by using PTT model are depicted in Figure 5.8 and in Figure 5.9 respectively at two different We and $Re \ll 1$. Increasing shear thinning at higher We is captured in the simulations. Smooth centerline velocity is obtained even at high We of two which is well above the We

limit of one in the Oldroyd-B case. Figure 5.10 shows centerline velocity profiles obtained by Oldroyd-B and PTT differential models for creeping flow conditions at $We=1$. It can be seen; PTT model predicted more smooth profiles than Oldroyd-B. The main difference between the models is with their maximum attainable We . Oldroyd-B model simulations become unstable at $We=1$. With PTT model, We number could be increased up to 3.

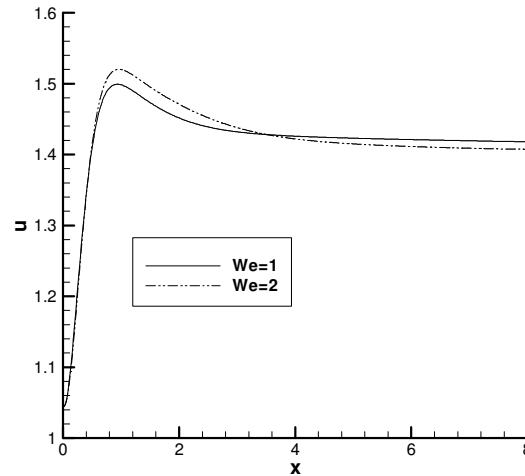


Figure 5.8. Effect of the We on centerline velocity for $Re \ll 1$ with PTT model.

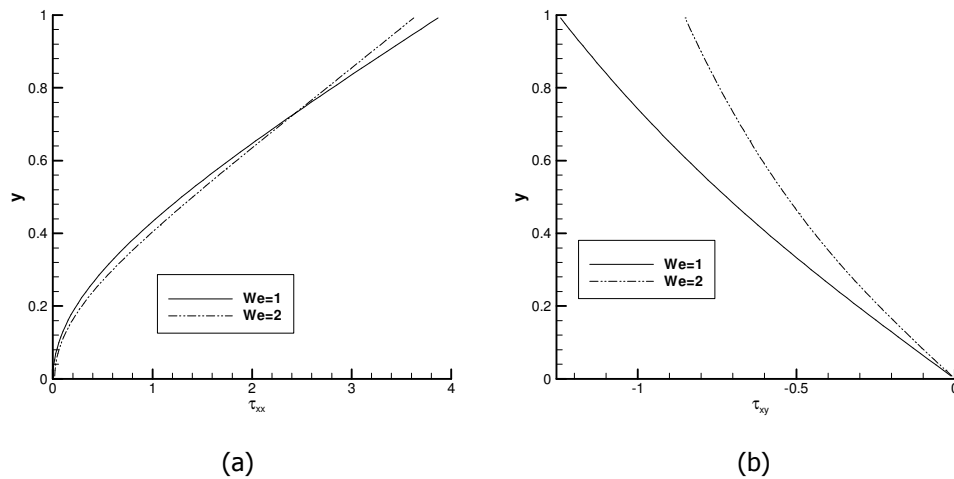


Figure 5.9. Computed profiles of (a) normal and (b) shear stresses at near the exit of the channel for $Re \ll 1$ at two different We for PTT model.

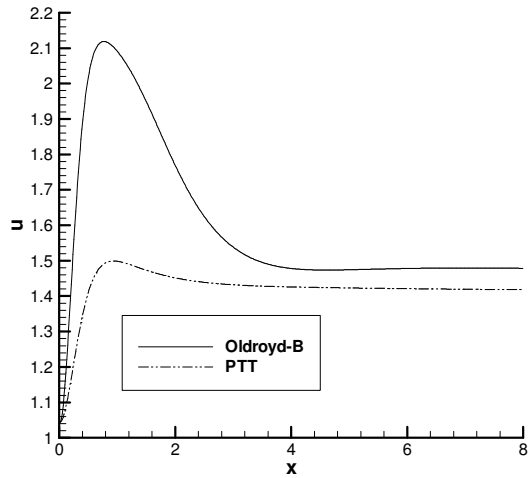


Figure 5.10. Centerline velocity profiles between constitutive models Oldroyd-B and PTT at $We=1$ for $Re \ll 1$.

Finally the effects of using White-Metzner constitutive model on the simulations are investigated. All the other flow conditions are identical to those of simulations using Oldroyd-B and PTT models. The material parameters of the model are tabulated in Table 5.1. Numerical results of the developing velocity at the centerline are presented in Figure 5.11 at various We for $Re \ll 1$. It can be seen that White-Metzner model exhibits shear-thinning behaviors similar to the PTT model. At high We this trend disappears. Numerical results of the normal and shear stresses are shown in Figures 5.12 at various We values. Their magnitude decreases with increasing We . We were able to obtain converged solution up to $We = 4$ using parameters listed in Table 5.1. Some of the parameters in Table 5.1 were used previously to simulate general non-linear constitutive equation by Gaidos and Darby [20]. If we compare stability and maximum attainable We using the same channel length, grid points and flow conditions, we can say that White-Metzner model is the most stable model. This fact is confirmed by Figure 5.13 which shows that developing centerline velocity obtained by using White-Metzner constitutive model is fairly smooth and does not appear any overshooting near the entrance of the channel.

All the results indicate that maximum achievable We is very sensitive to Re as well as to used constitutive model. However, all constitutive models which are used in the simulation of channel flow suffered from high We ($We > 5$) problem. We did not observe any differences

among schemes which are used to approximate convective terms in the momentum equations. In other words limiting We was the same for schemes.

Table 5.1. Material parameters used in White-Metzner model

| Parameters | w_r | σ | ε | α | β |
|------------|-------|----------|---------------|----------|---------|
| Values | 0.8 | 0.42 | 0.5 | 0.171 | 0.492 |

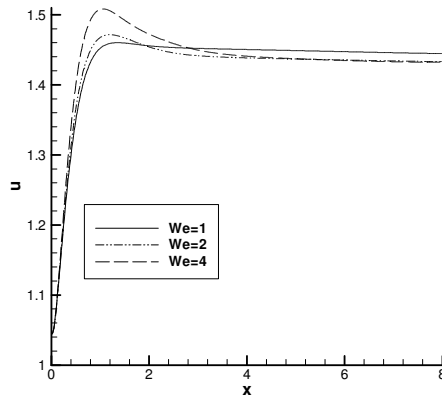


Figure 5.11. Effect of the We on centerline velocity for $Re \ll 1$ with White-Metzner model.

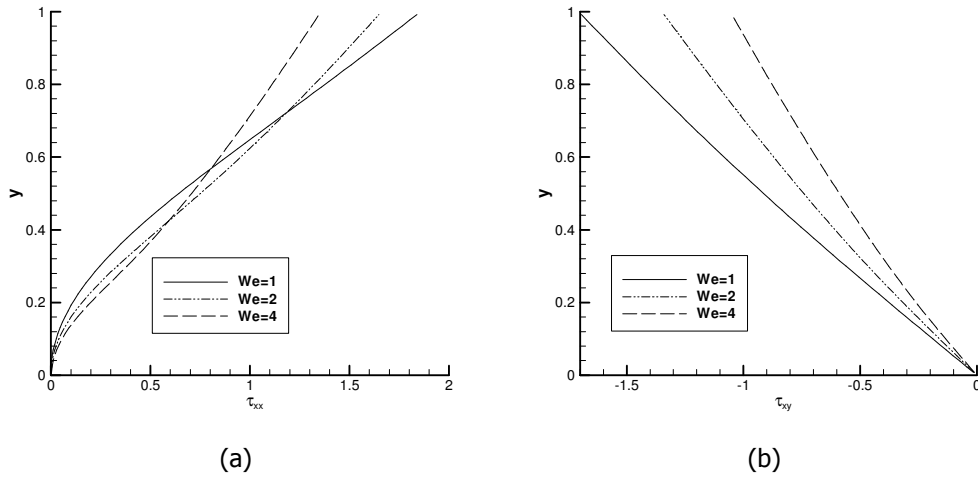


Figure 5.12. Profiles of (a) normal and (b) shear stresses near channel exit for $Re \ll 1$ at various We with White-Metzner model.

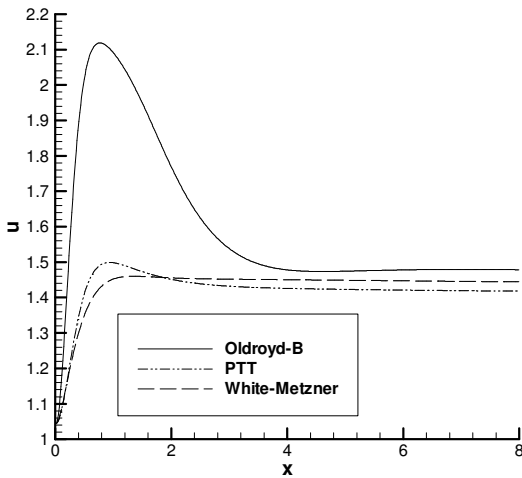


Figure 5.13. Effect of the constitutive models on predicted centerline velocity profiles at $We=1$ for $Re \ll 1$.

5.2. STICK-SLIP FLOW

Another test case, we have considered is the stick-slip geometry where boundary conditions change suddenly from no slip to perfect slip [12] as shown in Figure 5.14. Steady incompressible three constitutive models given in Chapter 2 are applied to the stick-slip geometry, which has stick length of $8H$ and slip length of $16H$. At the inlet, the flow is assumed to be plug flow except at the immediate vicinity of the wall. In addition, stress components and pressure correction boundary values are specified as described in the previous section.

To investigate impact of the abrupt change of the boundary conditions on the flow field as well as solution algorithm, stick-slip flow problem has been studied in the simulation of the viscoelastic flows in many studies [12, 25, 73-76]. Al Moatassime and Jouron [76] employed finite differences method on a non-uniform staggered grid arrangement to the discretize of the governing flow of Oldroyd-B fluid. They solved stick-slip flow problem as well as four to one contraction by using the fall approximation storage (FAS) multigrid method. For the Oldroyd- B model, they were able to simulate stick-slip flow problem up to We of 10. However, they have imposed fully developed Poiseuille flow in the entry region. They set the maximum velocity at the center as 0.333. Due to nonlinear relations between stress and

velocity field, extremely large stress peak was observed at the abrupt boundary change point. This high sensitivity become stronger as We increases [44]. We believe that, at the entrance region, streamwise velocity components should be set uniform [25] to test limiting value of the We .

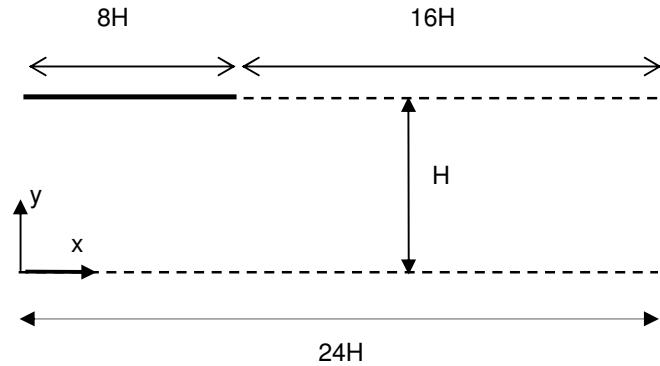


Figure 5.14. Stick-slip flow geometry

Below numerical results with polymer viscosity, $w_r = (1 - \beta)$, of 0.8 in the Oldroyd-B model are presented at Re of 1×10^{-4} . We used uniform collocated grids of contain 65 grid points in y -direction. Second order central differences scheme was used for the approximation of the convective terms in momentum equations. Figure 5.15 shows the velocity development profiles along the top boundary (see Figure 5.15 (a)) and center line (see Figure 5.15 (b)) at various values of We for $Re \ll 1$. The effect of the high We is to decrease the slope of the velocity profiles [75, 76] and to increase down stream channel length. This result can be expected since as We gets higher, it takes longer distances for the flow to relax after sudden no-slip boundary. Computed normal and shear stress components are presented along the top boundary in Figure 5.16 and 5.17, respectively. In addition, to demonstrate effect of the abrupt change of boundary, normal stress of τ_{xx} close the top boundary ($y=0.9923$) is also plotted in Figure 5.16 (b). At points where boundary changes suddenly from slip to perfect no slip, normal stress grows enormously and its dimensionless magnitude increases up to 1100 at Weissenberg number 1.5. This sudden huge increase in the normal stress causes large oscillation in the velocity and stress field.

Al Moatassime and Jouron [76] have computed normal stress value at singularity point as approximately 10 for We of 1, while in our computation this magnitude is nearly 550, providing possible explanation for the difference there between two simulations limit

Weissenberg number. All figures demonstrate that after We of 1 oscillations appear and increases as We gets higher. Another important concern in numerical simulation of viscoelastic fluids is mesh refinement. The convergence of the numerical scheme is very sensitive to mesh refinement. For instance as number of the grid points increases, attainable maximum We decreases due to large gradients over the smaller distances. This fact contradicts with the Newtonian flow simulation [63]. Profiles of normal stress components of τ_{xx} are shown in Figure 5.18 for two different meshes, M1 and M2 that respectively contain 65 and 33 grid points in y -direction. Here, We is 1.5 and $Re \ll 1$. The effect of having lower grid is to decrease the magnitude of the stress peak at the singularity point giving rise to non-oscillatory stress field. Although, using low number of grids allows one to get stable solutions at relatively high We , accurate approximation of the stress field entails a refined mesh [44].

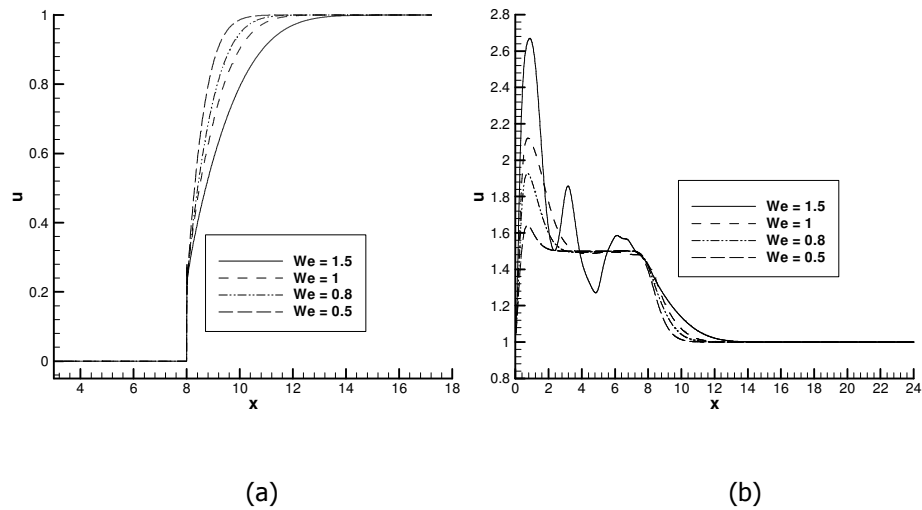


Figure 5.15. Velocity profiles along the a) top boundary b) center line at various values of We for $Re \ll 1$ by Oldroyd-B model.

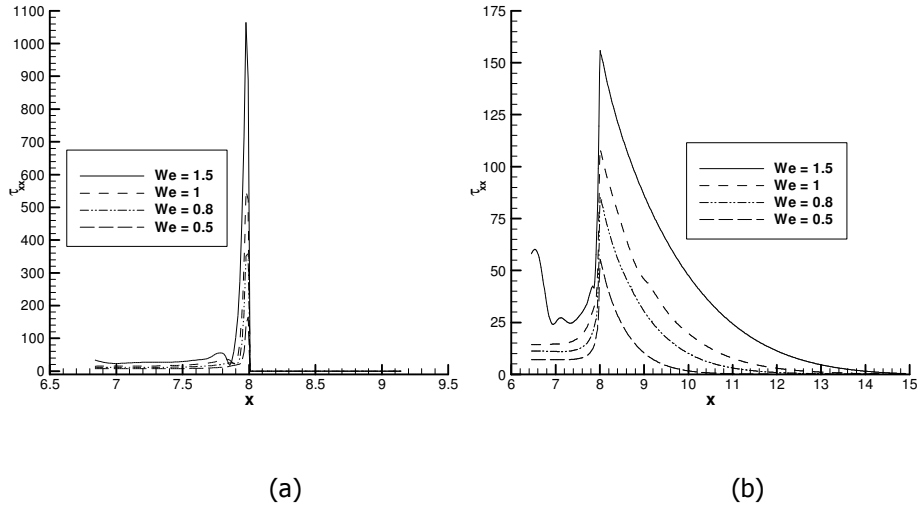


Figure 5.16. Normal stresses, τ_{xx} , profiles along a) top boundary b) close to top boundary ($y= 0.9923$) at various values of We for $Re \ll 1$ by Oldroyd-B model.

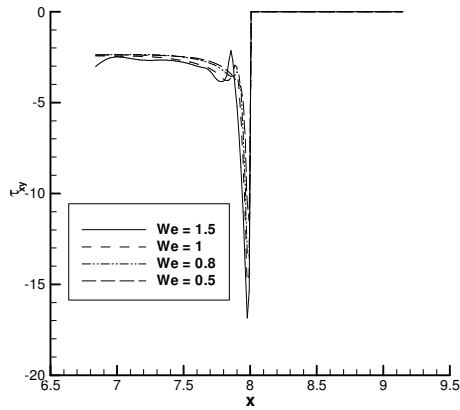


Figure 5.17. Shear stresses, τ_{xy} , profile along top boundary at various values of We for $Re \ll 1$ by Oldroyd-B model.

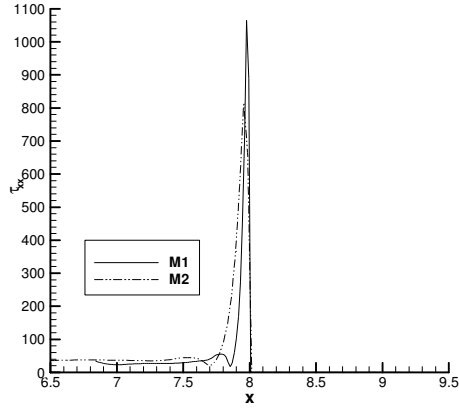


Figure 5.18. Normal stresses, τ_{xx} , profiles along top boundary using two different uniform mesh M1 and M2 having 66 and 33 grid points in y-direction at $We=1.5$ and $Re \ll 1$ by Oldroyd-B model.

Second constitutive model that is considered to simulate stick-slip flow is single-mode PTT model. We have chosen polymer viscosity, $w_p = 0.8$, and material parameter, $\varepsilon = 0.25$. Velocity development profiles along the top boundary and center line at two values of We for $Re \ll 1$ are shown in Figure 5.19. The horizontal developing velocity component exhibits different behavior from the flow of Oldroyd-B fluids at both locations. Overshoot and undershoot are observed. They get more pronounced as We increases. Stress components of normal and shear stress along the top boundary are shown in Figure 5.20. The values of the maximum normal stress and shear stress at singularity point are much lower than those obtained by Oldroyd-B model. Moreover, the predicted velocity and stresses profiles are smoother than Oldroyd-B model. However, loss of convergence was also observed in this geometry at We of 3 for the described material parameters. Maximum attainable We level is 2 in the case of PTT model.

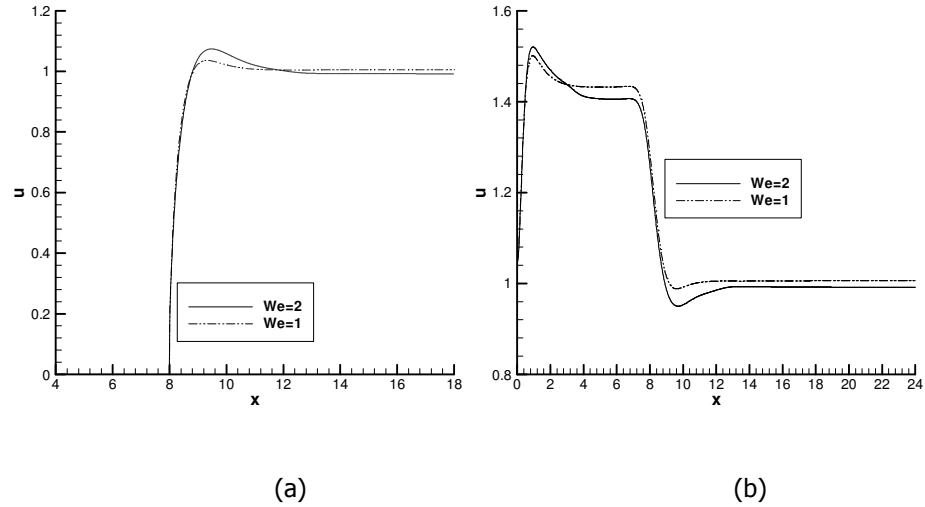


Figure 5.19. Velocity profiles along the a) top boundary b) center line at two values of We for $Re \ll 1$ with PTT model.

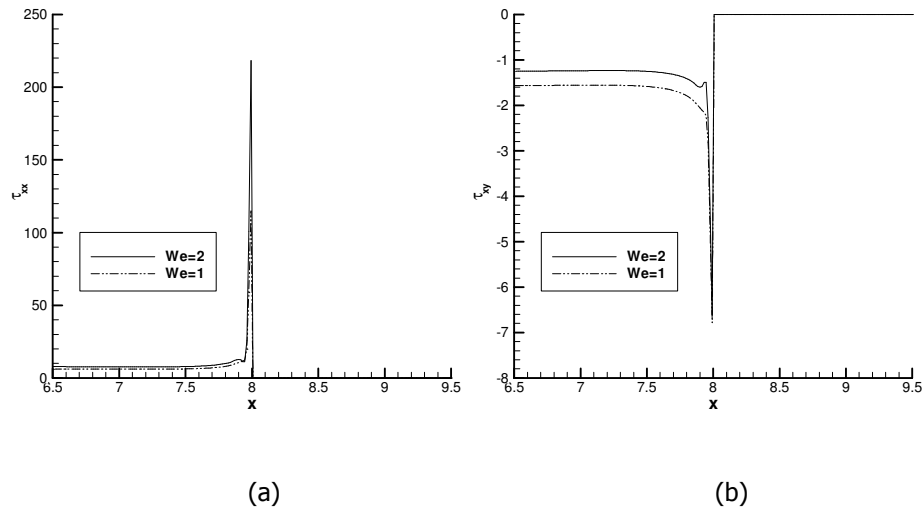


Figure 5.20. Profiles of (a) normal and (b) shear stresses along the top boundary for $Re \ll 1$ at two different We with PTT model.

The last constitutive model used in the stick-slip flow simulations is the White-Metzner model. The material parameter settings are tabulated in Table 5.1. They are the same as the values used for the channel flow simulations. Numerical results of the developing velocity along the top and centerline are presented in Figure 5.21 at We of 4 and 5 for $Re \ll 1$. It can be seen that White-Metzner model results in overshoot and undershoot along the top

and center line similar to the PTT model. Normal and shear stresses along the top boundary are shown in Figures 5.22. Calculated stress peak at the singularity point is much higher than that of PTT model but lower than the one obtained by Oldroyd-B model. We were able to obtain converged solutions up to $We = 5$ using parameters in Table 5.1. Like simple channel flow, White-Metzner model is the most stable model in the simulation of stick-slip flow. With respect to attainable maximum We and obtaining smooth solutions, the White-Metzner model seems to be superior than Oldroyd-B and PTT models.

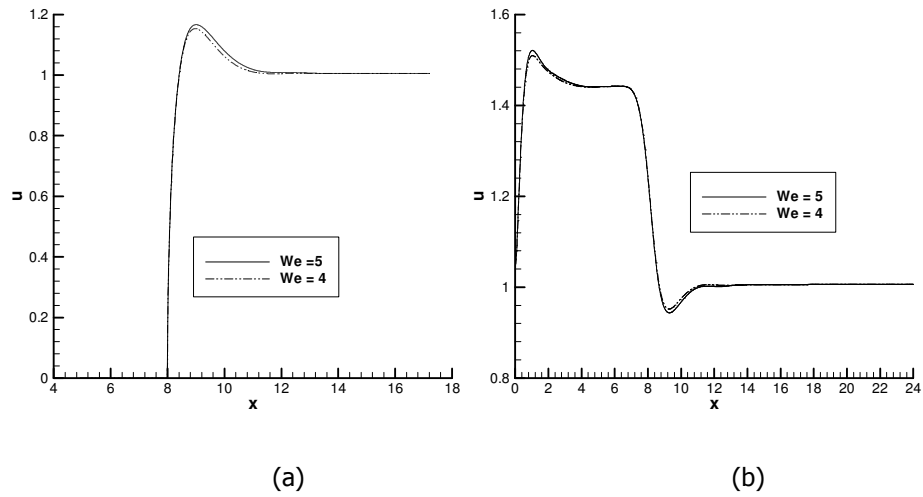


Figure 5.21. Velocity profile along the a) top boundary b) center line at two values of We for $Re \ll 1$ by White-Metzner model.

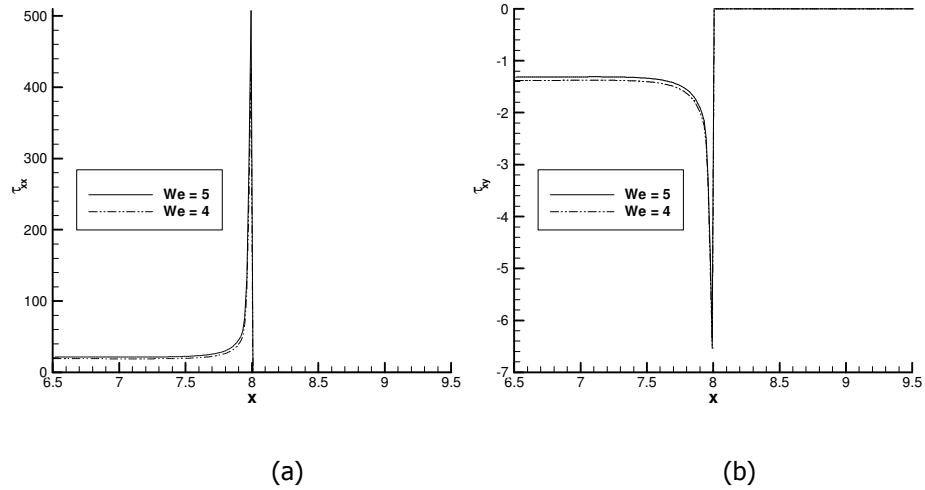
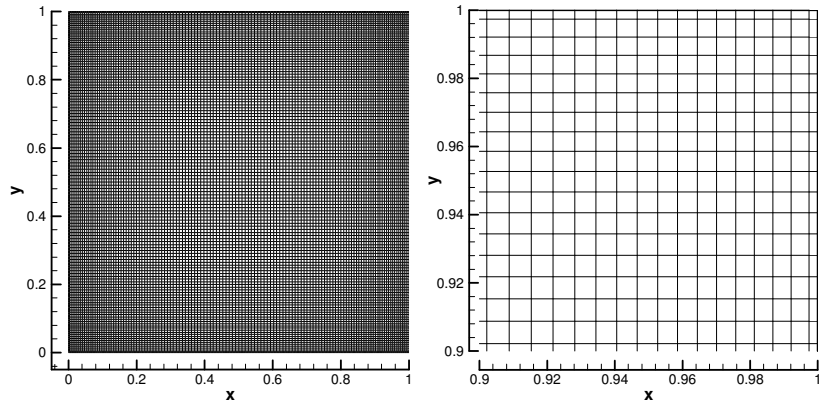


Figure 5.22. Profiles of (a) normal and (b) shear stresses along the top boundary at two We for $Re \ll 1$ using White-Metzner model.

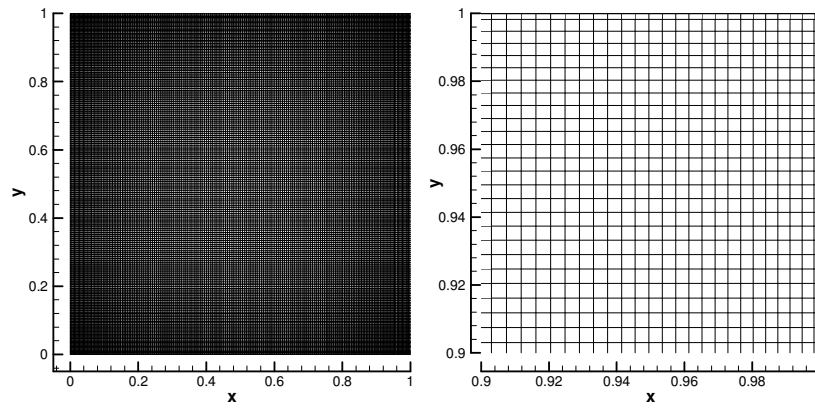
5.3. LID DRIVEN CAVITY FLOW

After verifying the computational methodology using the simple benchmarking geometries, it was proceeded with the square lid driven cavity flow of an OLDROYD-B fluid due to more challenging than PTT and White-Metzner model, for three different meshes, as shown in Figure 5.23. Mesh 1 (M1) contains 129×129 grid points and has the smallest cell area near the lid as 2.74×10^{-5} . Second mesh M2 contains 193×193 grid points and has the smallest cell area of 1.22×10^{-5} near the lid. Fine mesh contains 257×257 grid points and has the smallest cell area near the lid as 6.86×10^{-6} . Most of the results are presented for the fine mesh M3.

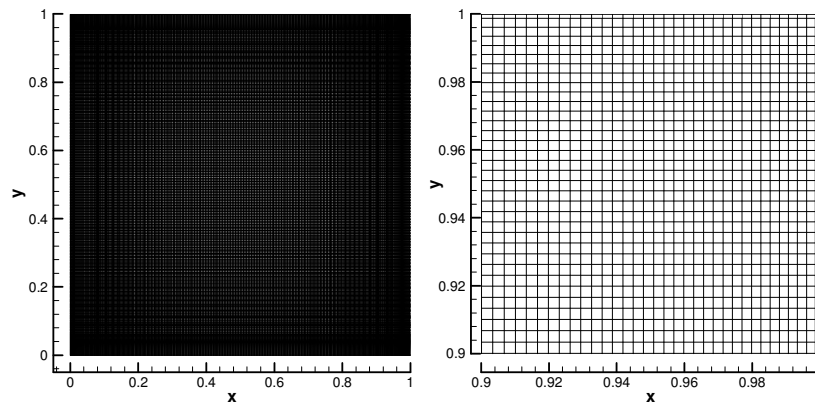
In this section, numerical results at We ranging from 0 to 1.1 are presented for three different polymer viscosities, $w_r = (1 - \beta)$ 0.7, 0.8 and 0.875. From definition of w_r in equation 2.4.9 and 2.1.8, decreasing w_r decreases polymer contribution viscosity. To investigate effect of the Re on the flow field, simulations are carried out over a wide range of Reynolds numbers including 1×10^{-4} , 100 and 400.



(a)



(b)



(c)

Figure 5.23. Non-uniform graded meshes with enlargements of right top corner (a) Mesh M1, 129x129 (b) Mesh M2, 193x193 (c) Mesh M3 257x257 grid points.

5.3.1. Boundary Conditions For Stresses

Boundary values of stress components can be determined by solving the constitutive equations with the available velocity field.

1) Top wall boundary conditions parallel to the x-axis:

$$u = 1, v = 0, \frac{\partial u}{\partial x} = 0, \frac{\partial v}{\partial x} = 0, \frac{\partial v}{\partial y} = 0$$

If we apply these conditions in the constitutive equations through (2.26-2.28) we obtain following non-linear equations

$$\tau_{xx} + \frac{\partial}{\partial x}(Weu\tau_{xx}) = 2We\left(\frac{\partial u}{\partial y}\right)\tau_{xy} \quad (5.8)$$

$$\tau_{yy} + \frac{\partial}{\partial x}(Weu\tau_{yy}) = 0 \quad (5.9)$$

$$\tau_{xy} + \frac{\partial}{\partial x}(Weu\tau_{xy}) = We\tau_{yy}\left(\frac{\partial u}{\partial y}\right) + w_r\left(\frac{\partial u}{\partial y}\right) \quad (5.10)$$

Therefore, the values of τ_{xx} , τ_{yy} and τ_{xy} on the lid are obtained by solving the set of equations above.

2) Bottom wall boundary conditions parallel to the x-axis:

If similar step procedure is applied by using the following conditions.

$$u = 0, v = 0, \frac{\partial v}{\partial x} = 0, \frac{\partial v}{\partial y} = 0, \frac{\partial u}{\partial x} = 0$$

we can obtain stress boundary conditions for the bottom wall.

$$\tau_{xx} = 2Wew_r\left(\frac{\partial u}{\partial y}\right)^2 \quad (5.11)$$

$$\tau_{yy} = 0 \quad (5.12)$$

$$\tau_{xy} = w_r \left(\frac{\partial u}{\partial y} \right) \quad (5.13)$$

3) Solid walls boundary conditions parallel to the y-axis (left and right wall):

The values of τ_{xx} , τ_{yy} and τ_{xy} at the solid walls are evaluated through the following conditions.

$$u = 0, v = 0, \frac{\partial u}{\partial y} = 0, \frac{\partial v}{\partial y} = 0, \frac{\partial u}{\partial x} = 0$$

$$\tau_{xx} = 0 \quad (5.14)$$

$$\tau_{yy} = 2We w_r \left(\frac{\partial v}{\partial x} \right)^2 \quad (5.15)$$

$$\tau_{xy} = w_r \left(\frac{\partial v}{\partial x} \right) \quad (5.16)$$

The boundary conditions on pressure-correction are of Neumann type for all boundaries.

5.3.2. Results at $Re \ll 1$

At creeping flow conditions, the stream functions and vorticity at different polymer viscosity, w_r , and We are depicted in Figures 5.24 and 5.25 respectively. Results of $w_r = 0.875$, $w_r = 0.8$ and $w_r = 0.7$ are given at top, middle and bottom of these figures, respectively. Stream function, ψ , and vorticity, ω , are obtained by solving the following equations after convergence is attained.

$$\nabla^2 \psi = -\omega \quad (5.17)$$

$$\omega = -\frac{\partial u}{\partial y} + \frac{\partial v}{\partial x} \quad (5.18)$$

In Newtonian cavity simulations, stream function and vorticity values and their locations are usually taken as a code validation. At $We = 0$ and $Re = 0$, i.e. Stokes flow, fore-aft symmetry is observed, a typical Newtonian fluid behavior. However, for a viscoelastic fluid, as the value of We increases the primary vortex shifts in the upstream direction (see Figure

5.26) and streamlines near the downstream corners become more curved due to the increased normal stress effects. This phenomenon was also observed experimentally by Pakdel et al. [45] using laser Doppler velocimetry (LDV) and digital particle image velocimetry (DPIV). The effect of the elasticity is more pronounced at the downstream than the upstream due to the finite relaxation of the normal stresses for all w_r , as shown by the vorticity contours in the Figure 5.25.

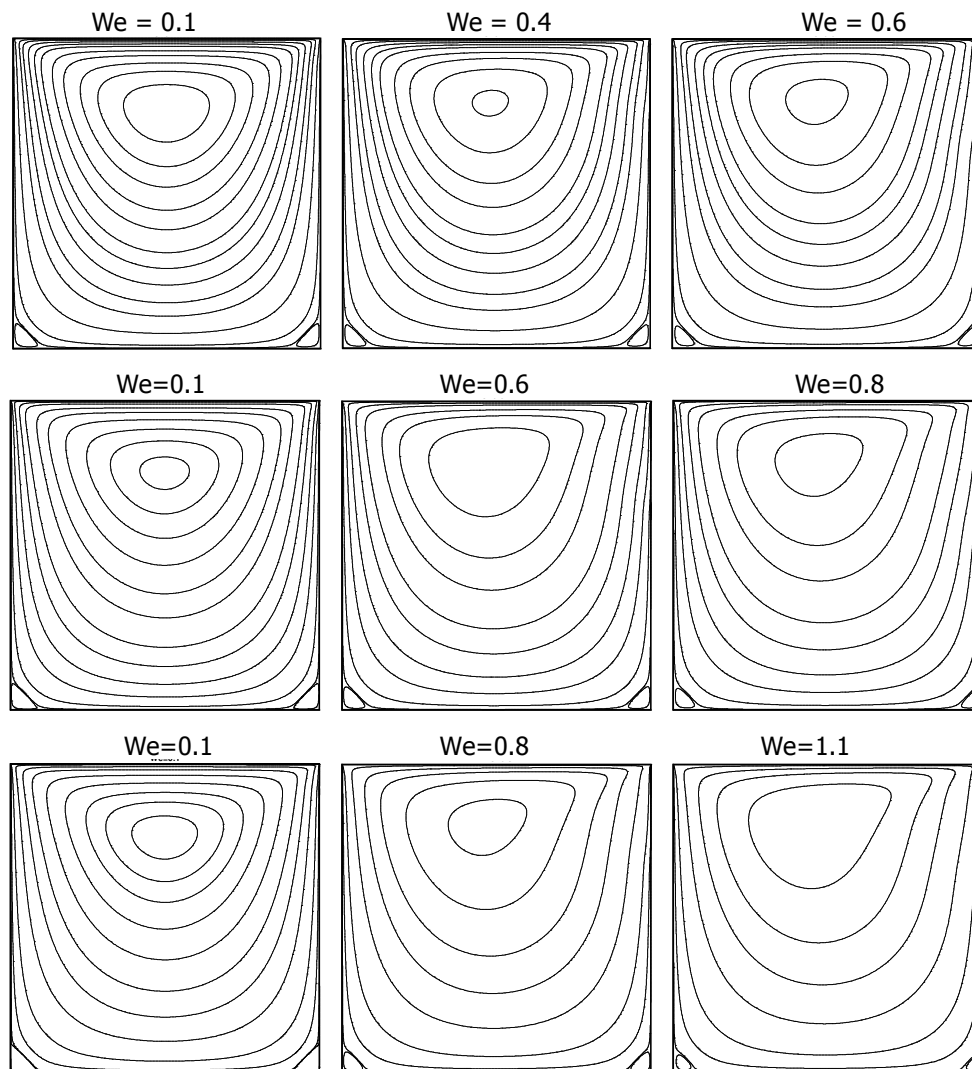
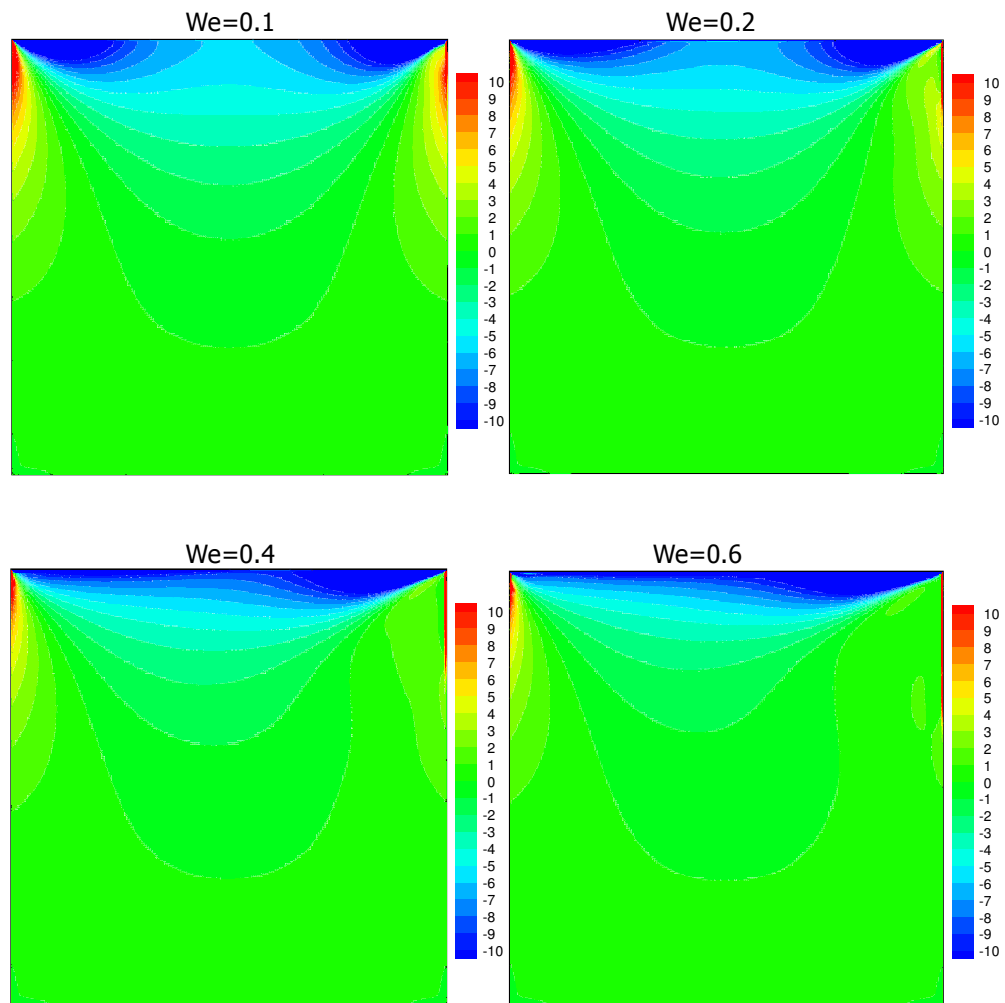
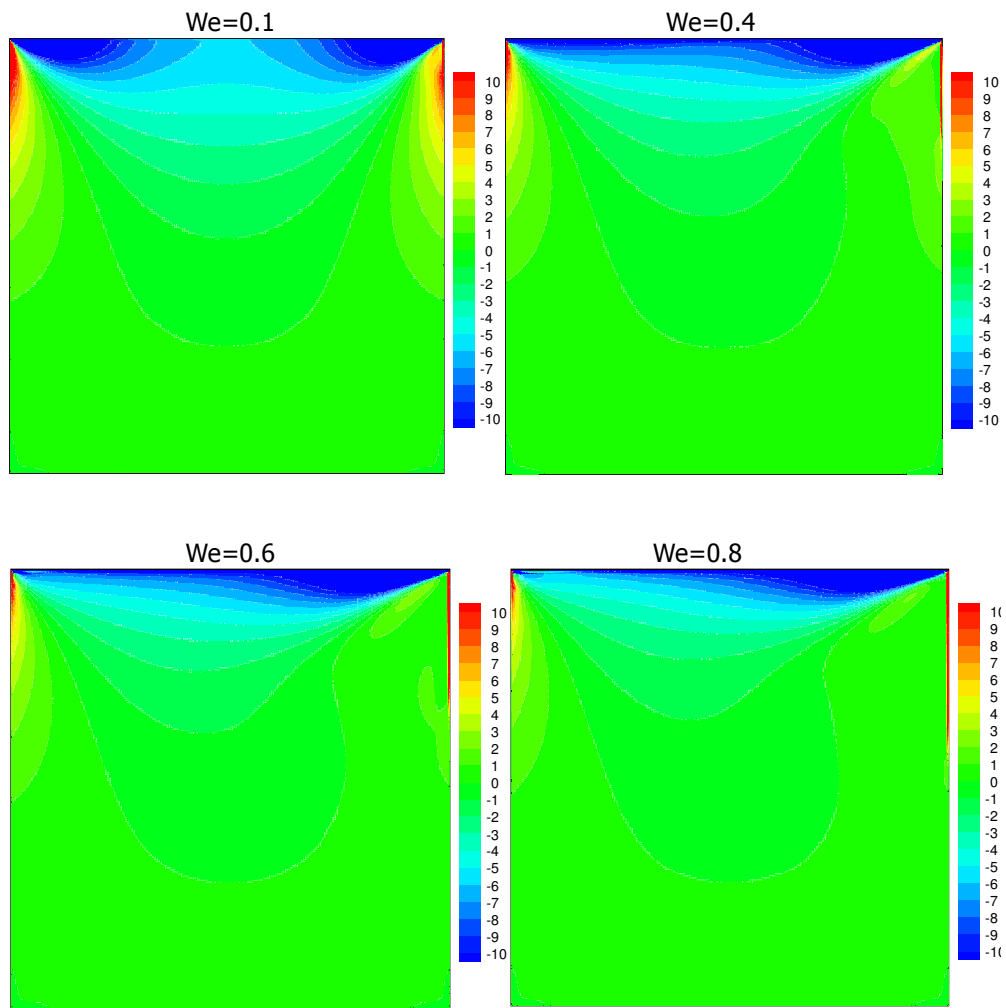


Figure 5.24. The stream functions at top $w_r = 0.875$, middle $w_r = 0.8$, bottom $w_r = 0.7$, for different We and at $Re = 0$



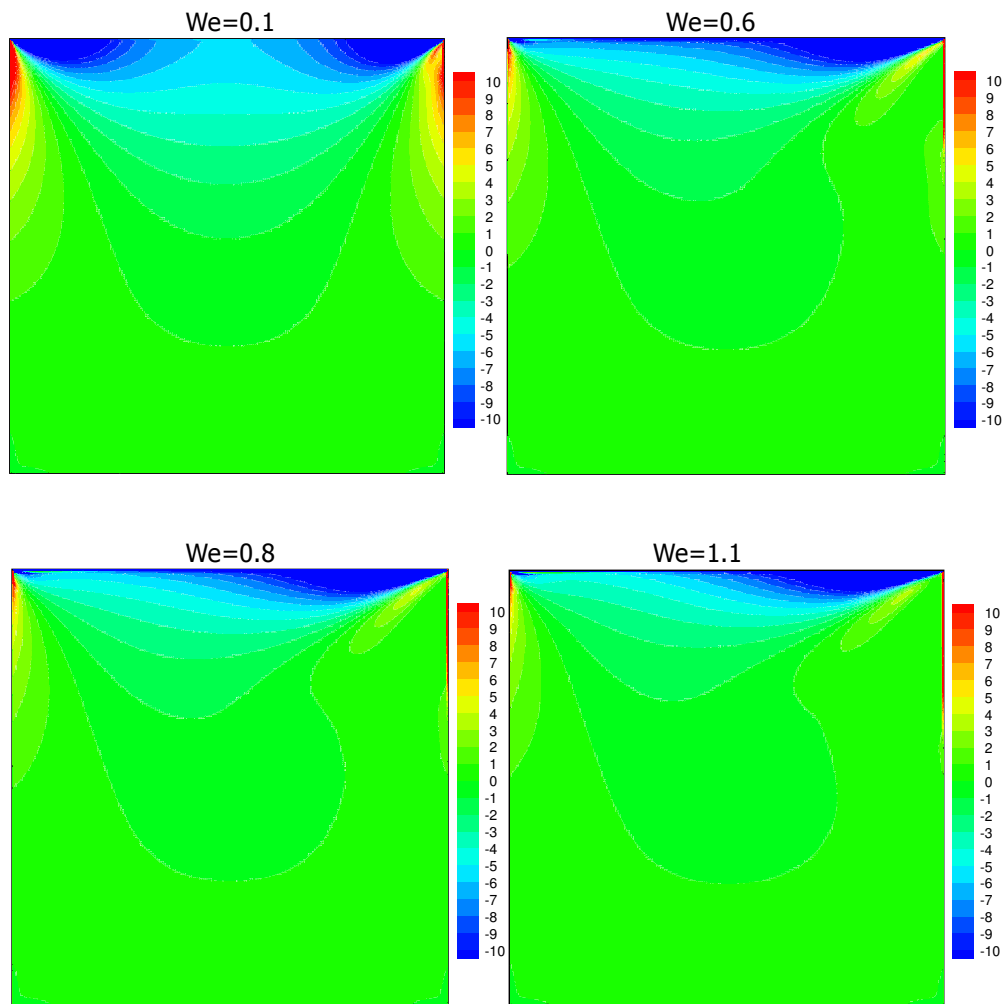
(a)

Figure 5.25. The vorticity contour a) $w_r = 0.875$, b) $w_r = 0.8$, c) $w_r = 0.7$, for different We and at $Re=0$. Contour levels are shown from -10 to 10 with increment of 1.



(b)

Figure 5.25. The vorticity contour a) $w_r = 0.875$, b) $w_r = 0.8$, c) $w_r = 0.7$, for different We and at $Re=0$. Contour levels are shown from -10 to 10 with increment of 1. (continued)



(c)

Figure 5.25. The vorticity contour a) $w_r = 0.875$, b) $w_r = 0.8$, c) $w_r = 0.7$, for different We and at $Re=0$. Contour levels are shown from -10 to 10 with increment of 1. (continued)

Figures 5.27 and 5.28 show the effect of We on the horizontal (u) and vertical (v) velocity components distribution at $x=0.5$ and $y=0.5$, respectively. With increasing We , maximum magnitudes of the velocity components decrease as expected.

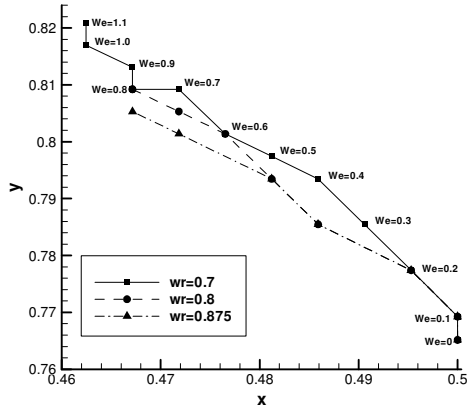
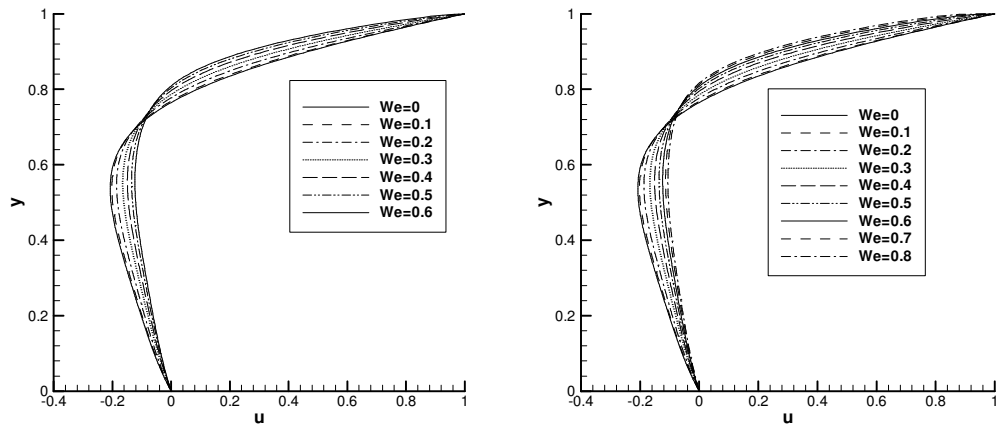


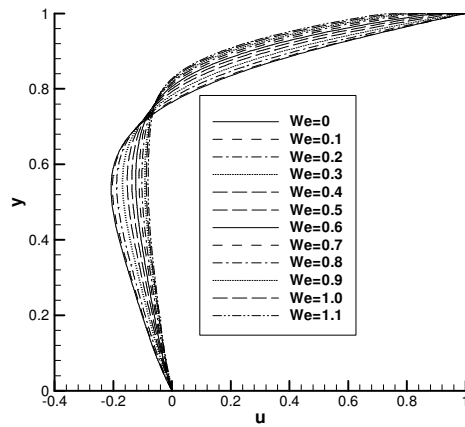
Figure 5.26. Primary vortex center location as a function of We and w_r for $Re=0$.

The maximum and minimum values of the velocity components at the corresponding centerlines are also given in Table 5.2 along with their locations. Here subscripts denote values pertaining to the minimum and maximum velocities. The results obtained at $We=0$ compares well with those of a Newtonian fluid study [65]. Vertical position of u_{min} shifts upward. Horizontal positions of the v_{max} and v_{min} , on the other hand, decrease as a function of We . As the Newtonian viscosity increases, in other words polymer contribution viscosity decreases the maximum attainable converged values of We increases. For $w_r = 0.875, 0.8$ and 0.7 , maximum We reached are $0.6, 0.8$ and 1.1 , respectively.



(a)

(b)



(c)

Figure 5.27. Effects of We on u at vertical centerline ($x=0.5$) for (a) $w_r = 0.875$ (b) $w_r = 0.8$ (c) $w_r = 0.7$ at $Re=0$.

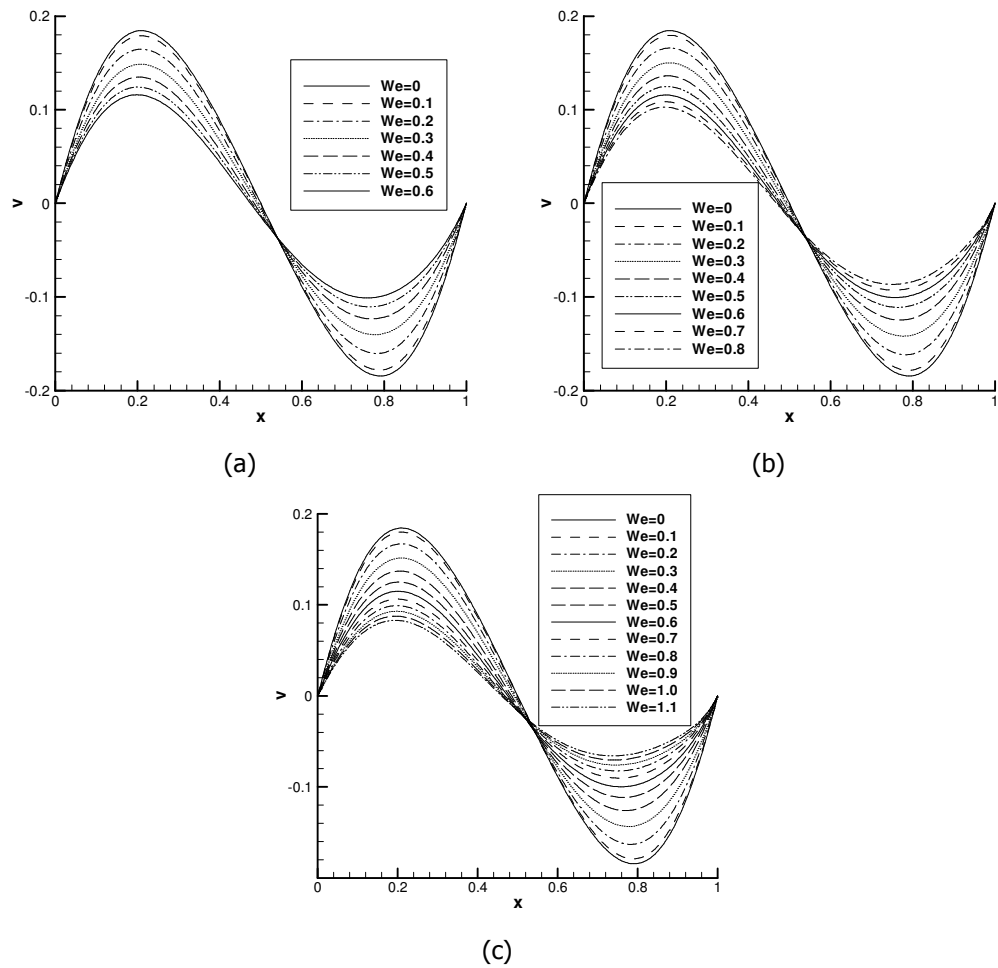


Figure 5.28. Effects of We on v at horizontal centerline ($y=0.5$) for (a) $w_r = 0.875$ (b) $w_r = 0.8$ (c) $w_r = 0.7$ at $Re=0$.

The effect of We on the magnitude and location of the center of the primary eddy are listed in Table 5.3. The stream function values at the center of the primary eddy decrease as We gets higher for each w_r . Other impact of the increasing We is that the position of the primary eddy center moves slightly toward the upstream corner of the lid. Effect of the polymer viscosity is clearly depicted in Figure 5.29, where upstream and downstream bottom corner streamlines with value of 0 are plotted at different We (the arrows point increasing We from 0 to the maximum value depicted in Table 5.3). Magnitudes and locations of the upstream secondary eddy (USE) and downstream secondary eddy (DSE) for each We at $w_r = 0.875$ are similar (see Figure 5.29 top). That means there is no reduction in height and width of the

USE and DSE. When w_r decreases (see Figure 5.29 middle and bottom) USE and DSE height and width begin to shrink with increasing We .

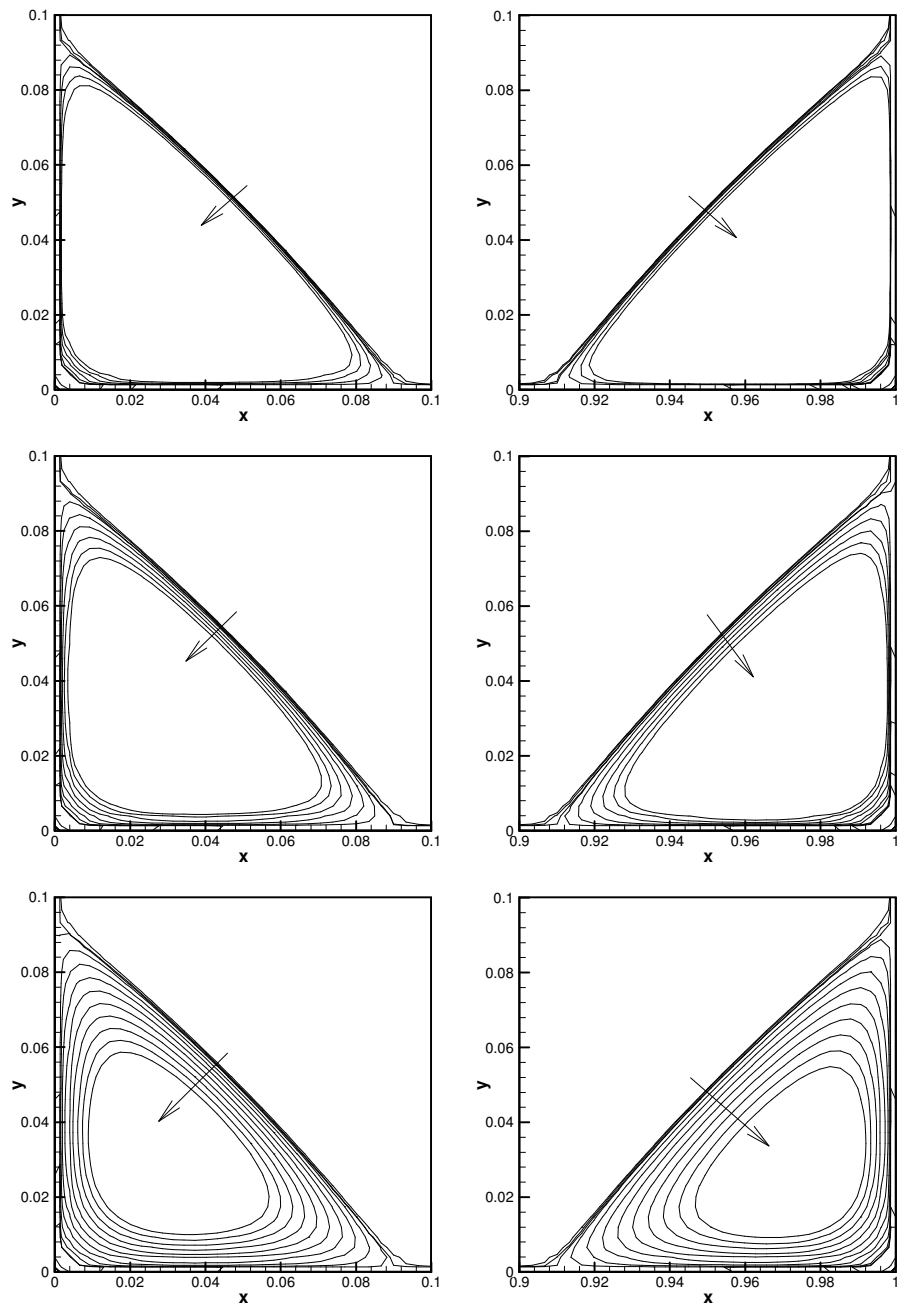


Figure 5.29. Comparison of the eddy sizes USE and DSE as a function of We in terms of contour level at top $w_r = 0.875$, middle $w_r = 0.8$, bottom $w_r = 0.7$ for $Re = 0$.

Table 5.2. Horizontal minimum velocity, vertical minimum and maximum velocity through the centerlines of the cavity at $Re=0$.

| We | Reference | U_{min} | Y_{min} | V_{max} | X_{max} | V_{min} | X_{min} |
|---------------|-----------|-----------|-----------|-----------|-----------|-----------|-----------|
| 0 | Present | -0.207703 | 0.537543 | 0.181364 | 0.210522 | -0.181364 | 0.789478 |
| | [65] | -0.207754 | 0.537600 | 0.186273 | 0.210500 | -0.186273 | 0.789400 |
| $w_r = 0.875$ | | | | | | | |
| 0.1 | Present | -0.202034 | 0.537543 | 0.176042 | 0.210522 | -0.175110 | 0.789478 |
| 0.2 | Present | -0.186088 | 0.546907 | 0.161904 | 0.210522 | -0.157802 | 0.781445 |
| 0.3 | Present | -0.166914 | 0.551583 | 0.146044 | 0.206535 | -0.138094 | 0.777400 |
| 0.4 | Present | -0.149482 | 0.556256 | 0.132502 | 0.206535 | -0.121522 | 0.769254 |
| 0.5 | Present | -0.135287 | 0.556256 | 0.122030 | 0.202567 | -0.108905 | 0.765154 |
| 0.6 | Present | -0.123995 | 0.556255 | 0.113942 | 0.198618 | -0.099566 | 0.761033 |
| $w_r = 0.8$ | | | | | | | |
| 0.1 | Present | -0.202458 | 0.537543 | 0.176462 | 0.210522 | -0.175508 | 0.789478 |
| 0.2 | Present | -0.187380 | 0.546907 | 0.163106 | 0.210522 | -0.159068 | 0.781445 |
| 0.3 | Present | -0.168658 | 0.551583 | 0.147554 | 0.206535 | -0.139630 | 0.777400 |
| 0.4 | Present | -0.151202 | 0.556256 | 0.133855 | 0.206535 | -0.122739 | 0.769254 |
| 0.5 | Present | -0.136325 | 0.556256 | 0.122658 | 0.202567 | -0.109379 | 0.765154 |
| 0.6 | Present | -0.124182 | -0.124182 | 0.113689 | 0.198619 | -0.099110 | 0.756898 |
| 0.7 | Present | -0.114430 | 0.556256 | 0.106572 | 0.198619 | -0.091309 | 0.752744 |
| 0.8 | Present | -0.106548 | 0.556256 | 0.100908 | 0.198619 | -0.085277 | 0.752744 |
| $w_r = 0.7$ | | | | | | | |
| 0.1 | Present | -0.203008 | 0.537543 | 0.176990 | 0.210522 | -0.176055 | 0.789478 |
| 0.2 | Present | -0.188813 | 0.542227 | 0.164324 | 0.210522 | -0.160463 | 0.781445 |
| 0.3 | Present | -0.170569 | 0.551583 | 0.148913 | 0.206535 | -0.141227 | 0.777400 |
| 0.4 | Present | -0.153022 | 0.556256 | 0.134884 | 0.206535 | -0.124003 | 0.769254 |
| 0.5 | Present | -0.137542 | 0.560924 | 0.122966 | 0.202567 | -0.109823 | 0.765154 |
| 0.6 | Present | -0.124264 | 0.560924 | 0.112968 | 0.202567 | -0.098328 | 0.756898 |
| 0.7 | Present | -0.112980 | 0.560924 | 0.104559 | 0.198619 | -0.088975 | 0.198619 |
| 0.8 | Present | -0.103401 | 0.560924 | 0.097433 | 0.198619 | -0.081276 | 0.748571 |
| 0.9 | Present | -0.095250 | 0.560924 | 0.091331 | 0.198619 | -0.074869 | 0.744382 |
| 1.0 | Present | -0.088284 | 0.556256 | 0.086082 | 0.194690 | -0.069472 | 0.740175 |
| 1.1 | Present | -0.082302 | 0.556256 | 0.081527 | 0.194690 | -0.064882 | 0.740175 |

Table 5.3. Intensities of the primary eddies as a function of Weissenberg number at $Re=0$.

| We | Reference | ψ_{min} | x_{min} | y_{min} |
|---------------|-----------|--------------|------------|------------|
| 0 | Present | -0.10007595 | 0.50000000 | 0.76515381 |
| | [66] | -0.10005400 | 0.50000000 | 0.76260000 |
| $w_r = 0.875$ | | | | |
| 0.1 | Present | -0.09789340 | 0.50000000 | 0.76925443 |
| 0.2 | Present | -0.09144949 | 0.49530326 | 0.77740029 |
| 0.3 | Present | -0.08341255 | 0.48591125 | 0.78547102 |
| 0.4 | Present | -0.07605805 | 0.48121672 | 0.79346518 |
| 0.5 | Present | -0.07007088 | 0.47183244 | 0.80138136 |
| 0.6 | Present | -0.06528044 | 0.46714342 | 0.80530980 |
| $w_r = 0.8$ | | | | |
| 0.1 | Present | -0.09805254 | 0.50000000 | 0.76925443 |
| 0.2 | Present | -0.09196584 | 0.49530326 | 0.77740029 |
| 0.3 | Present | -0.08411501 | 0.48591125 | 0.78547102 |
| 0.4 | Present | -0.07675354 | 0.48121672 | 0.79346518 |
| 0.5 | Present | -0.07046514 | 0.47652366 | 0.80138136 |
| 0.6 | Present | -0.06530458 | 0.47183244 | 0.80530980 |
| 0.7 | Present | -0.06110342 | 0.46714342 | 0.80921826 |
| 0.8 | Present | -0.05766664 | 0.46714342 | 0.80921826 |
| $w_r = 0.7$ | | | | |
| 0.1 | Present | -0.09826001 | 0.50000000 | 0.76925443 |
| 0.2 | Present | -0.09250882 | 0.49530326 | 0.77740029 |
| 0.3 | Present | -0.08482177 | 0.49060688 | 0.78547102 |
| 0.4 | Present | -0.07737952 | 0.48591125 | 0.79346518 |
| 0.5 | Present | -0.07081864 | 0.48121672 | 0.79743310 |
| 0.6 | Present | -0.06516975 | 0.47652366 | 0.80138136 |
| 0.7 | Present | -0.06034487 | 0.47183244 | 0.80921826 |
| 0.8 | Present | -0.05620550 | 0.46714342 | 0.80921826 |
| 0.9 | Present | -0.05264022 | 0.46714342 | 0.81310660 |
| 1.0 | Present | -0.04954916 | 0.46245698 | 0.81697465 |
| 1.1 | Present | -0.04685245 | 0.46245698 | 0.82082228 |

Normal stress, τ_{xx} , profiles for different values of w_r and We are presented near the downstream ($x=0.9987$) as a function of y in Figure 5.30. Increasing elasticity and polymer viscosity lead to increase in hoop stress in the vicinity of the downstream corner so that magnitude of the stress gets higher. One of the reasons of why the low polymer contributed viscosity at very high We becomes computable, may be the fact that as polymer contributed viscosity decreases. Hence this pollute the velocity field with a lower extend. As polymer viscosity increases high stress gradients cause to loss of convergence of the numerical scheme. Effects of the mesh refinement on the stress profile are shown in Figure 5.31 at $w_r=0.8$ and $We=0.8$. It can be seen that the prediction of all meshes give a similar trend while the peak near the down stream corner with fine mesh M3 becomes much higher than those of the other meshes. The maximum and minimum values of the velocity components for three different meshes at the corresponding centerlines are given in Table 5.4 along with their locations. Although predicted stress peak increases with mesh refinement, their size has little impact on the rest of the flow [10]. This can be seen clearly in Table 5.4. For instance, stress near the down stream in the case of M3 is nearly four times greater than M1 and two times than M2 (see Figure 5.31). But differences between velocities of each mesh are very little (see Table 5.4).

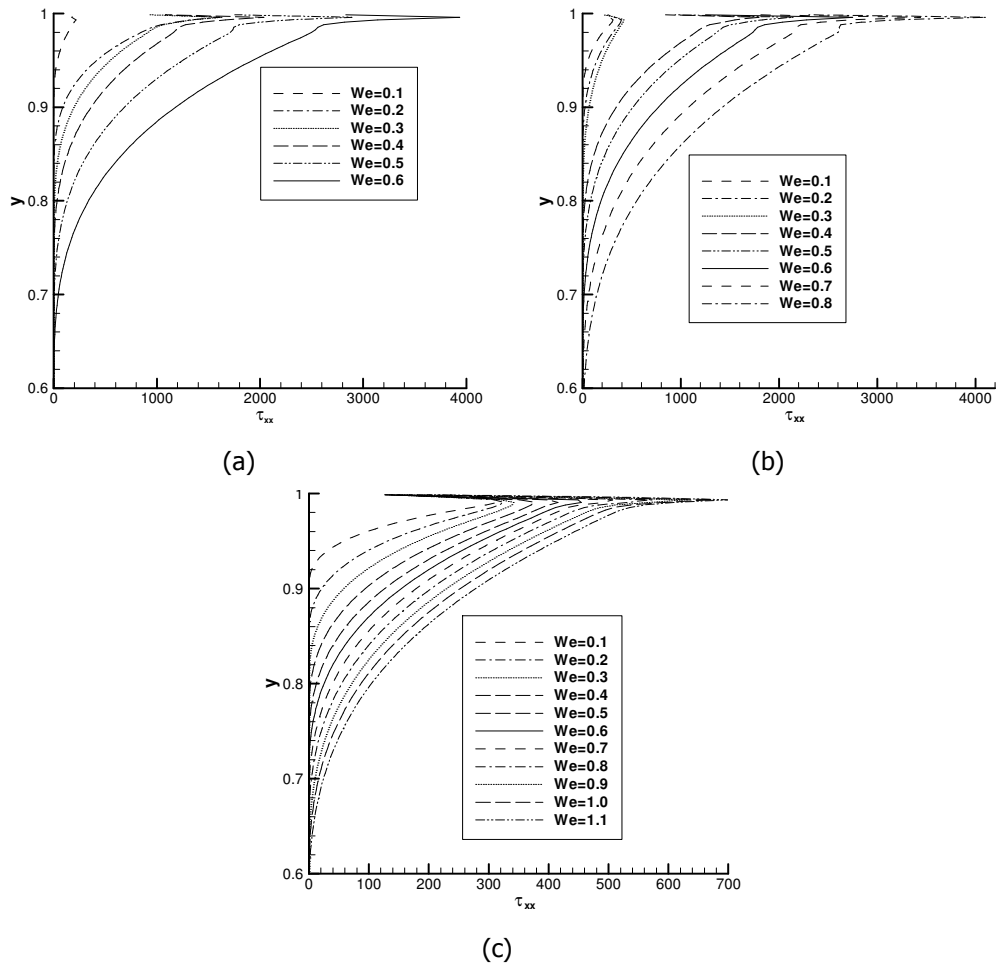


Figure 5.30. Normal stresses, τ_{xx} , near the downstream ($x=0.9987$) (a) $wr = 0.875$ (b) $wr = 0.8$ (c) $wr = 0.7$ at different We for $Re=0$.

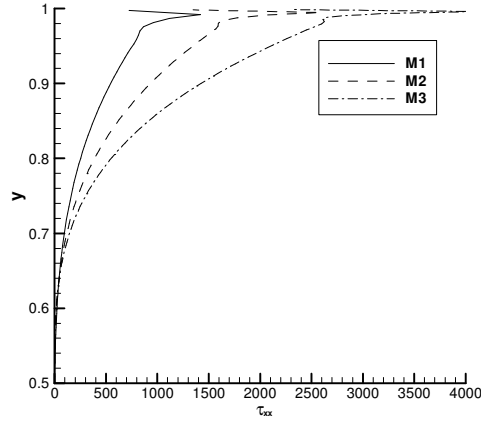


Figure 5.31. Normal stresses, τ_{xx} , stresses near the downstream ($x=0.9987$) for three different meshes at $We=0.8$ and $w_r=0.8$.

Table 5.4. Horizontal minimum velocity, vertical minimum and maximum velocity through the centerlines of the cavity with three different mesh at $Re=0$.

| | u_{min} | y_{min} | v_{max} | x_{max} | v_{min} | x_{min} |
|------------------------------|------------|-----------|-----------|-----------|------------|-----------|
| $w_r = 0.875$ and $We = 0.6$ | | | | | | |
| M1 | -0.1241959 | 0.5560386 | 0.1097893 | 0.2075530 | -0.0982472 | 0.7683024 |
| M2 | -0.1241545 | 0.5561832 | 0.1124586 | 0.1989656 | -0.0991492 | 0.7634701 |
| M3 | -0.1239950 | 0.5562550 | 0.1139420 | 0.1986180 | -0.0995660 | 0.7610330 |
| $w_r = 0.8$ and $We = 0.8$ | | | | | | |
| M1 | -0.1073025 | 0.5560386 | 0.0981493 | 0.1996574 | -0.0840592 | 0.7601066 |
| M2 | -0.1067921 | 0.5561832 | 0.0997698 | 0.1989656 | -0.0847774 | 0.7524415 |
| M3 | -0.1065484 | 0.5562558 | 0.1009084 | 0.1986186 | -0.0852773 | 0.7527436 |

5.3.3. Results at $Re=100$

The impact of the non-linear inertial terms in the Cauchy stress equation gets amplified as Reynolds number increases and eventually flow becomes unstable when a critical Re is reached, i.e. $Re_{crit} \approx 500$ [46]. In this and following parts of the report, the effects of increasing Re (100 and 400) on the viscoelastic flow in the square lid are investigated. The velocity components through the vertical and horizontal centerline of the cavity are compared with the Weissenberg number and polymer viscosity w_r in Figures 5.32 and 5.33

and their values are tabulated in Table 5.5. As can be seen from both Figures 5.32 and 5.33 and Table 5.5, as Weissenberg number increases the minimum value of the horizontal velocity component decreases in magnitude and its location moves closer to the lid. Also, extremal values of the vertical velocity components decrease and their minimum and maximum values approaches to zero with increasing We. This trend depicts that as the elasticity increases recirculation flow inside a lid driven cavity gets restricted.

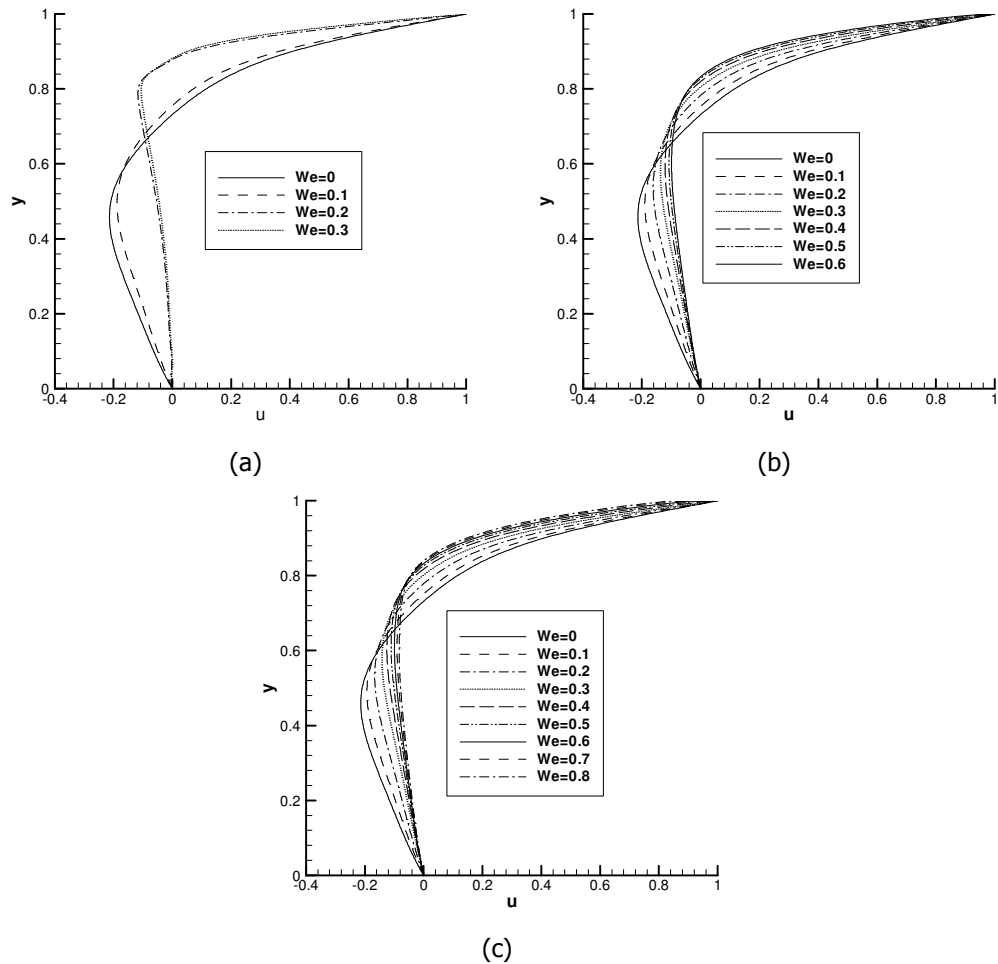


Figure 5.32. Effects of We on u at vertical centerline ($x=0.5$) for (a) $w_r = 0.875$ (b) $w_r = 0.8$ (c) $w_r = 0.7$ for $Re = 100$

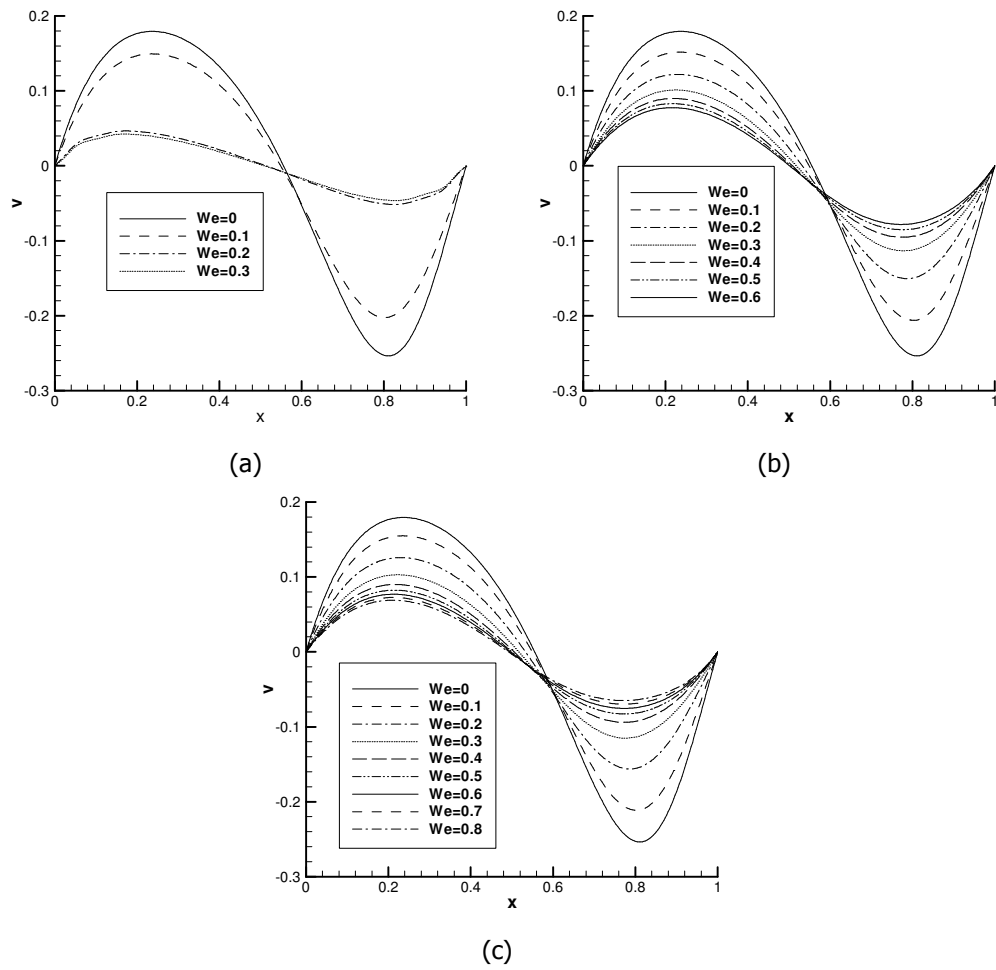


Figure 5.33. Effects of We on v at horizontal centerline ($y=0.5$) for (a) $w_r = 0.875$ (b) $w_r=0.8$ (c) $w_r = 0.7$ for $Re=100$

Table 5.5. Horizontal minimum velocity, vertical minimum and maximum velocity through the centerlines of the cavity at $Re=100$.

| We | Reference | U_{min} | Y_{min} | V_{max} | X_{max} | V_{min} | X_{min} |
|---------------|-----------|-----------|-----------|-----------|-----------|-----------|-----------|
| 0 | Present | -0.213948 | 0.4609726 | 0.179528 | 0.236738 | -0.253801 | 0.810584 |
| | [65] | -0.213924 | 0.459800 | 0.180888 | 0.235400 | -0.256603 | 0.812700 |
| | [66] | -0.210900 | 0.453100 | 0.175270 | 0.234400 | -0.245330 | 0.804700 |
| | [67] | -0.214042 | 0.458100 | 0.179572 | 0.237000 | -0.253803 | 0.810400 |
| | [68] | -0.210600 | 0.453100 | 0.178600 | 0.234400 | -0.252100 | 0.812500 |
| $w_r = 0.875$ | | | | | | | |
| 0.1 | Present | -0.186563 | 0.490607 | 0.147314 | 0.234846 | -0.198547 | 0.801381 |
| 0.2 | Present | -0.116733 | 0.789478 | 0.045753 | 0.175351 | -0.050539 | 0.824649 |
| 0.3 | Present | -0.107539 | 0.797433 | 0.041586 | 0.167759 | -0.045373 | 0.824649 |
| $w_r = 0.8$ | | | | | | | |
| 0.1 | Present | -0.188753 | 0.490607 | 0.149660 | 0.234846 | -0.202205 | 0.801381 |
| 0.2 | Present | -0.160699 | 0.532857 | 0.120203 | 0.230746 | -0.147604 | 0.785471 |
| 0.3 | Present | -0.137966 | 0.574898 | 0.099591 | 0.222600 | -0.111286 | 0.777400 |
| 0.4 | Present | -0.120749 | 0.593448 | 0.088454 | 0.218555 | -0.093618 | 0.773337 |
| 0.5 | Present | -0.107701 | 0.598068 | 0.081641 | 0.218555 | -0.083802 | 0.773337 |
| 0.6 | Present | -0.099129 | 0.598068 | 0.076364 | 0.214529 | -0.076978 | 0.773337 |
| $w_r = 0.7$ | | | | | | | |
| 0.1 | Present | -0.191659 | 0.485911 | 0.152828 | 0.234846 | -0.207302 | 0.801381 |
| 0.2 | Present | -0.165225 | 0.532857 | 0.123908 | 0.230746 | -0.153196 | 0.785471 |
| 0.3 | Present | -0.142547 | 0.574898 | 0.101308 | 0.222600 | -0.112935 | 0.773337 |
| 0.4 | Present | -0.124635 | 0.602681 | 0.088516 | 0.218555 | -0.092300 | 0.773337 |
| 0.5 | Present | -0.110441 | 0.611882 | 0.080997 | 0.214529 | -0.081339 | 0.773337 |
| 0.6 | Present | -0.099314 | 0.611882 | 0.075704 | 0.214529 | -0.074158 | 0.773337 |
| 0.7 | Present | -0.090564 | 0.607286 | 0.071477 | 0.210522 | -0.068596 | 0.773337 |
| 0.8 | Present | -0.083503 | 0.602681 | 0.067872 | 0.210522 | -0.063928 | 0.769254 |

Moreover, effect of the increasing Weissenberg number on the hydrodynamic behavior of the flow is investigated with streamline and vorticity contours that are shown in Figures 5.34 and 5.35, respectively. Streamline plots of Figure 5.34 show that at high We primary vortex center moves in the upstream direction and streamlines near the downstream corners more

curved. Similar effects are observed for creeping flow. However results become quite different in the case of $w_r = 0.875$ (see Figure 5.34 top). After $We=0.2$, USE and DSE secondary eddies disappear and almost no circulation occurs in the cavity (see Table 5.6). Locations of the primary vortex center as a function of Weissenberg number and polymer viscosity w_r are presented in Figure 5.36. Table 5.6 includes the intensities of the primary eddy with the various values of Weissenberg numbers. Their comparison with the literature is also given for Newtonian fluid. Results of the $Re = 100$ indicate that attainable maximum Weissenberg number strongly depends on Reynolds number. At this Reynolds number, at $w_r = 0.875$, 0.8 and 0.7 , maximum We values reached were 0.3 , 0.6 , 0.8 respectively.

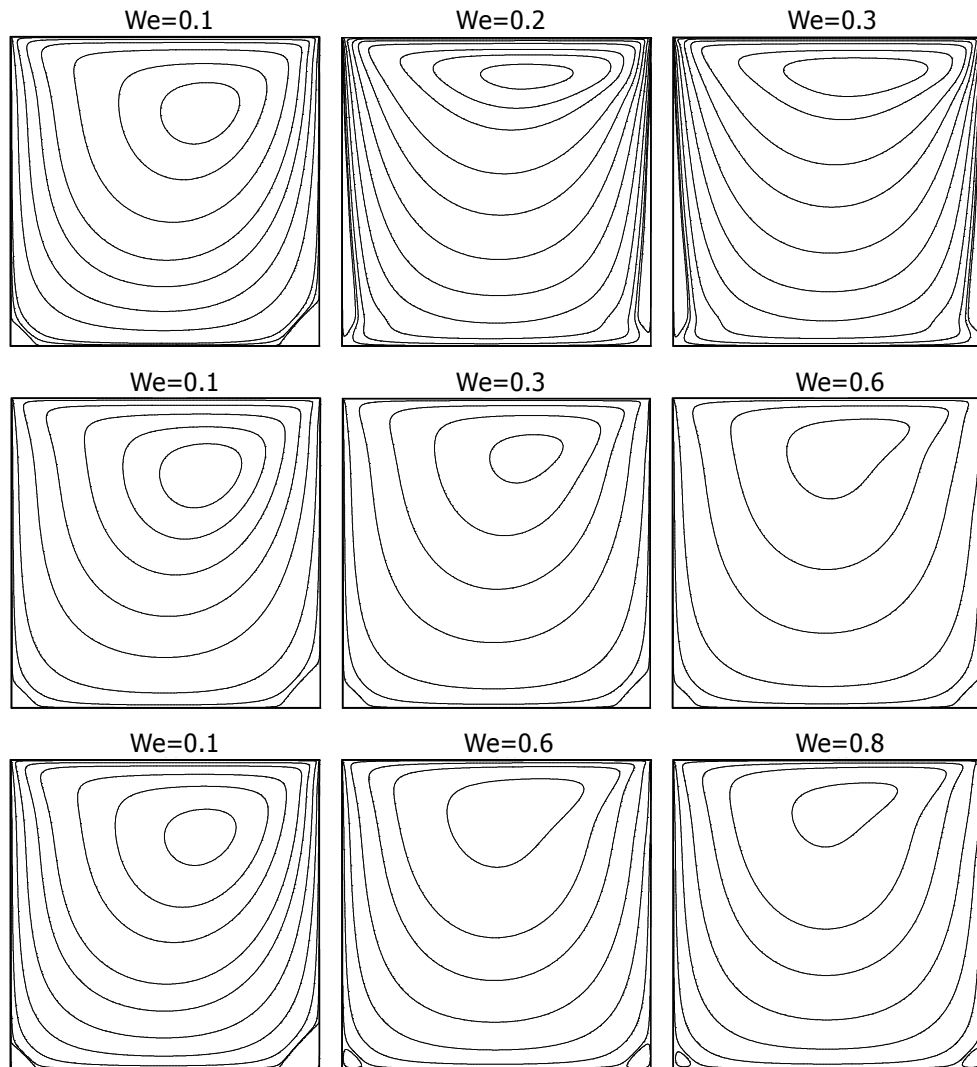
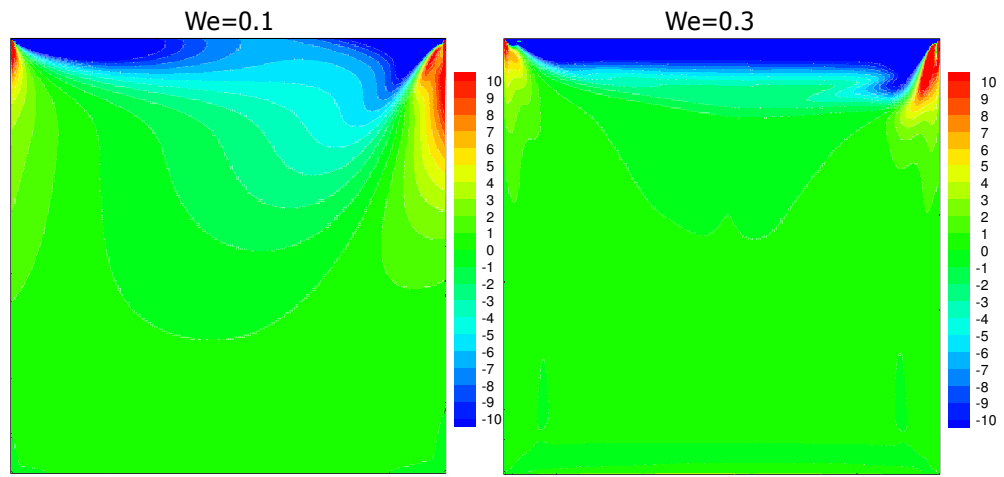
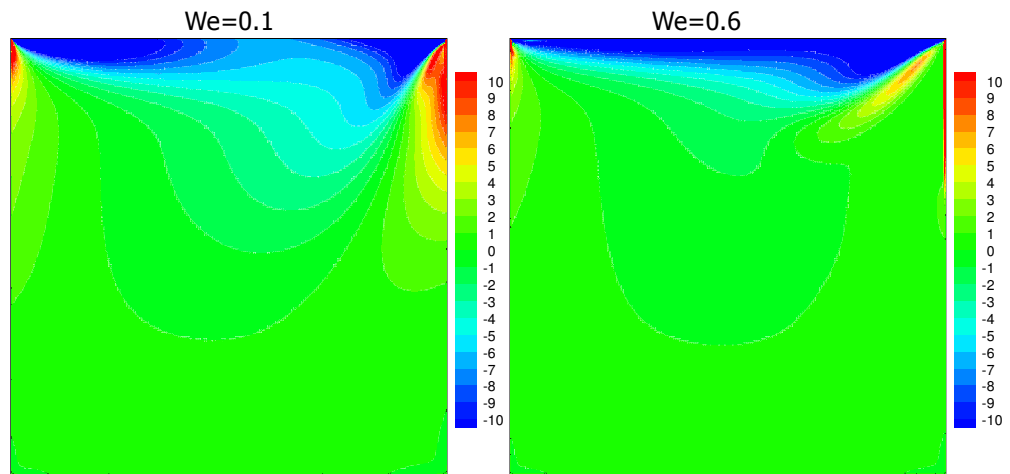


Figure 5.34. The stream functions at top $w_r = 0.875$, middle $w_r = 0.8$, bottom $w_r = 0.7$, for different We and for $Re=100$.

Figure 5.37 shows that downstream (DSE) and upstream (USE) secondary eddy at various We and at $w_r = 0.8$ and $w_r = 0.7$. It is observed that the DSE and USE shrink with increasing We for both polymer viscosities. However, it can clearly be seen that as elasticity is increased, the width and height of the DSE decreases more than USE. These may be due to the unrelaxed stresses. When stretched stresses arrive at the downstream bottom corner, they may still be unrelaxed and may need more distance to be relaxed.

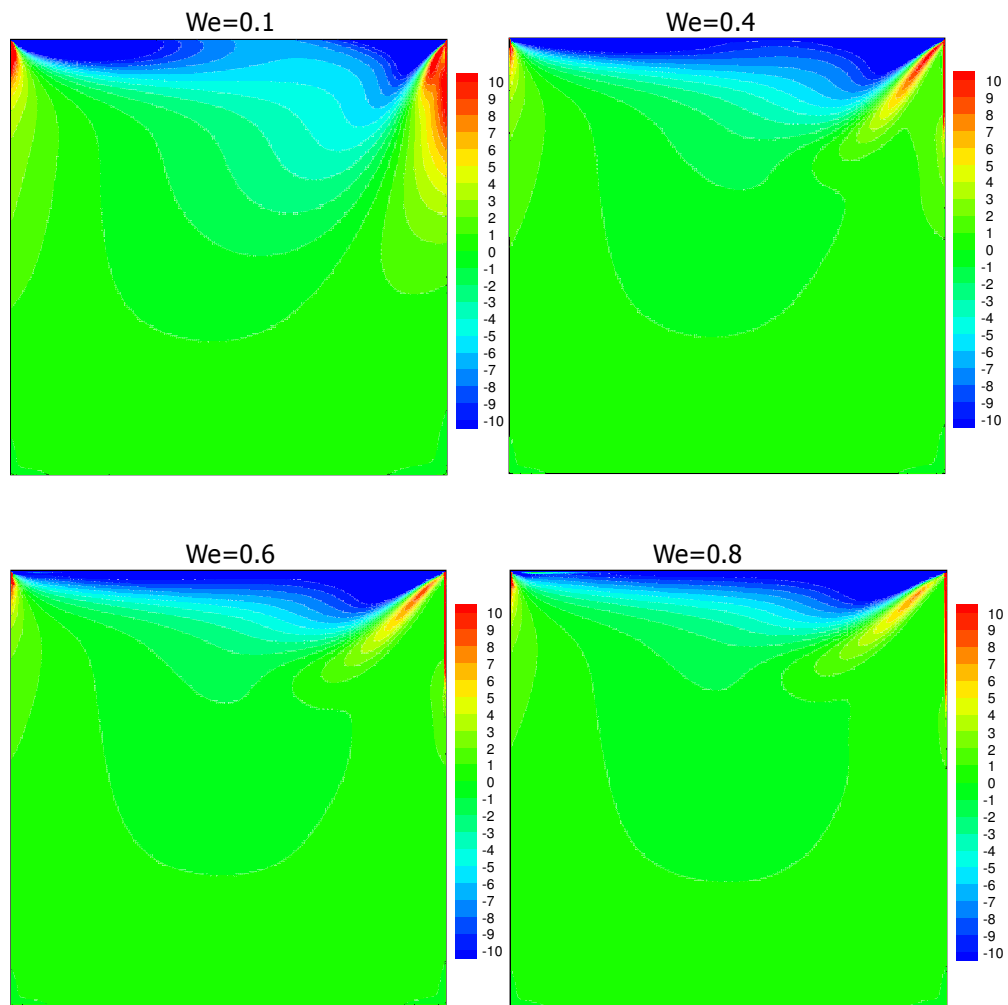


(a)



(b)

Figure 5.35. The vorticity contour a) $w_r = 0.875$, b) $w_r = 0.8$, c) $w_r = 0.7$, for different We and at $Re=100$. Contour levels are shown from -10 to 10 with increment of 1 .



(c)

Figure 5.35. The vorticity contour a) $wr = 0.875$, b) $wr = 0.8$, c) $wr = 0.7$, for different We and at $Re=100$. Contour levels are shown from -10 to 10 with increment of 1. (continued)

Table 5.6. Intensities of the primary eddies as a function of Weissenberg number at Re=100.

| We | Reference | ψ_{\min} | X_{\min} | Y_{\min} |
|---------------|-----------|---------------|------------|------------|
| 0 | Present | -0.10341067 | 0.61553348 | 0.73744621 |
| | [65] | -0.10347100 | 0.61890000 | 0.74000000 |
| | [66] | -0.10342300 | 0.61720000 | 0.73440000 |
| | [67] | -0.10260000 | 0.61720000 | 0.73440000 |
| $w_r = 0.875$ | | | | |
| 0.1 | Present | 0.09429142 | 0.62104905 | 0.76103499 |
| 0.2 | Present | -0.04741423 | 0.58418619 | 0.87600341 |
| 0.3 | Present | -0.04282108 | 0.56558728 | 0.87950867 |
| $w_r = 0.8$ | | | | |
| 0.1 | Present | -0.09507428 | 0.62104905 | 0.76103499 |
| 0.2 | Present | -0.08312456 | 0.61647003 | 0.78947776 |
| 0.3 | Present | -0.07229769 | 0.60268082 | 0.81697465 |
| 0.4 | Present | -0.06429992 | 0.58882050 | 0.83600592 |
| 0.5 | Present | -0.05837442 | 0.57489837 | 0.84347184 |
| 0.6 | Present | -0.05420375 | 0.56558728 | 0.84717292 |
| $w_r = 0.7$ | | | | |
| 0.1 | Present | -0.09611734 | 0.62104905 | 0.75689818 |
| 0.2 | Present | -0.08488373 | 0.61647003 | 0.78547102 |
| 0.3 | Present | -0.07391579 | 0.60728558 | 0.81310660 |
| 0.4 | Present | -0.06547667 | 0.59344793 | 0.83224130 |
| 0.5 | Present | -0.05916544 | 0.57954536 | 0.83974947 |
| 0.6 | Present | -0.05426943 | 0.57024555 | 0.84717292 |
| 0.7 | Present | -0.05033084 | 0.56092390 | 0.85085261 |
| 0.8 | Present | -0.04706214 | 0.55625578 | 0.85451080 |

Normal stress, τ_{xx} , profiles at different values of Weissenberg number and polymer viscosity are presented near the downstream upper corner as a function of y in Figure 5.38. Stress peaks at Reynolds number 100 show similar trends to the creeping flow results.

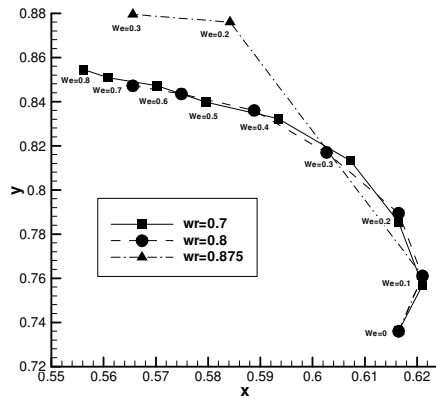


Figure 5.36. Primary vortex center location as a function of We and w_r at $Re=100$.

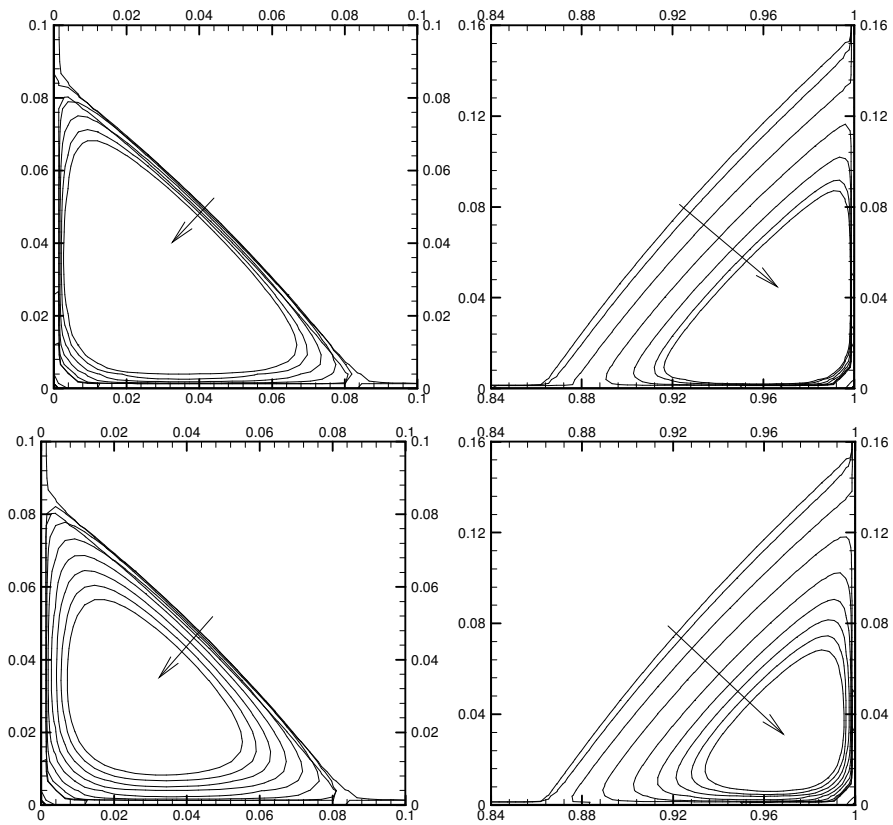


Figure 5.37. Comparison of the eddy sizes USE and DSE as a function of We in terms of contour level at top $w_r = 0.8$, bottom $w_r = 0.7$ for $Re=100$.

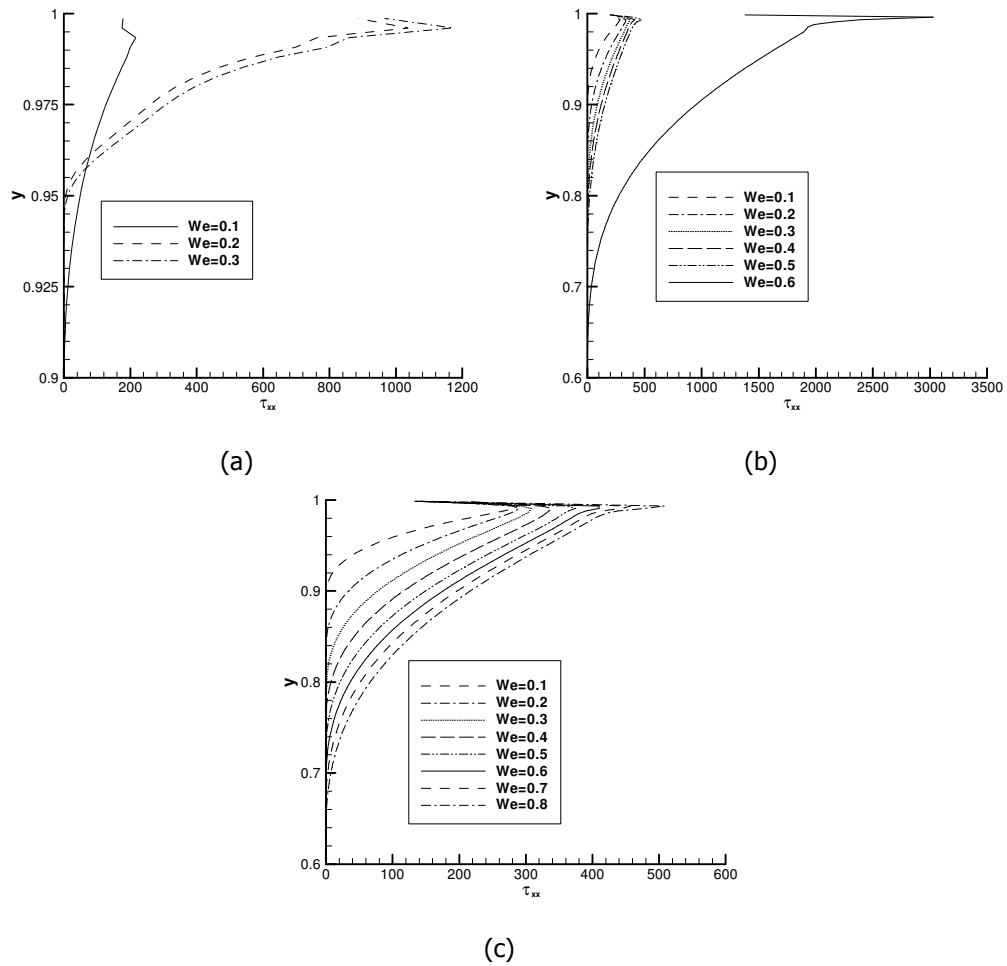


Figure 5.38. Normal stresses, τ_{xx} , near the downstream ($x = 0.9987$) (a) $w_r = 0.875$ (b) $w_r = 0.8$ (c) $w_r = 0.7$ for different We at $Re = 100$.

5.3.4. Results at $Re=400$

In the final test flow at $Re = 400$ is investigated. At this Reynolds number the maximum attainable Weissenberg number at which a converged numerical solution was found 0.1, 0.3 and 0.5 for $w_r = 0.875$, 0.8 and 0.7, respectively. Figures 5.39 and 5.40 illustrate distribution of horizontal velocity along the vertical centerline and vertical velocity along the horizontal centerline. Their extrema values are listed in Table 5.7. In the Figures 5.39 and 5.40 especially for low polymer viscosity cases, as Weissenberg number increases the minimum value of the horizontal velocity component decrease in magnitude and its location moves

closer to the lid. Vertical velocity, on the other hand is almost zero. Computed streamlines and vorticity contours are displayed in Figures 5.41 and 5.42, respectively. At $We = 0.3$, two loops appear in the cavity for both polymer viscosity values. However, after $We = 0.3$ second loop in the cavity disappears and DSE and USE begin to shrink with increasing We for $w_r = 0.7$. Figure 5.43 shows location of the primary vortex center as a function of Weissenberg number at two different w_r . It is found that primary vortex shifts in downstream direction, which is an opposite trend observed in $Re = 0$ and 100 simulations. Table 5.8 includes the intensities of the primary eddy with the various values of We . Their comparison with the literature is also given for Newtonian fluid. In Figure 5.44, we demonstrate the graphs of stress τ_{xx} near the downstream upper corner.

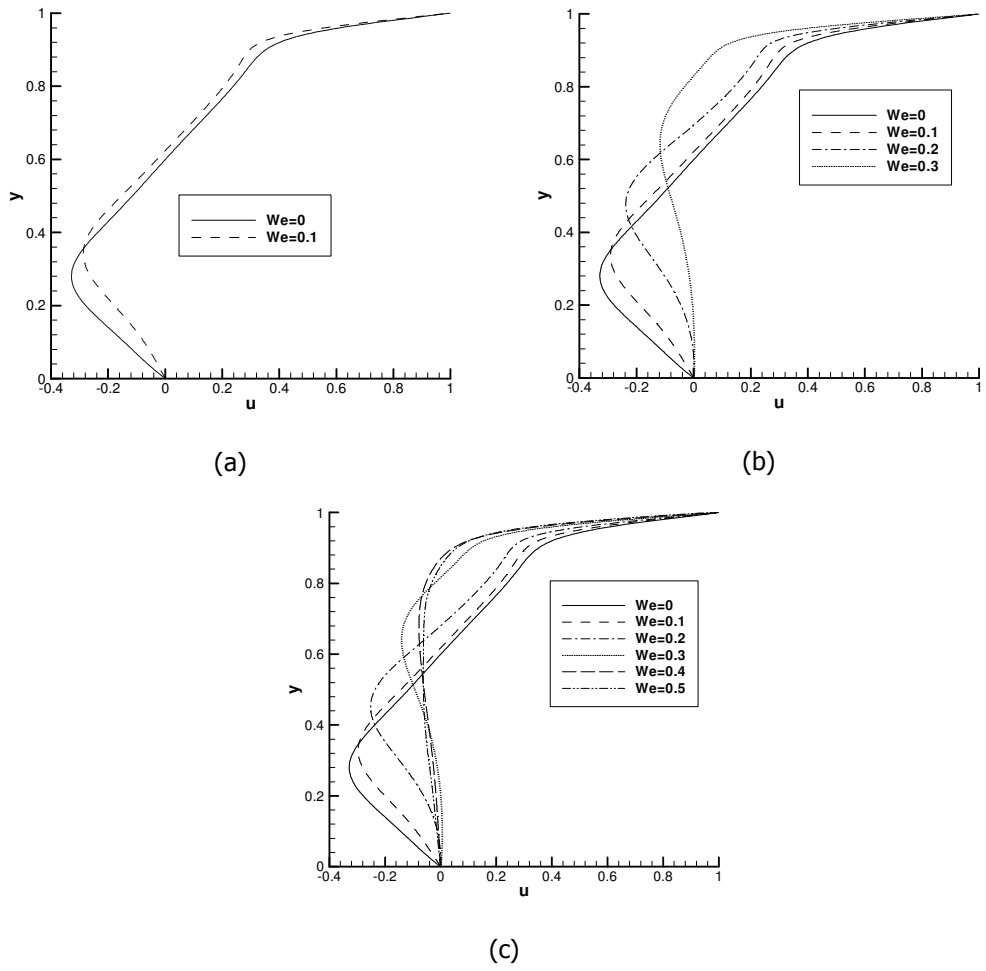
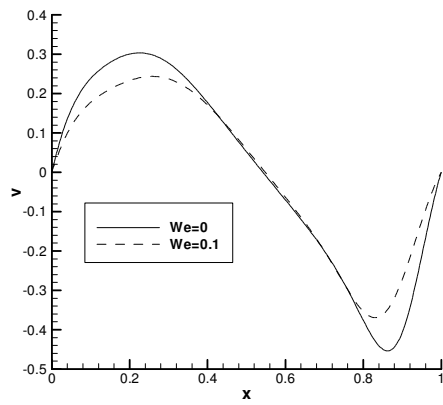
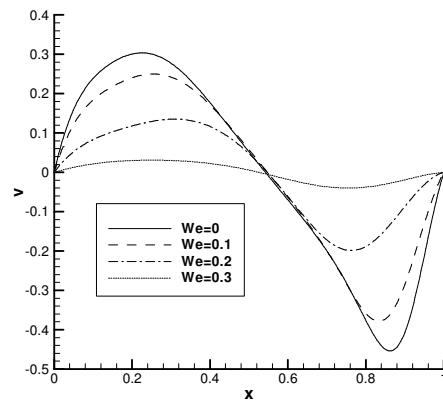


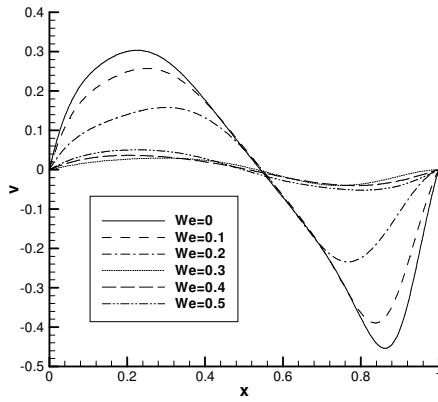
Figure 5.39. Effects of We on u at vertical centerline ($x = 0.5$) for (a) $w_r = 0.875$ (b) $w_r = 0.8$ (c) $w_r = 0.7$ for $Re = 400$



(a)



(b)



(c)

Figure 5.40. Effects of We on v at horizontal centerline ($y=0.5$) for (a) $w_r = 0.875$ (b) $w_r=0.8$ (c) $w_r = 0.7$ for $Re=400$

Table 5.7. Horizontal minimum velocity, vertical minimum and maximum velocity through the centerlines of the cavity at Re=400.

| We | Reference | u_{\min} | y_{\min} | V_{\max} | x_{\max} | V_{\min} | x_{\min} |
|---------------|-----------|------------|------------|------------|------------|------------|------------|
| 0 | Present | -0.327159 | 0.281107 | 0.301868 | 0.226663 | -0.449446 | 0.861762 |
| | [65] | 0.328375 | 0.281500 | 0.304447 | 0.225300 | -0.456316 | 0.862100 |
| | [66] | -0.327260 | 0.281300 | 0.302030 | 0.226600 | -0.449930 | 0.859400 |
| $w_r = 0.875$ | | | | | | | |
| 0.1 | Present | -0.285669 | 0.342679 | 0.241659 | 0.259825 | -0.364606 | 0.828456 |
| $w_r = 0.8$ | | | | | | | |
| 0.1 | Present | -0.289831 | 0.333723 | 0.247890 | 0.255618 | -0.373670 | 0.333723 |
| 0.2 | Present | -0.235405 | 0.476524 | 0.132482 | 0.307161 | -0.193572 | 0.761035 |
| 0.3 | Present | -0.117764 | 0.639269 | 0.029975 | 0.247256 | -0.038502 | 0.752744 |
| $w_r = 0.7$ | | | | | | | |
| 0.1 | Present | -0.295010 | 0.329263 | 0.255583 | 0.251429 | -0.384803 | 0.836006 |
| 0.2 | Present | -0.249793 | 0.448417 | 0.155438 | 0.298417 | -0.228557 | 0.765154 |
| 0.3 | Present | -0.139979 | 0.639269 | 0.028305 | 0.289731 | -0.038294 | 0.744382 |
| 0.4 | Present | -0.077242 | 0.675184 | 0.035751 | 0.206535 | -0.039309 | 0.785471 |
| 0.5 | Present | -0.062104 | 0.537543 | 0.049668 | 0.226663 | -0.051088 | 0.801381 |

Table 5.8. Intensities of the primary eddies as a function of Weissenberg number at $Re = 400$.

| We | Reference | ψ_{\min} | x_{\min} | y_{\min} |
|---------------|-----------|---------------|------------|------------|
| 0 | Present | -0.11391532 | 0.55625578 | 0.60728558 |
| | [65] | -0.11389700 | 0.55360000 | 0.60750000 |
| | [66] | -0.11390900 | 0.55470000 | 0.60550000 |
| $w_r = 0.875$ | | | | |
| 0.1 | Present | -0.10009768 | 0.56558728 | 0.63017903 |
| $w_r = 0.8$ | | | | |
| 0.1 | Present | -0.10145504 | 0.56558728 | 0.63017903 |
| 0.2 | Present | -0.08103418 | 0.59806816 | 0.70158321 |
| 0.3 | Present | -0.05645073 | 0.71889305 | 0.83600592 |
| $w_r = 0.7$ | | | | |
| 0.1 | Present | -0.10316055 | 0.56092390 | 0.62561883 |
| 0.2 | Present | -0.08494495 | 0.58418619 | 0.68844592 |
| 0.3 | Present | -0.05982333 | 0.70158321 | 0.82082228 |
| 0.4 | Present | -0.04583972 | 0.75274358 | 0.88645269 |
| 0.5 | Present | -0.04301233 | 0.73595167 | 0.89670163 |

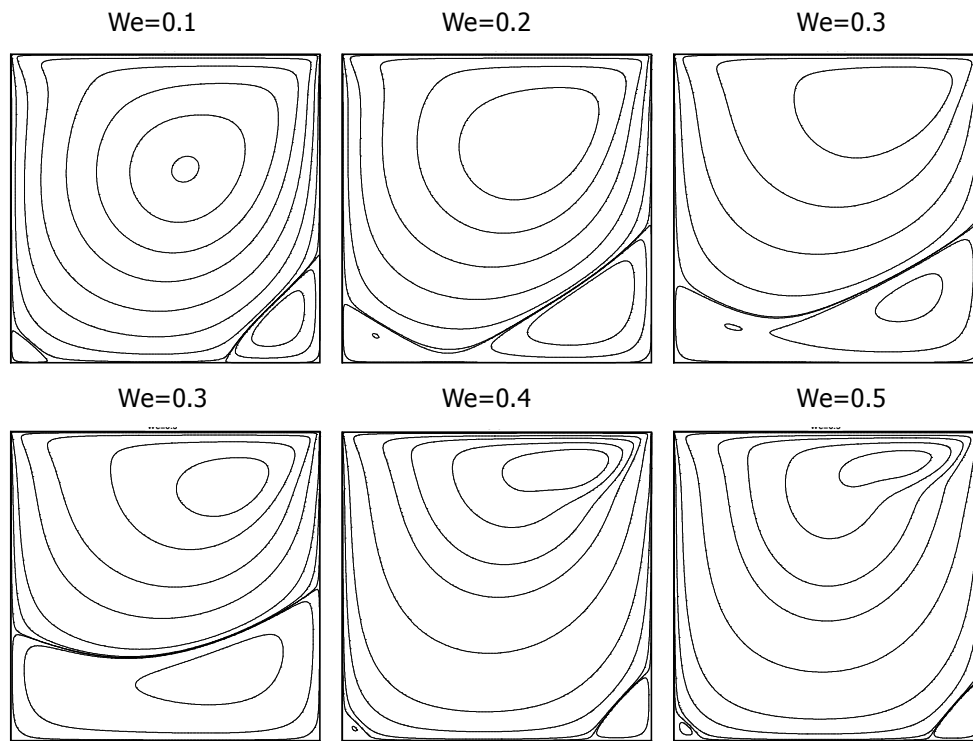
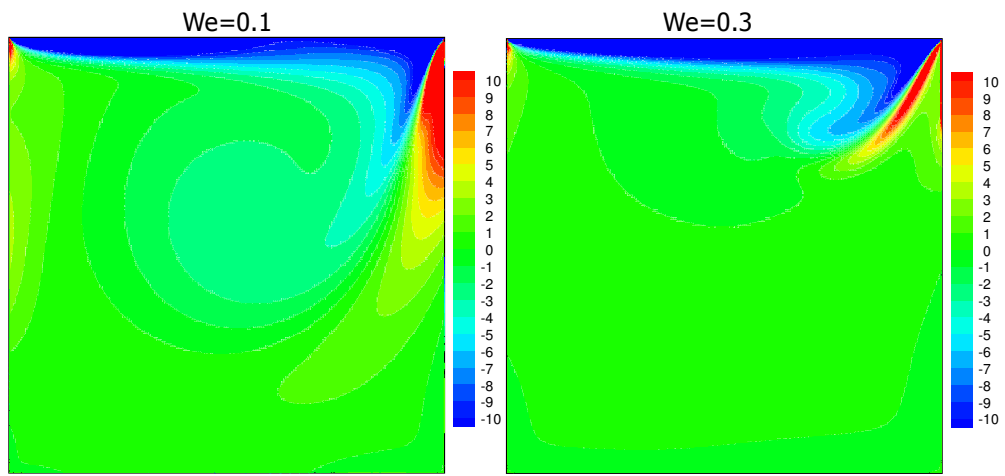
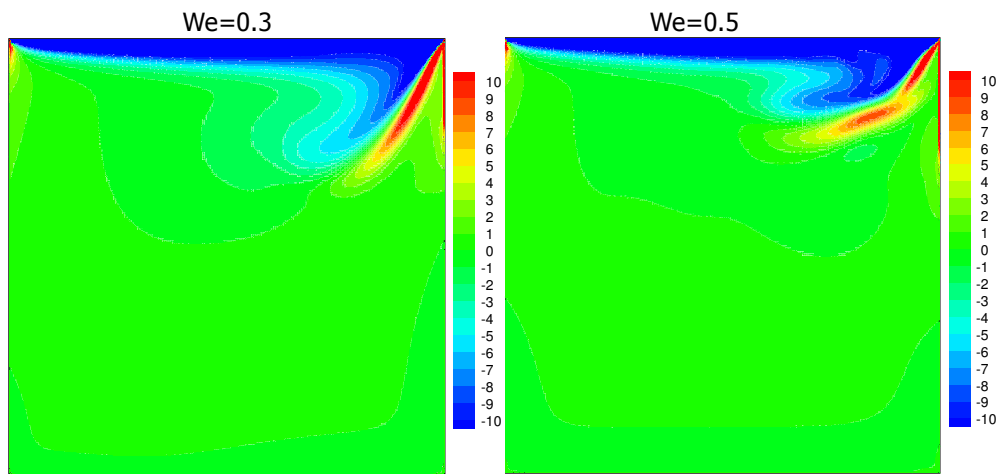


Figure 5.41. The stream functions at top $w_r = 0.8$, bottom $w_r = 0.7$, for different We and for $Re = 400$.



(a)



(b)

Figure 5.42. The vorticity contour a) $w_r = 0.8$, b) $w_r = 0.7$, for different We and at $Re=400$. Contour levels are shown from -10 to 10 with increment of 1.

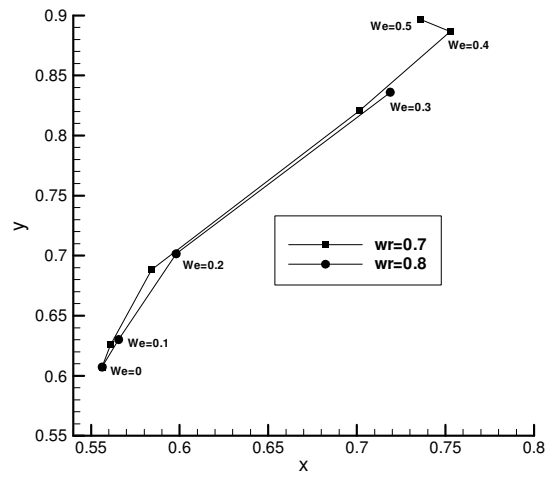
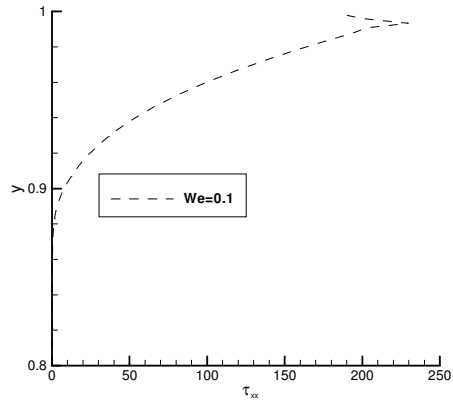
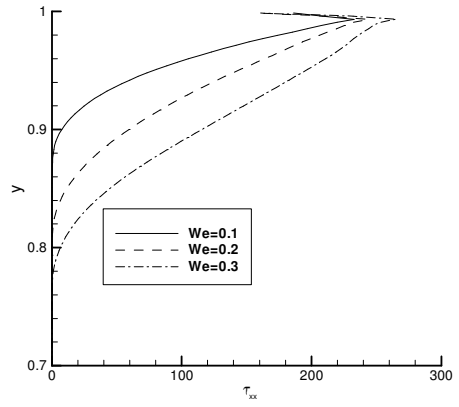


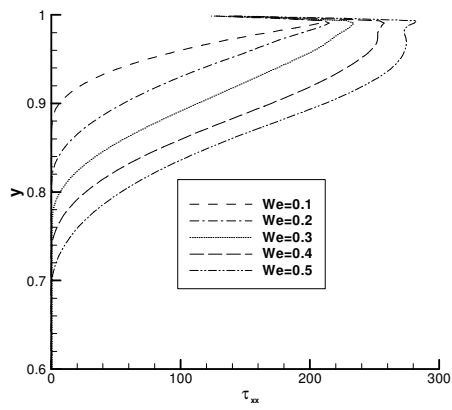
Figure 5.43. Primary vortex center location as a function of We and w_r at $Re=400$.



(a)



(b)



(c)

Figure 5.44. Normal stresses, τ_{xx} , near the downstream ($x = 0.9987$) (a) $wr = 0.875$ (b) $wr = 0.8$ (c) $wr = 0.7$ for different We for $Re = 400$.

CHAPTER 6

PARTICLE MIGRATION AND SUSPENSION STRUCTURE IN STEADY AND OSCILLATORY CHANNEL FLOW

In this chapter, rates of particle migrations for concentrated suspensions of spherical, non-Brownian particles in steady and oscillatory pressure driven channel flow is presented in detail. The equations governing relation between structure and stress in hard sphere suspensions has been developed by Stickel [77] at Department of Chemical Engineering and Material Science University of California at Davis.

6.1. INTRODUCTION

Concentrated suspensions of Brownian, neutrally buoyant hard spheres exhibit rheologically interesting features that are, in many cases, not as well understood as comparable phenomena in polymeric liquids. Even in the absence of any elastic response in the suspending medium, structural rearrangements that follow changes in flow conditions contribute a time-dependent rheological response in step-strain and small amplitude oscillatory shear (SAOS) experiments [78,79,80,81]. In addition, normal stress differences have been measured in viscometric flows [82] and computed in particle-level dynamic simulations [83].

Among the interesting observations involving concentrated suspensions is the observation that particles migrate irreversibly in non-homogeneous shear flows of concentrated suspensions. Dating to the pioneering work of Gadala-Maria and Acrivos [78] and Leighton and Acrivos [84], this finding was at first surprising because it appeared to contradict the well-known principle of reversibility of low Reynolds number flow. However, the presence of non-hydrodynamic interactions, as well as the non-linear nature of the equations that govern the trajectories of particles affected by multiparticle interactions, provides suitable explanations for the irreversible behavior. There is no longer doubt as to existence of phenomenon. It has been observed directly in flows between concentric cylinders [85], pressure driven flow between flat plates [86, 87] and in cylindrical tubes [88] as well as in models of process equipment such as scraped surface heat exchangers and extruders [89].

A number of modeling approaches have been proposed to predict particle migration in concentrated suspensions, and its relation to velocity and stress fields. Leighton and Acrivos [84] proposed expressions for the scaling of particle flux with concentration, shear rate and particle dimension. The scaling arguments were used in a slightly modified form by Phillips et al [85] to form a two part, phenomenological model consisting of particle conservation equation and generalized Newtonian fluid expression for the stress. Although successful in describing the time-dependent development of concentration variations in flow between concentric cylinders, the resulting model is not based directly on fundamental principles that may be readily generalized to mixed or non-viscometric flows. In addition, it fails to explain qualitative features of concentration profiles that have been measured subsequently [88]. Not and Brady [90] proposed a model that is based on a principle of energy conservation. By analogy with granular flows, they introduced the concept of "suspension temperature" to describe the fluctuations in particle velocities in highly filled suspensions. Such a suspension temperature has since been measured [91].

Of primary interest in this work is the approach proposed by Morris and Boulay [92] and Miller and Morris [93], who solved that momentum conservation in a two-phase fluid can lead to migration of one phase relative to other. To be applied, the theory of Morris and Boulay [92] requires detailed understanding of relation between the stress, structure and deformation in particulate suspensions. Among the possible approaches to describing, these complicated relationships are, at the continuum level, the models of Phan-Thien [94], Goddard [95], and Stickel et al. [96, 97]. Particle level theories have been developed by Brady and co-workers [98, 99]. In the model of Stickel et al. [96, 97] (hereafter referred to as SPP model), the term structure refers to a second-order tensor that is calculated based on the shape formed by the cage of nearest neighbors surrounding any test particle in the suspension. The structure and stresses predicted by the model were evaluated independently by comparing with Stokesian dynamics simulations. The SPP model therefore provides a convenient means of reproducing the dominant structural and rheological features that would be computed by particle level simulations, if they were computationally feasible. In addition to comparing with dynamic simulations, direct comparisons have been made between SPP model and experimental results for the time dependent response of non-Brownian, neutrally buoyant suspensions [97]. One surprising experimental observation that has not yet been predicted by any theory describing particle migration is the findings of Butler et al. [88] that in oscillatory tube flow with small but finite strains, in some cases particles migrate to tube wall. This observation is at odds with what is seen in steady flows and in large strain oscillatory flows, for which the particles generally migrate to regions of

low shear rate. Although not predicted theoretically, migration toward regions of high shear rate were found in Stokesian dynamics simulations performed by Morris [100]. Those simulations were performed for a monolayer of mobile spheres suspended between flat walls comprised of other, fixed spheres.

6.2. A MODEL FOR STRUCTURE, STRESS AND FLOW

We present here a set of coupled, frame –indifferent equations that can be solved to obtain the structure, stress and velocity profiles in suspension flowing at low Reynolds number. The theoretical description of particle migration is that of Morris and Boulay [92] and Miller and Morris [93], with the addition of a dispersive flux for steady flows, which have unlimited strain. In that theory, migration across stream lines is shown to be required to conserve momentum in both suspensions as a whole and in the particle phase. The divergence of the particle acts as a body force that drives particle motion relative to the suspension-average velocity, causing an interchange of momentum. To obtain the particle stress we use the SPP model.

6.2.1 The Migration Model

An approach to modeling particle migration that is based on mass and momentum balances has been presented by Morris and Boulay [92] and Miller and Morris [93]. Conservation of mass and momentum in the bulk suspension are described in terms of the suspension average velocity \underline{v} and suspension average stress $\underline{\underline{\Sigma}}$ by

$$\nabla \cdot \underline{v} = 0 \quad (6.1)$$

and

$$\nabla \cdot \underline{\underline{\Pi}} + \langle \rho \rangle \underline{g} = 0 \quad (6.2)$$

where \underline{g} is gravitational acceleration and $\langle \rho \rangle$ is the density of the bulk suspension. The bulk stress $\underline{\underline{\Pi}}$ is related to the particle contribution $\underline{\underline{\Sigma}}^p$ by

$$\underline{\underline{\Pi}} = -p\underline{I} + 2\eta_0 \dot{\underline{\underline{\gamma}}} + \underline{\underline{\Sigma}}^p \quad (6.3)$$

where η_0 is the viscosity of suspending liquid. In general the particle stress $\underline{\underline{\Sigma}}^p$ contains an isotropic portion that constitutes a particle contribution to the overall pressure, beyond the fluid-phase average pressure p . A momentum balance over the particle phase requires that

$$0 = \nabla \cdot \underline{\underline{\Sigma}}^p + n \langle \underline{F}^H \rangle + \phi \Delta \rho \underline{g} \quad (6.4)$$

where the number of density n is related to the volume fraction ϕ by

$$\phi = \left(\frac{4\pi a^3}{3} \right) n \quad (6.5)$$

The average hydrodynamic force $\langle \underline{F}^H \rangle$ is the mean force on the particles that is caused by their migration relative to the suspension average velocity. If the divergence of the particle stress is non-zero, then this hydrodynamic force must be non-zero, to affect an exchange of momentum between the two phases in the suspension. In the absence of inertia $\langle \underline{F}^H \rangle$ depends linearly on that migration velocity, so that the mean volume flux is

$$(\underline{v}^p - \underline{v}) = - \frac{\phi f_s(\phi)}{6\pi\eta_0 a} \langle \underline{F}^H \rangle \quad (6.6)$$

Here the function $f_s(\phi)$ is a sedimentation hindrance that accounts for the finite volume fraction,

$$f_s(\phi) = (1 - (\phi / \phi_m))(1 - \phi)^{\alpha-1} \quad (6.7)$$

In addition to the flux of particle volume described by equation (6.6), which is required to satisfy momentum conservation, multiparticle interactions that occur whenever a concentrated suspension is subjected directly to the random fluctuations in the particle trajectories relative to the suspension average velocity. It is comparable to the Brownian flux described by Einstein [101], who showed in very simple terms that if a population of particles undergoes random jumps, then in the presence of a concentration gradient a flux results that is proportional to $\nabla \phi$. In a following, concentrated suspensions, the jumps relative to the average motion are caused by particle interactions. In the axial direction they lead to a measurable Taylor dispersion effect [102], but in the current work it is dispersion in the velocity gradient direction that is of interest. This dispersion coefficient $D_{dis}(\phi)$ has been measured experimentally and the results are commonly report in the form

$$D_{dis}(\phi) = \dot{\gamma} a^2 d(\phi) \quad (6.8)$$

where $d(\phi)$ is a dimensionless function of volume fraction. In our computations we use

$$d(\phi) = 0.1001e^{-[(\phi-0.5287)/0.313]^2} \quad (6.9)$$

a correlation that we chose as a convenient and smooth way to represent experimental data from the literature. A plot of equation (6.9) and experimental data from literature is shown in Figure 6.1. For the non-Brownian particles of interest here, the full contribution of this dispersion terms is only present when the deformation is sufficient for multiple particle interactions to cause a loss of reversibility. Conservation of particles requires that

$$\frac{\partial \phi}{\partial t} + \underline{v} \cdot \nabla \phi = -\nabla \cdot \underline{j} \quad (6.10)$$

where \underline{j} is the volume flux of particles relative to the suspension average velocity \underline{v} . For the flux \underline{j} we have both convective and dispersive contributions,

$$\underline{j} = -D_{dis}(\phi) \nabla \phi - \frac{\phi_s^c(\phi)}{6\pi\eta_0 a} \langle \underline{F}^H \rangle \quad (6.11)$$

From equation (6.4) for neutrally buoyant particles with $\Delta\rho = 0$

$$\langle \underline{F}^H \rangle = -\frac{1}{n} \nabla \cdot \underline{\underline{\Sigma}}^p \quad (6.12)$$

Substitution of equations (6.11) and (6.12) in to equation (6.10) yields the desired conservation equation for particles. In that equation, particles are driven to migrate across streamlines by body force proportional to the divergence of the particle stress, and also by hydrodynamic dispersion.

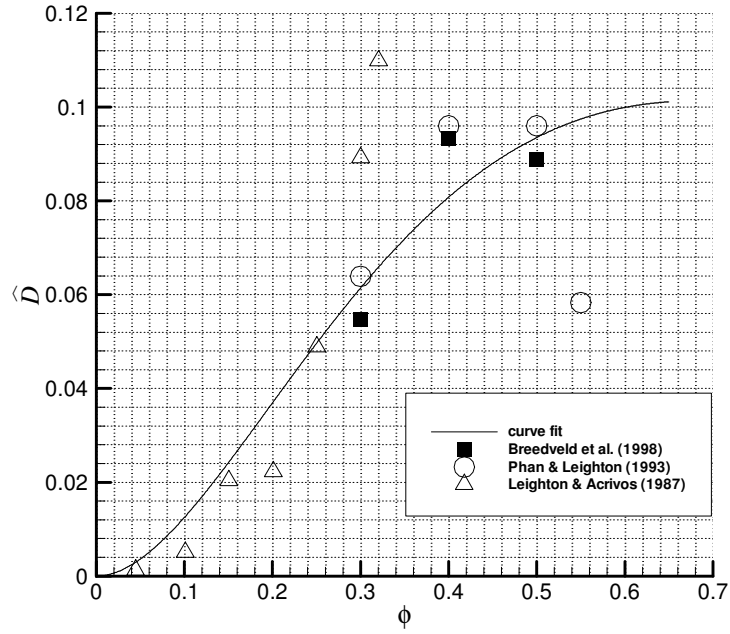


Figure 6.1. Profiles of dimensionless diffusion coefficient curve fit obtained from experimental data.

6.2.2 The SPP Model

In the SPP model, structure is defined mathematically in terms of the average distance $l_{mf}(\hat{x})$ that a test particle can move in a direction denoted by the unit vector \hat{x} before colliding with another particle. The isotropic part of second order structure tensor \underline{Y} is given by ζ_s , where

$$\zeta_s = \frac{1}{3} \text{tr}(\underline{Y}) \quad (6.13)$$

To obtain an evolution equation for the structure, it is presumed that, in a reference frame rotating with the local fluid vorticity, changes in structure depend in some fashion on the structure itself and the rate of deformation

$$\overset{\circ}{\underline{Y}} = \underline{Y}(\underline{Y}, \dot{\underline{\gamma}}) \quad (6.14)$$

here the superscript o refers to the corotational derivative or time derivative in reference frame rotating with local vorticity, given by

$$\underline{\underline{\dot{Y}}}^o = \frac{\partial}{\partial t} \underline{\underline{Y}} + \underline{\underline{v}} \cdot \nabla \underline{\underline{Y}} \cdot \underline{\underline{w}} + \underline{\underline{w}} \cdot \underline{\underline{Y}} \quad (6.15)$$

the rate of deformation and vorticity tensors $\underline{\underline{\dot{\gamma}}}$ and $\underline{\underline{w}}$ are defined by

$$\underline{\underline{\dot{\gamma}}} = \frac{1}{2} (\nabla \underline{\underline{v}} + \nabla \underline{\underline{v}}^t) \quad (6.16)$$

$$\underline{\underline{w}} = \frac{1}{2} (\nabla \underline{\underline{v}} - \nabla \underline{\underline{v}}^t) \quad (6.17)$$

General forms of the function on the right side of equation (6.14) that satisfy the constraint of frame indifference are well known [104, 105], and form the basis of second order fluid constitutive model. In the SPP model, in the interest of simplicity, terms non-linear in the structure tensor $\underline{\underline{Y}}$ are also neglected.

$$\begin{aligned} \underline{\underline{\dot{Y}}}^o = c_2 \dot{\gamma} \left[\frac{1}{3} \text{tr}(\underline{\underline{Y}}) - 3f(\phi) \right] \underline{\underline{I}} + c_3 \text{tr} \left(\underline{\underline{Y}} \cdot \underline{\underline{\dot{\gamma}}} \right) \underline{\underline{I}} + c_4 \dot{\gamma} \left[\underline{\underline{Y}} - \frac{1}{3} \text{tr}(\underline{\underline{Y}}) \underline{\underline{I}} \right] + \\ \left[c_5 f(\phi) + c_6 \frac{1}{3} \text{tr}(\underline{\underline{Y}}) \right] \underline{\underline{\dot{\gamma}}} + c_7 \left[\underline{\underline{Y}} \cdot \underline{\underline{\dot{\gamma}}} + \underline{\underline{\dot{\gamma}}} \cdot \underline{\underline{Y}} - \frac{2}{3} \text{tr} \left(\underline{\underline{Y}} \cdot \underline{\underline{\dot{\gamma}}} \right) \underline{\underline{I}} \right] \end{aligned} \quad (6.18)$$

All tensors on the right side of equation (6.18) are traceless except those explicitly proportional to the identity tensor $\underline{\underline{I}}$. The values of c_k in equation (6.18) are found by Stickel et al. [96] and here tabulated in Table 6.1.

An equation for the particle stress $\underline{\underline{\Pi}}_p$ can be found in manner comparable to that used for the structure $\underline{\underline{Y}}$.

$$\underline{\underline{\Pi}}_p = \underline{\underline{\Pi}}_p \left(\underline{\underline{Y}}, \underline{\underline{\dot{\gamma}}} \right) \quad (6.19)$$

Stickel et al. [96, 97] proposed the model as

$$\underline{\underline{\Sigma}}_p = \eta_o \left\{ \begin{array}{l} k_2 \left[\frac{1}{3} \text{tr}(\underline{\underline{Y}}) - 3f(\phi) \right] \underline{\underline{I}} + k_3 \text{tr}(\underline{\underline{Y}} \cdot \dot{\underline{\underline{Y}}}) \underline{\underline{I}} + \left[k_5 f(\phi) + k_6 \frac{1}{3} \text{tr}(\underline{\underline{Y}}) \right] \dot{\underline{\underline{Y}}} \\ + k_7 \left[\underline{\underline{Y}} \cdot \dot{\underline{\underline{Y}}} + \dot{\underline{\underline{Y}}} \cdot \underline{\underline{Y}} - \frac{2}{3} \text{tr}(\underline{\underline{Y}} \cdot \dot{\underline{\underline{Y}}}) \underline{\underline{I}} \right] \end{array} \right\} \quad (6.20)$$

The values of k_i in equation (6.20) are given in Table 6.2.

Table 6.1. Values of c_k in equation 6.2.2.6

| c_k | values |
|-------|--------|
| c_1 | 12.2 |
| c_2 | -4.07 |
| c_3 | -23.5 |
| c_4 | -2.41 |
| c_5 | -2.54 |
| c_6 | -0.95 |
| c_7 | 0.47 |

Table 6.2. Values of k_i in equation 6.2.2.8

| k_i | values |
|-------|----------|
| k_1 | 0.41752 |
| k_2 | -0.13917 |
| k_3 | 2.428 |
| k_4 | 0 |
| k_5 | -5.3956 |
| k_6 | -0.51987 |
| k_7 | 1.3525 |

6.3. NUMERICAL SOLUTION

The flow and structural evaluation of particulate suspension must satisfy equations (6.1) and (6.10-12) governing conservation of mass and particles, respectively, and equation (6.12) and (6.14) governing momentum conservation in the bulk suspension and particle phase, respectively. These equations can be solved in an arbitrary flow by using the constitutive model for structure and stress represented by equations (6.18) and (6.20) respectively. These equations take particularly simple form in rectangular channel. We consider a region of the channel far from the entrance and exit, where variations in structure and flow in the flow direction x_1 are negligible in the channel bounded at $x_2 = \pm H$ by solid, flat walls. The pressure gradient $G(t)$ driving the flow varies cosine function in time,

$$G(t) = G_0 \cos(\omega t) \quad (6.21)$$

where the values of the frequency ω are constrained such that

$$\frac{\langle \rho \rangle \omega H^2}{\eta_0} \ll 1 \quad (6.22)$$

Under this constraint, the flow in the channel is free of inertial effects [106]. Although suspension structure responds to changing conditions only after several strain units of deformation, with a given structure the suspension flow responds instantaneously to changes in the pressure gradient. The function $G(t)$ is thus actually a dynamic pressure gradient from which hydrostatic variations are removed according to $G(t) = \nabla p - \rho \underline{g}$.

For fully developed flow, the convective transport term $\underline{v} \cdot \nabla \phi$ in equation (6.10) is negligible, and the equation governing conservation of particles simplifies to

$$\frac{\partial \phi}{\partial t} = - \frac{\partial j}{\partial x_2} \quad (6.23)$$

where

$$j_2 = -D_{dis}(\phi) \frac{\partial \phi}{\partial x_2} + \frac{2a^2}{9\eta_0} f_s(\phi) \frac{\partial \Sigma_{22}^p}{\partial x_2} \quad (6.24)$$

The channel width and amplitude of the pressure gradient G_0 may be used to identify scales for normalizing the variables in equation (6.24). We define a characteristic shear rate according to

$$\dot{\gamma}_0 = \frac{G_0 H}{\eta_0} \quad (6.25)$$

Then the dimensionless shear rate, position and time are given by

$$\hat{\gamma} = \frac{\dot{\gamma}}{\dot{\gamma}_0}, \quad \hat{x}_2 = \frac{x_2}{H}, \quad \hat{t} = \dot{\gamma}_0 t \quad (6.26)$$

The particle stress is made dimensionless by a characteristic stress based on the solvent viscosity,

$$\hat{\underline{\underline{\Sigma}}}^p = \frac{\underline{\underline{\Sigma}}^p}{\dot{\gamma}_0 \eta_0} \quad (6.27)$$

Then in dimensionless form, the particle conservation equation is

$$\frac{\partial \phi}{\partial \hat{t}} = - \left(\frac{a}{H} \right)^2 \frac{\partial}{\partial \hat{x}_2} \left[\frac{2}{9} f_s(\phi) \frac{\partial \hat{\underline{\underline{\Sigma}}}_{22}^p}{\partial \hat{x}_2} - P \hat{\gamma} d(\phi) \frac{\partial \phi}{\partial \hat{x}_2} \right] \quad (6.28)$$

where equation (6.8) has been used to specify the scaling of dispersion coefficient. Here P represent the effect of the hydrodynamic dispersion. If P=1 means fully hydrodynamic dispersion included. The 22 component of the particle contribution to the stress is given

$$\hat{\underline{\underline{\Sigma}}}_{22}^p = \hat{\gamma} \left\{ k_1 f(\phi) + \frac{k_2}{3} tr(\underline{\underline{Y}}) + \frac{2 \hat{\gamma}_{12}}{\hat{\gamma}} \left(k_3 + \frac{k_7}{3} \right) Y_{12} \right\} \quad (6.29)$$

scalar rate of strain is related to the 12 tensor component by

$$\hat{\gamma} = \left[2 \hat{\underline{\underline{\gamma}}} : \hat{\underline{\underline{\gamma}}} \right]^{1/2} = 2 \left| \hat{\gamma}_{12} \right| \quad (6.30)$$

Momentum conservation in the bulk suspension is governed by equation (6.2) with the average density term included in the pressure gradient. The component in the x direction yields,

$$\frac{\partial}{\partial \hat{x}_2} \left(2\hat{\eta}_0 \hat{\gamma}_{12} + \hat{\Sigma}_{21}^p \right) = G_0 \cos(\hat{\omega}t) \quad (6.31)$$

where the total stress has been separated in to the solvent and particle contributions and pressure by using equation (6.3). Equation (6.31) is now integrated, with the requirement that the total shear stress Π_{yx} be zero at the centerline.

$$\hat{\gamma}_{12} + \hat{\Sigma}_{21}^p = \hat{x}_2 G_0 \cos(\hat{\omega}t) \quad (6.32)$$

The yx component of the particle stress tensor may be found from (6.20) and in dimensionless form is given by

$$\hat{\Sigma}_{12}^p = \frac{1}{2} \left\{ k_5 f(\phi) + \frac{k_6}{3} \text{tr}(\underline{Y}) + k_7 (Y_{11} + Y_{22}) \right\} \hat{\gamma}_{12} \quad (6.33)$$

In viscometric flow, the structure tensor \underline{Y} is specified by the 3 diagonal components Y_{11} , Y_{22} and Y_{33} along with the off-diagonal component Y_{12} . The evolution of structure is governed by equation (6.18), the relevant components of which are

$$\begin{aligned} \frac{dY_{11}}{d\hat{t}} &= 2\hat{\gamma}_{12} Y_{12} \left(1 + c_3 + \frac{c_7}{3} \right) + \hat{\gamma} c_1 f(\phi) + \hat{\gamma} c_4 Y_{11} \\ &+ \hat{\gamma} \left(\frac{Y_{11} + Y_{22} + Y_{33}}{3} \right) (c_2 - c_4) \end{aligned} \quad (6.34)$$

$$\begin{aligned} \frac{dY_{22}}{d\hat{t}} &= 2\hat{\gamma}_{12} Y_{12} \left(-1 + c_3 + \frac{c_7}{3} \right) + \hat{\gamma} c_1 f(\phi) + \hat{\gamma} c_4 Y_{22} \\ &+ \hat{\gamma} \left(\frac{Y_{11} + Y_{22} + Y_{33}}{3} \right) (c_2 - c_4) \end{aligned} \quad (6.35)$$

$$\begin{aligned} \frac{dY_{33}}{d\hat{t}} = & 2\hat{\gamma}_{12} Y_{12} \left(c_3 - 2\frac{c_7}{3} \right) + \hat{\gamma}_{c_1} f(\phi) + \hat{\gamma}_{c_4} Y_{33} \\ & + \hat{\gamma} \left(\frac{Y_{11} + Y_{22} + Y_{33}}{3} \right) (c_2 - c_4) \end{aligned} \quad (6.36)$$

$$\begin{aligned} \frac{dY_{12}}{d\hat{t}} = & \hat{\gamma}_{12} (Y_{22} - Y_{11}) + \hat{\gamma}_{c_4} Y_{12} + c_7 \hat{\gamma}_{12} (Y_{22} + Y_{11}) \\ & + \hat{\gamma}_{12} \left(C_5 f(\phi) + c_6 \frac{(Y_{11} + Y_{22} + Y_{33})}{3} \right) \end{aligned} \quad (6.37)$$

Equations (6.28), (6.29), (6.32-37) are 8 equations for the unknown variables $Y_{11}, Y_{22}, Y_{33}, Y_{12}, \hat{\gamma}_{12}, \hat{\Sigma}_{22}^P, \hat{\Sigma}_{12}^P$ and ϕ . Because the fully developed flow, the velocity does not appear explicitly as an unknown, but velocity profiles can be obtained by integrating shear rate. Equations (6.32) and (6.33) can be solved to obtain an explicit relation for the shear rate, which can be substituted directly in to the other equations. The particle stress component can then be substituted in to particle conservation equation (6.28), leaving 5 equations, equation (6.28) and equations (6.34-37), for the 4 unknown components of structure tensor and the volume fraction ϕ . The 5 equations were solved with 3 different approaches. First, under steady conditions, set of nonlinear algebraic equations by solved using optimization toolbox of Matlab[®]. In transient state, both MacCormack and finite volume methods were used to solve the conservation equation, in conjunction with a fourth-order Runge-Kutta method to integrate the structure equations.

6.3.1 The MacCormack Method

The MacCormack method use to solve equation (6.28) consist of predictor and corrector step [107]. To advance from a time step n to $n+1$ the volume fraction at an intermediate point in time $\overline{n+1}$ is calculated according to

$$\overline{\phi}_i^{n+1} = \phi_i^n - \frac{\Delta \hat{t}}{\Delta \hat{x}_2} (j_{i+1}^n - j_i^n) \quad (6.38)$$

This predictor step is followed by a corrector step given by

$$\phi_i^{n+1} = \phi_i^{n+1/2} - \frac{\Delta \hat{t}}{2\Delta \hat{x}_2} \left(\overline{j_i^{n+1}} - \overline{j_{i-1}^{n+1}} \right) \quad (6.39)$$

where the volume fraction at the half-step is given by

$$\phi_i^{n+1/2} = \frac{1}{2} \left(\phi_i^n + \overline{\phi_i^{n+1}} \right) \quad (6.40)$$

To evaluate the flux component in equation (6.38), it is necessary to have structure components at time step n . Starting from special initial condition these were found by integrating equations (6.34-37) by using fourth-order Runge-Kutta method [108]. Derivatives needed to evaluate j^n were evaluated by using central difference formulae, except near boundaries. At the wall at the top of the channel, the second-order backward difference, at the center of the channel second-order forward difference was used [109].

6.3.2 The Finite Volume Method

In order to implement finite volume method, we rearrange the divergence of flux in equation (6.28) to the form

$$\frac{\partial \phi}{\partial \hat{t}} = - \frac{\partial}{\partial \hat{x}_2} \left(\left(\frac{a}{H} \right)^2 d(\phi) \hat{\gamma} \frac{\partial \phi}{\partial \hat{x}_2} \right) + \hat{q} \quad (6.41)$$

where

$$\hat{q} = - \left(\frac{a}{H} \right)^2 \frac{\partial}{\partial \hat{x}} \left[\frac{2}{9} f_s(\phi) \frac{\partial \hat{\Sigma}_{22}}{\partial \hat{y}} - (1 - \alpha) d(\phi) \hat{\gamma} \frac{\partial \phi}{\partial \hat{y}} \right] \quad (6.42)$$

In equation (6.41) and (6.42) are identical to equation (6.28), except that a dispersive flux term always appears explicitly, both when dispersion is present ($\alpha = 1$) and when it is absent ($\alpha = 0$). The scheme for one-dimensional, time-dependent system is shown in Figure 6.2. The superscript i denotes a point in time, with $i = 0$ representing the initial condition. Equation (6.41) is integrated over a time step $\Delta \hat{t}$ and from positions s^i to n^i to obtain equations governing the evaluation field variables at P^i [57]. The result is

$$\phi_P^{i+1} = \phi_P^i - \frac{\Delta t}{\Delta x_2} \left[\left(\frac{d(\phi_n) \hat{\gamma}_n}{\Delta x_2} \right) (\phi_N^i - \phi_P^i) - \left(\frac{d(\phi_s) \hat{\gamma}_s}{\Delta x_2} \right) (\phi_P^i - \phi_S^i) \right] + \hat{q} \Delta t \quad (6.43)$$

Boundary condition at the solid surface is obtained by requiring the particle flux to be zero at the pale n^i located at the wall. This condition is implemented directly in the finite volume approach, via the term \hat{q} in equation (6.41). Note that the dispersive and convective fluxes must also be zero at the wall, because the dispersion coefficient D_{dis} and sedimentation hindrance f_s vanish even in the presence of a finite gradients in particle concentration or stress. Boundary condition at the symmetry line is obtained by requiring strain $\hat{\gamma}_s$ be zero. In addition particle flux to be zero.

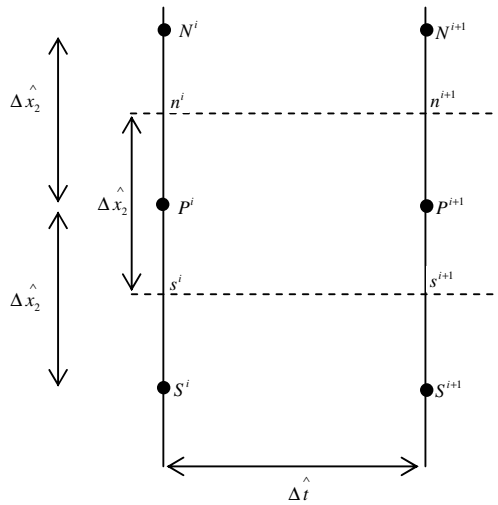


Figure 6.2. 1-D control volume

6.4 RESULTS AND DISCUSSION

Steady state particle concentration profiles were calculated for pressure-driven flow through a rectangular channel, using the model described 6.2.1 and 6.2.2 and numerical methods of Section 6.3. The results are shown as solid curves in Figure 6.3 for are-average volume fractions of $\phi = 0.2$, $\phi = 0.3$, $\phi = 0.4$ and $\phi = 0.5$. Clearly the model predicts a net

migration of particles toward the channel center at all of these average volume fractions. The data points in Figure 6.3 were measured experimentally by Koh et al. [86] and Lyon and Leal [87]. Overall data are in good agreement with the simulations, even though no adjustable parameters were used in performing the calculations. As noted by Lyon and Leal [87], it is possible that results of Koh et al. [86] were measured before steady state had been reached. Lyon and Leal [87] also state that their measurements near the channel wall at $\hat{x}_2/H = 1$ are the least reliable data, providing a possible explanation for the differences there between the simulations and experiments especially at high volume fractions.

Changes in the velocity profile caused by particle migration in pressure driven channel flow are depicted in Figure 6.4 where the velocity v_2 normalized by the centerline value U_{\max} , is plotted versus normalized position x_2/H . The higher concentration at the channel center, the cause the viscosity in that region to be relatively high. In Figures 6.5 is plotted results predicted by the model for change in suspension structure as a result of the steady channel flow, for average volume fractions in the range $0.2 \leq \phi \leq 0.5$. Both isotropic structure function ζ_s and the off-diagonal component Y_{12} vary by several orders of magnitude over the flow domain.

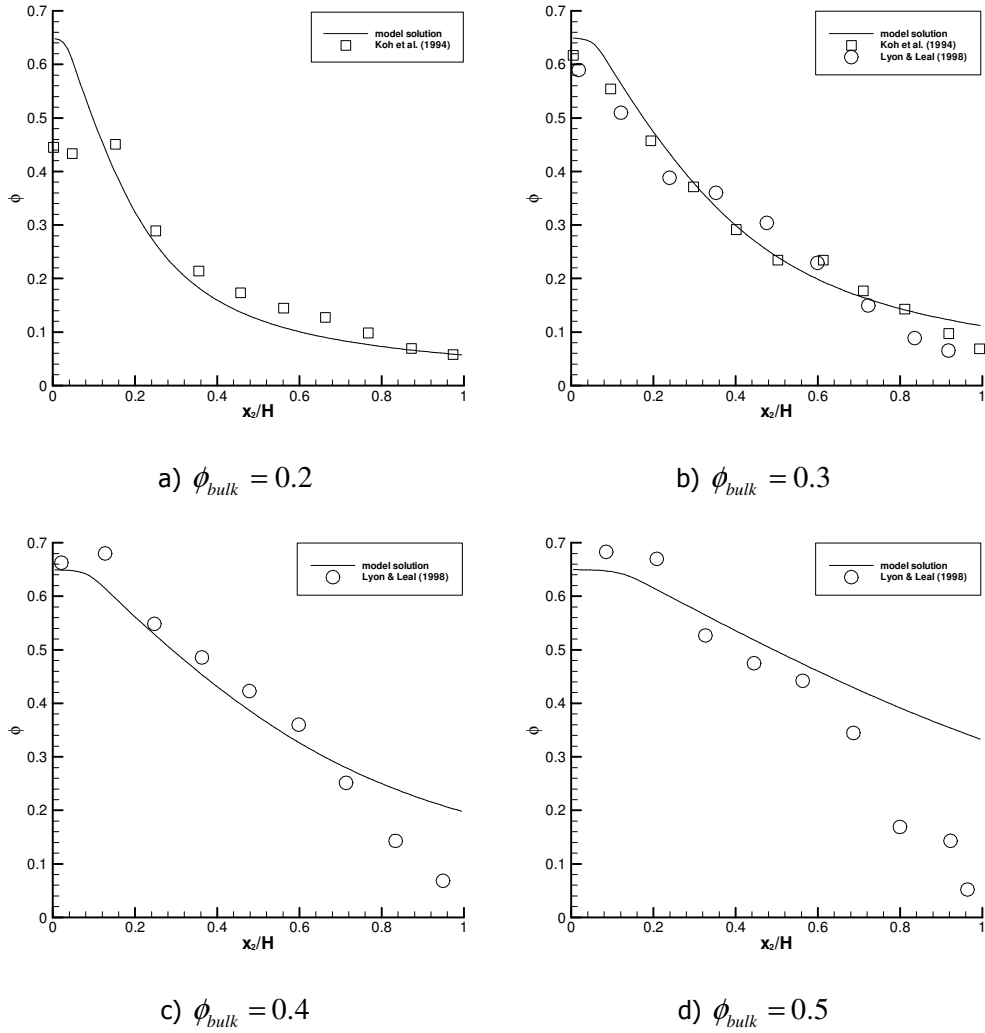


Figure 6.3. Particle volume fraction versus position at steady state. Data are experimentally measurements reported by Koh et al. [86] and Lyon and Leal [87].

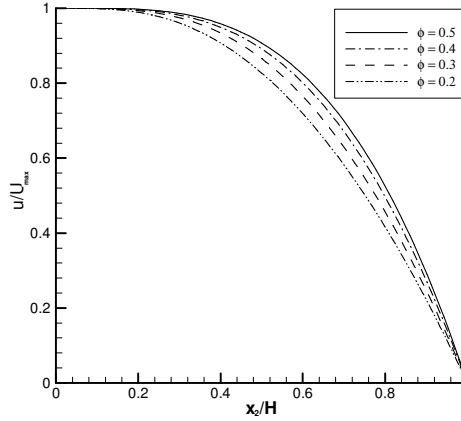
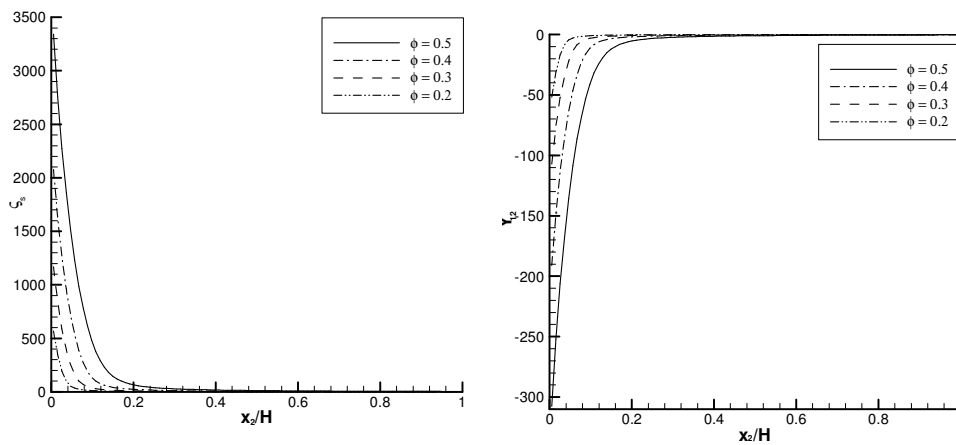


Figure 6.4. Profiles of predicted dimensionless steady velocity are shown for various ϕ .



a) $\zeta_s = \frac{1}{3} tr(\underline{Y})$

b) Y_{12}

Figure 6.5. Profiles of predicted structure component tensors are shown for a)

$\zeta_s = \frac{1}{3} tr(\underline{Y})$ b) Y_{12} at steady state for various ϕ .

In Figures 6.6 is plotted results predicted by the model for change in particle contribution stress and migration flux as a result of the steady channel flow, for average volume fractions in the range $0.2 \leq \phi \leq 0.5$.

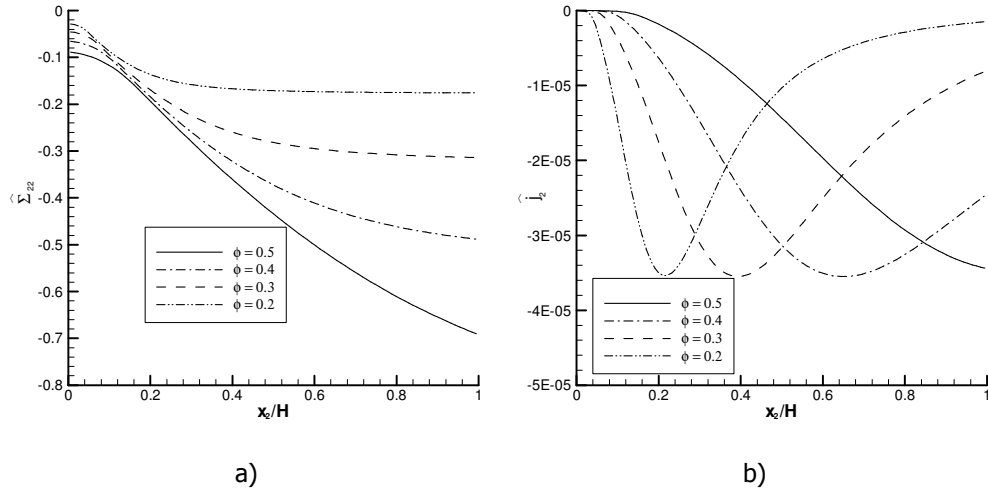


Figure 6.6. Profiles of predicted are shown dimensionless a) particle contributed stress b) migration flux at steady state for various

Also we investigated effect of the initial distribution of the volume fraction on the transient evolution of concentration. Figure 6.7 shows three different initial particle concentrations versus normalized position x_2 / H .

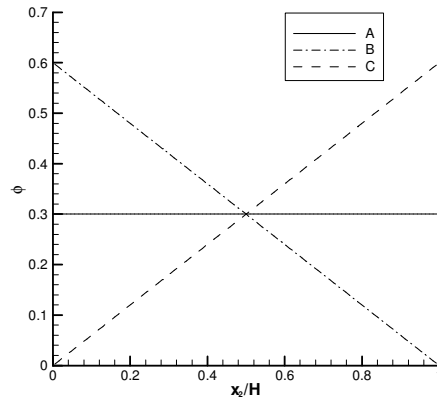


Figure 6.7. Profiles of different initial concentration distributions for $\phi = 0.3$

All initial concentration distributions predict a net migration toward the center, shown in Figure 6.8. We conclude that initial distribution of particle concentrations does not effect steady solution.

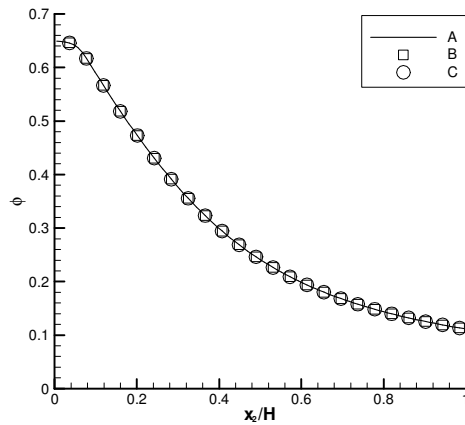


Figure 6.8. Effect of the different initial distribution on steady particle concentration profile for $\phi_{bulk} = 0.3$

An interesting aspect of transient evolution of structure, both near the wall and near the channel center, maybe seen in Figures 6.9 and 6.10 respectively. In Figure 6.9, the isotropic structure function, ζ_s , is plotted for dimensionless time in the range $0 \leq \hat{t} \leq 10$ for suspension in which $\phi = 0.4$ that is homogeneous and isotropic at the initial time. The structure near the wall develops much more quickly than that near the center, because the shear rate there is much larger. Structure in these suspension develops primarily because particles are moved by the imposed flow, and the development of structure occurs as the strain reaches a value of approximately 2-3 [97]. At the higher shear rates, the strain grows more rapidly and hence so does the non-homogeneity in the structure. The long time behavior shown in Figure 6.10 is caused by particle migration.

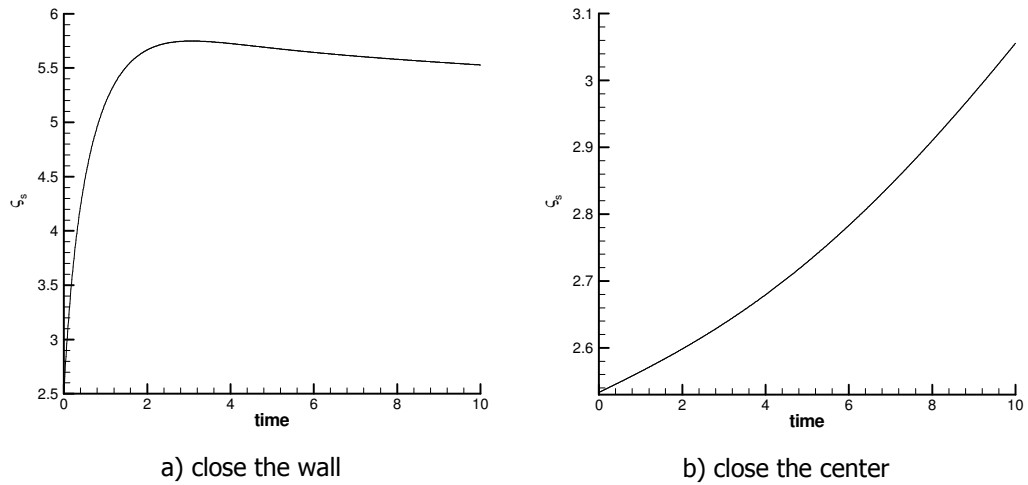


Figure 6.9. Short time trace of structure tensors components profiles a) close to the wall b)close to the center for $\phi = 0.4$.

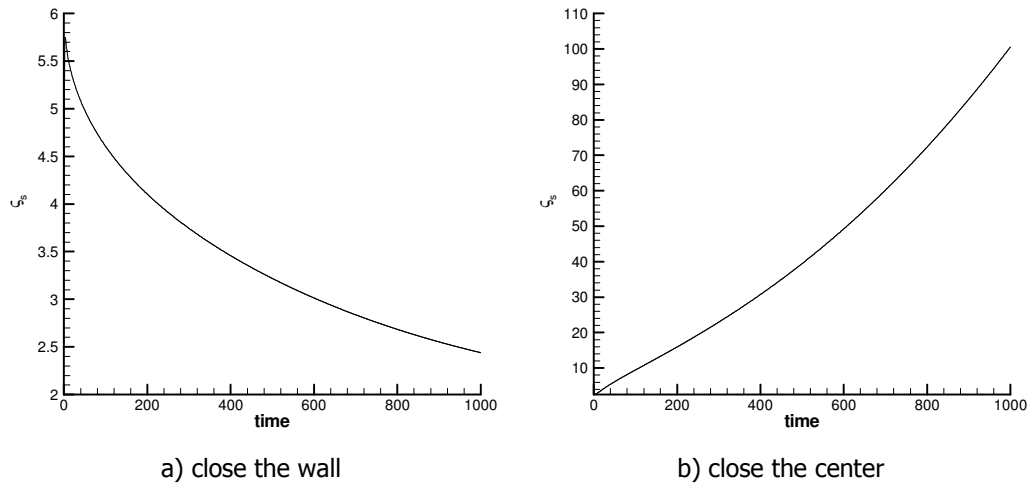


Figure 6.10. Long time trace of structure tensors components profiles a) close to the wall b)close to the center for $\phi = 0.4$.

For the second case, computations are carried out for oscillatory pressure driven channel flow where the pressure gradient followed a cosine function as specified in equation 6.21. Pressure oscillatory results may be described as large strain or small strain by using the characteristic shear rate defined in equation 6.3.5, to gather with the period of the

oscillation $2\pi/\hat{\omega}$. Small values of the dimensionless frequencies $\hat{\omega}$ therefore correspond to large strains and large values of frequencies correspond to small strains. The effect of hydrodynamic dispersion were included in simulations with large strains $\hat{\gamma} \gg 1$, but not for small strains $\hat{\gamma} \ll 1$. Concentration profiles for the low frequencies of $\hat{\omega} = 0.1$ and $\hat{\omega} = 0.5$ or very large displacement are shown in Figure 6.11. The effects of having low frequencies are to decrease the maximum concentration at the channel center. When the maximum strain in the oscillation is small, the concentration profiles are qualitatively different from those in Figure 6.11. Results for frequencies of $\hat{\omega} = 20$, $\hat{\omega} = 30$ and $\hat{\omega} = 50$ for $\phi = 0.4$ are shown in Figure 6.12 after $N=50000$ oscillations have been completed. Near the channel center, there is slight decrease in particle concentration, but greatest change in particle concentration occurs in the region of channel close the wall. The effect of continuing the simulation to $N=150000$ cycles is shown in Figure 6.13. Relative to the concentration profiles in Figure 6.12 after many oscillations the values of the maximum concentrations increase in all 3 cases and the positions of the peaks move toward the channel center. For the results in Figure 6.12 and 6.13 the dimensionless time step was $\Delta \hat{t} = 5 \times 10^{-5}$. Results at higher frequencies are shown in Figure 6.4.12 at $\hat{\omega} = 100$ the results are qualitatively the same as those in Figure 6.4.11. However as the frequency of oscillation increases, a transition occur at $\hat{\omega} = 250$ the position of the maximum concentration is at the wall is shown in Figure 6.15. Three concentration profiles are shown at $\hat{\omega} = 250$ one after 1×10^5 cycles, second after 5×10^5 and the last after 10^6 , the latter showing the higher concentration at the wall. Because the migration occurs only after many cycles and because the time step must be small compares the period of the oscillation, those simulations took several days to complete, for that reason we were not able to study even higher values of $\hat{\omega}$. These results shown at $\hat{\omega} = 250$ were computed dimensionless time steps 9×10^{-6} and 2×10^{-5} and the results differed by 0.5 % or less is shown in Figure 6.16. In general the rate of migration in oscillatory flow depends on the dimensionless frequencies or the amplitude of the strain. However since the migration occurs on a time scale that is long compared to the period of the oscillation at a given frequency the rate of migration scales with $(H/a)^2$ just as in steady flow. Since the particles respond the time-average of the conditions during an oscillation, the concentration changes in Figure 6.13-15 may be

deduced in terms of time-averaged profiles of the particle stress component $\langle \hat{\Sigma}_{22}^P \rangle$, where angle brackets are used to indicate an average over one period of oscillation. The plots of this averaged normal stress component at position in the channel are shown in Figure 6.17 at frequencies of $\hat{\omega} = 50$, $\hat{\omega} = 100$ and $\hat{\omega} = 250$ after $N=10^4$ period of oscillations. At $N=10^4$ very little migration has occurred, but the suspension has experienced ample deformation to have forgotten its initial condition. Particles migrate toward the wall in regions where the slope is positive and toward the center where it is negative. The plots therefore indicate that at lower frequencies 50 and 100 there is a region near the channel center where particles move toward the wall but near the wall they migrate inward toward the center. The concentration maximum is therefore expected to be located near the wall, but at $x_2 < H$. By contrast, at the highest frequency of 250 the slope is positive in the entire domain, and consequently the maximum value of the concentration is expected to be located at $x_2 = H$.

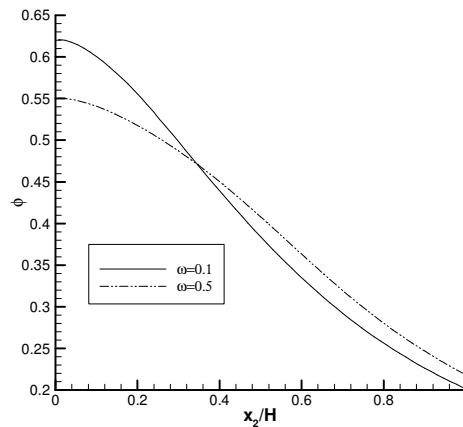


Figure. 6.11. Concentration profiles after $N=1000$ cycles, with full hydrodynamic dispersion included.

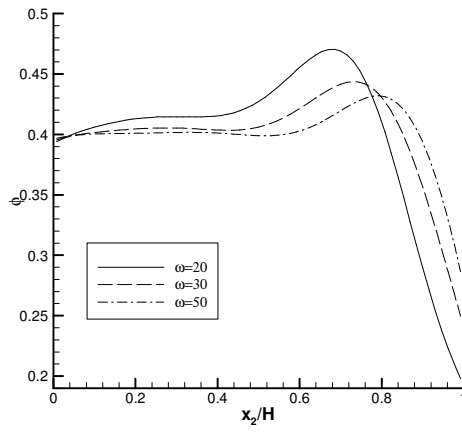


Figure. 6.12. Concentration profiles at average volume fraction, $\phi = 0.4$ after $N=50000$ oscillations.

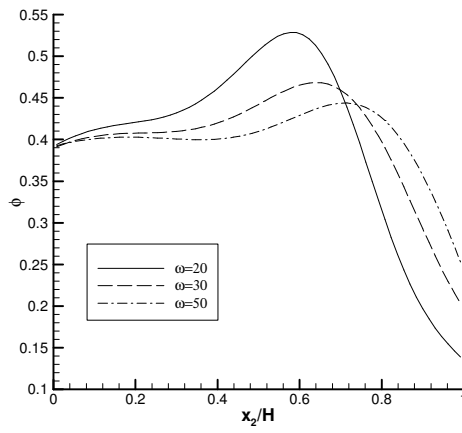


Figure. 6.13. Concentration profiles at average volume fraction, $\phi = 0.4$ after $N=150000$ oscillations.

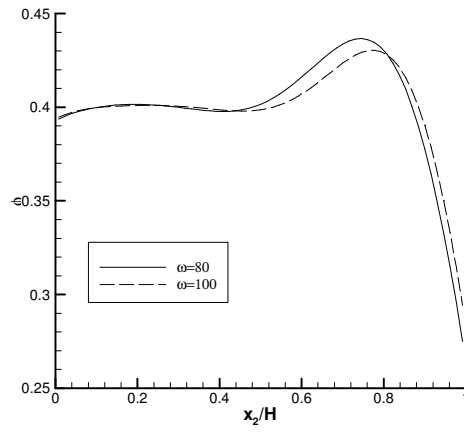


Figure. 6.14. Concentration profiles at average volume fraction, $\phi = 0.4$ after $N=200000$ oscillations.

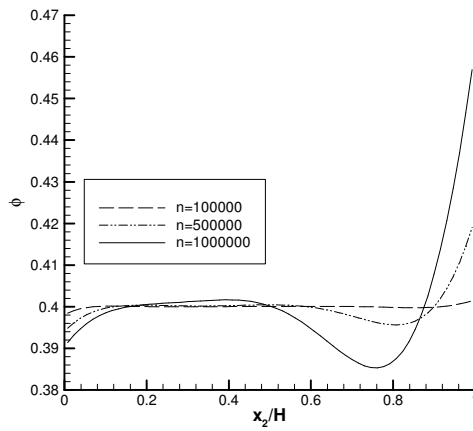


Figure. 6.15. Concentration profiles at average volume fraction, $\phi = 0.4$ for $\hat{\omega} = 250$.

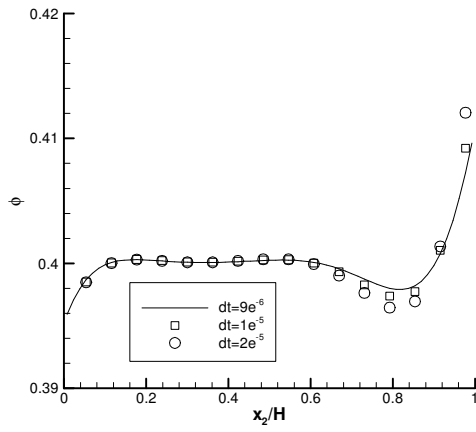


Figure. 6.16. Time step size dependency on the solution for $\hat{\omega} = 250$ after $N=10^5$ cycles.

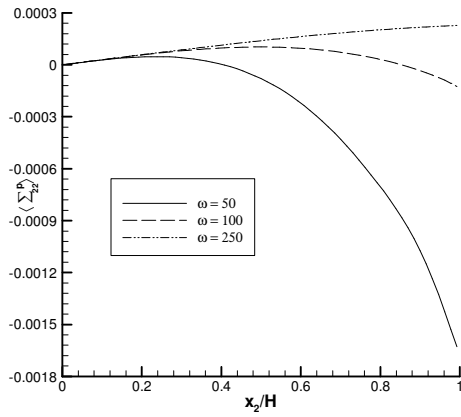


Figure. 6.17. Time averaged values of $\langle \hat{\Sigma}_{22}^P \rangle$ for $\hat{\omega} = 50$, $\hat{\omega} = 100$ and $\hat{\omega} = 250$ after $N=10^4$ cycles.

CHAPTER 7

CONCLUSIONS

In this study numerical calculations are carried out for steady laminar flows of both Newtonian and non-Newtonian fluids. Oldroyd-B, Phan-Thien Tanner (PTT) and White-Metzner constitutive models are used to capture viscoelasticity. Flows are simulated at various Reynolds and Weissenberg numbers and polymer viscosity, w_r by utilizing the finite volume method on a uniform and non-uniform graded collocated grid systems. Convective terms in the momentum equations are treated by using first order upwind, power-law second order central differences and QUICK schemes. Upwind and QUICK approximations are employed for the viscoelastic stresses. The semi-implicit method for the pressure-linked equation (SIMPLE) and SIMPLE consistent (SIMPLEC) are used to solve the coupled continuity, momentum and constitutive equations. Extra stress terms in momentum equations are solved by decoupled strategy. The code is applied to three different test cases: a) laminar steady flow in planar channel entrance, b) laminar steady flow around stick-slip and c) laminar steady flow in lid-driven square cavity. The results obtained in this study allow one to draw the following conclusions:

1. Numerically it is possible to obtain steady solutions of lid-driven cavity flow at high Reynolds numbers up to 40000 even with coarse grids of 257x257.
2. If Reynolds number increases, convective terms become dominant in the momentum equations; hence additional pressure correction inner loop cycle is required to satisfy continuity equation. For example, for Reynolds number 25000, six inner cycle iterations are needed to obtain convergence solution.
3. Our analysis shows that momentum interpolation method (MIM) should be used instead of the simple linear interpolation to evaluate coefficients in the constitutive equations and to obtain velocity gradients because of the robustness. However near the boundary they should be calculated at least by introducing a second order polynomial.

4. Detailed examination of the numerical solutions of the flow in channel of planar entrance flow has revealed that all schemes result in almost the same results and they require nearly the same iteration numbers for an Oldroyd-B fluid at $Re \ll 1$. However, QUICK scheme is the most expensive one in all schemes in terms of computing requirements. At this creeping flow condition maximum attainable Weissenberg number is 1 for all schemes.
5. It is also shown that maximum attainable value of Weissenberg number is dependent on Reynolds number as well as the used constitutive model. However all constitutive models used in the simulation of channel flow suffered from instabilities at high Weissenberg number.
6. In stick-slip flow, as the value of Weissenberg number increases, the slope of velocity profiles decreases at top boundary and the magnitude of the normal and shear stresses at singularity point grow enormously. These large stresses peaks cause large oscillation in the velocity and stress field.
7. The convergence of the numerical scheme is found to be very sensitive to mesh refinement. For instance as number of the grid points increase, attainable maximum Weissenberg number decreases.
8. An opposed to the Oldroyd-B fluid model, the velocity profile of White-Metzner and PTT models show overshoot and undershoot along the top and centerline of the stick-slip. In addition, White-Metzner model predicts much higher stress peaks at the singularity point than PTT model but lower than Oldroyd-B model.
9. With respect to attainable maximum value of Weissenberg number as well as smooth solutions, the White-Metzner model seems to yield smoother solutions at much higher Weissenberg number than Oldroyd-B and PTT models.
10. Attainable maximum value of Weissenberg number is very sensitive to polymer viscosity as well as Reynolds number. Upstream secondary eddy (USE) and downstream secondary eddy (DSE) sizes are also strongly affected by the value of polymer contributed viscosity. For instance at creeping flow condition ($Re \ll 1$) and small Reynolds number ($Re=100$) DSE and USE sizes decrease with increasing Weissenberg number. However, at moderately large value of Reynolds number ($Re=400$), DSE and USE come together and form second loop at the bottom of the cavity at Weissenberg number 0.3. However when Weissenberg number is greater than 0.3, DSE and USE shrink and become similar to the those at low Reynolds numbers.

11. Dimensionless magnitude of normal stress near the downstream increases with increasing Weissenberg number for all Reynolds numbers. On the other hand at a fixed Weissenberg number magnitude of the stress decreases as Reynolds number increases.
12. Under steady conditions, the SPP model predicts that the resulting migration causes particles to the center of the channel where the concentration approaches the maximum packing for hard sphere suspensions.
13. In oscillatory flow, the behavior depends strongly on the amplitude of the strain. For oscillations with large strains, the particles migrate to the channel center. However, when the strain is small, the maximum concentration is located either at a position between the channel center and walls, or in the limit of very small strains, at the wall.

REFERENCES

- [1] R.E. Evans and K. Walters, Further remarks on the lip-vortex mechanism of vortex enhancement in planar-contraction flows, *J. Non-Newtonian Fluid Mech.*, 32 (1989) 95.
- [2] R.E. Evans and K. Walters, Flow characteristic associated with abrupt changes in geometry in the case of highly elastic liquid, *J. Non-Newtonian Fluid Mech.*, 20 (1986) 11.
- [3] D.V. Boger, D.U. Hur and R.J. Binnington, Further observations of elastic effects in tubular entry flows, *J. Non-Newtonian Fluid Mech.*, 20 (1986) 31.
- [4] B. Pak, U.I. Cho and S. U.S. Choi, Separation and reattachment of non-Newtonian fluid flows in a sudden expansion pipe, *J. Non-Newtonian Fluid Mech.*, 37 (1990) 175.
- [5] Y.C. Zhou, B.S.V. Patnaik, D.C. Wan and G.W. Wei, DSC solution for flow in a staggered double lid driven cavity, *Int. J. Numer. Meth. Engng.*, 57 (2003) 211.
- [6] M.S. Darwish and J.R. Whiteman, Numerical modeling of viscoelastic liquids using a finite-volume method, *J. Non-Newtonian Fluid Mech.*, 45 (1992) 311-337.
- [7] R. Keunings, On the high Weissenberg number problem, *J. Non-Newtonian Fluid Mech.*, 20 (1986) 209-226.
- [8] M. Fortin, A new approach for the FEM simulation of viscoelastic flows, *J. Non-Newtonian Fluid Mech.*, 32 (1989) 295-310.
- [9] A.R. Davies, Numerical filtering and the high Weissenberg number problem, *J. Non-Newtonian Fluid Mech.*, 16 (1984) 195-209.
- [10] B. Debbaut, J.M. Marchal and M.J. Crochet, Numerical simulation of highly viscoelastic flows through an abrupt contraction, *J. Non-Newtonian Fluid Mech.*, 29 (1988) 119-146.

- [11] P. Saramito, Efficient simulation of nonlinear viscoelastic fluid flows, *J. Non-Newtonian Fluid Mech.*, 60 (1995) 199-223.
- [12] M.R. Apelian, R.C. Armstrong and R.A. Brown, Impact of the constitutive equation and singularity on the calculation of stick-slip flow: The modified Upper-Convected Maxwell model, *J. Non-Newtonian Fluid Mech.*, 27 (1988) 299-321.
- [13] G.P. Sasmal, A finite volume approach for calculation of viscolastic flow through an abrupt axisymmetric contraction, *J. Non-Newtonian Fluid Mech.*, 56 (1995) 15-47.
- [14] D.D. Joseph, M. Renardy, J.-C. Saut, Hyperbolicity and change of type in the flow of viscoelastic fluids, *Mech. Anal.*, 87 (1985) 213-251.
- [15] J.Y. Yoo, D.D. Joseph, Hyperbolicity and change of type in the flow of viscoelastic fluids through channels, *J. Non-Newtonian Fluid Mech.*, 19 (1985) 15-41.
- [16] T.B. Gasti, Steady flow of a non-Newtonian fluid through a contraction, *J. Comput. Phys.*, 27 (1975) 42.
- [17] M.J. Crochet and G. Pilate, Plane flow of a fluid of second grade through a contraction, *J. Non-Newtonian Fluid Mech.*, 1 (1976) 247.
- [18] H.C. Choi, J.H. Song and J.Y. Yoo, Numerical simulation of planar contraction flow of a Gieskus fluid, *J. Non-Newtonian Fluid Mech.*, 29 (1998) 347.
- [19] P.W. Chang, T.W. Patten and B.A. Finlayson, Collocation and Galerkin finite element methods for viscoelastic fluid flow, *Comput. Fluids*, 7 (1979) 267.
- [20] R.E. Gaidos and R. Darby, Numerical simulation and change in type in the developing flow of a nonlinear viscoelastic fluid, *J. Non-Newtonian Fluid Mech.*, 29 (1988) 59.
- [21] A.N. Beris, R.C. Armstrong and R.A. Brown, Spectral/finite element calculations of the flow of a Maxwell fluid between eccentric rotating cylinders, *J. Non-Newtonian Fluid Mech.*, 22 (1987) 129.
- [22] J.Y. Yoo and Y. Na, A numerical study of the planar contraction flow of a viscoelastic fluid using the SIMPLER algorithm, *J. Non-Newtonian Fluid Mech.*, 39 (1991) 89.

- [23] S.-C. Xue, N. Phan-Thien and R.I. Tanner, Numerical study of secondary flows of viscoelastic fluid in straight pipes by an implicit finite volume method, *J. Non-Newtonian Fluid Mech.*, 59 (1995) 191.
- [24] S.-C. Xue, N. Phan-Thien and R.I. Tanner, Three dimensional numerical simulations of viscoelastic flows through planar contractions, *J. Non-Newtonian Fluid Mech.*, 74 (1998) 195-245.
- [25] P.J. Oliveira, F.T. Pinho and G.A. Pinto, Numerical simulation of non-linear elastic flows with a general collocated finite-volume method, *J. Non-Newtonian Fluid Mech.* 79 (1998) 1-43.
- [26] X. Huang, N. Phan-Thien and R.I. Tanner, Viscoelastic flow between eccentric rotating cylinders: unstructured control volume method, *J. Non-Newtonian Fluid Mech.*, 64 (1996) 71.
- [27] R.I. Tanner and S-C. Xue, Computing transient flows with high elasticity, *Korea-Australia Rheology Journal*, 14 (2002) 143-159.
- [28] H.A. Moatassime and D. Esselaoui, A finite volume approach for unsteady viscoelastic fluid flows, *Int. J. Numer. Meth. Fluids*, 39 (2002) 939-959.
- [29] M. Peric, R. Kesser and G. Scheuerer, Comparison of finite volume numerical methods with staggered and collocated grids, *Computers & Fluids*, 16 (1988) 389-403.
- [30] A.W. Date, Solution of Navier-Stokes equations on non-staggered grid, *Int. J. Heat Mass Transfer*, 36 (1993) 1913-1922.
- [31] C.M. Rhie and W.L. Chow, Numerical study of the turbulent flow past an airfoil with trailing Edge Separation, *AIAA J.*, 21 (11) (1983) 1525-1532.
- [32] S. Majumdar, Role of underrelaxation in momentum interpolation for calculation of flow with nonstaggered grids, *Numerical Heat Transfer*, 13 (1988) 125-132.
- [33] B. Yu, W. – Q. Tau, J.-J. Wei, Y. Kawaguchi, T. Tagawa and H. Ozoe, Discussion on momentum interpolation method for calculated grids of incompressible flow, *Numerical Heat Transfer, Part B*, 42 (2002) 141-166.

- [34] M.A. Alves, F.T. Pinho and P.J. Oliveira, Effect of a high-resolution differencing scheme on finite-volume prediction of viscoelastic flows, *J. Non-Newtonian Fluid Mech.* 93 (2000) 287-314.
- [35] M.A. Alves, F.T. Pinho and P.J. Oliveira, The flow of viscoelastic fluids past a cylinder: finite volume high-resolution methods, *J. Non-Newtonian Fluid Mech.* 97 (2001) 207-232.
- [36] S.S. Edussuriya, A.J. Williams and C. Bailey, A cell-centred finite volume method for modeling viscoelastic flow, *J. Non-Newtonian Fluid Mech.* 117 (2004) 47-61.
- [37] D.B. Spalding, A novel finite difference formulation for differential expressions involving both first and second derivatives, *Int. J. Num. Methods Eng.*, 4 (1972) 551.
- [38] S.V. Patankar, *Numerical Heat Transfer and Fluid Flow*, McGraw-Hill, New York, 1980.
- [39] G.D. Raithby, Skew upwind differencing schemes for problems involving fluid flow, *Comput. Methods Appl. Mech. Eng.*, 19 (1976) 153.
- [40] W. Shyy, S. Thakur and J. Wright, Second order upwind and central difference schemes for recirculating flow computation, *AIAA J.*, 30(1999) 923.
- [41] B.P. Leonard, A stable and accurate convective modelling procedure based on quadratic upstream interpolation, *Comput. Methods Appl. Mech. Eng.*, 19 (1979) 59.
- [42] P.H. Gaskell and A.K.C. Lau, Curvature-compensated convective transport: SMART, a new boundedness-preserving transport algorithm, *Int. J. Num. Methods Fluids*, 8 (1988) 617.
- [43] T. Cochrane, K. Walters and M.F. Webster, On Newtonian and non-Newtonian flow in complex geometries, *Phil. Trans. R. Soc. Lond. A* 301, 163 (1981) 163.
- [44] M.A. Mendelson, P.-W. Yeh, R.A. Brown and R.C. Armstrong, Approximation error in finite element calculations of viscoelastic fluid flows, *J. Non-Newtonian Fluid Mech.*, 10 (1982) 31.
- [45] P. Pakdel, S.H. Spiegelberg and G.H. McKinley, Cavity flows of elastic liquids: Two-dimensional flows, *Phys. Fluids* 9 (11), (1997) 3123.

- [46] P. Pakdel and G. H. McKinley, Cavity flows of elastic liquids: Purely elastic instabilities, *Phys. Fluids*, 10 (1998) 1058.
- [47] A.M. Grillet, B. Yang, B. Khomami and E.S.G. Shaqfeh, Modelling of viscoelastic lid driven cavity flow using finite element simulations, *J. Non-Newtonian Fluid Mech.*, 88 (1999) 99.
- [48] A.M. Grillet, E.S.G. Shaqfeh and B. Khomami, Observations of elastic instabilities in lid-driven cavity flow, *J. Non-Newtonian Fluid Mech.*, 94 (2000) 15.
- [49] R. Fattal and R. Kupferman, Time dependent simulation of viscoelastic flows at high Weissenberg number using the log-conformation representation, *J. Non-Newtonian Fluid Mech.*, 126 (2005) 23.
- [50] R.B. Bird, R.C. Armstrong, O. Hassager, *Dynamics of Polymeric Liquids*, vol. 1. Fluid Mechanics, Wiley USA, (1987).
- [51] Y. Na and J.Y. Yoo, A finite volume technique to simulate the flow of a viscoelastic fluid, *Computational Mechanics.*, 8 (1991) 43-55.
- [52] N. Phan-Thien and R.I. Tanner, A new constitutive equation derived from network theory, *J. Non-Newtonian Fluid Mech.*, 2 (1977) 353-365.
- [53] D.O.A. Cruz, F.T. Pinho and P.J. Oliveira, Analytical solution for fully developed laminar flow of some viscoelastic liquids with a Newtonian solvent contribution, *J. Non-Newtonian Fluid Mech.* 132 (2005) 28-35.
- [54] A. Hakim, Existence of slow steady flows of viscoelastic fluids of White-Metzner type, *Computers and Mathematics with Applications*, 38 (1999) 239-247.
- [55] S. Raghay and A. Hakim, Numerical simulation of White-Metzner fluid in a 4:1 contraction, *Int. J. Numer. Meth. Fluids*, 35 (2001) 559-573.
- [56] H.K. Versteeg and W. Malalasekera, *An introduction to computational fluid dynamics: The finite volume method*, Prentice Hall, 1995.
- [57] R. Courant, E. Isaacson and M. Rees, On the solution of non-linear hyperbolic differential equations by finite differences, *Comm. Pure Appl. Math.*, 5 (1950) 243.

- [58] H.A. Moatassime and D. Esselaoui, A. Hakim and S. Raghay, Finite volume multigrid method of the planar contraction flow of a viscoelastic fluid, *Int. J. Numer. Meth. Fluids*, 36 (2001) 885-902.
- [59] S.V. Patankar and D.B. Spalding, A calculation procedure for heat, mass and momentum transfer in three-dimensional parabolic flows, *International Journal for Heat and Mass Transfer*, 15 (1972) 1787.
- [60] J.P. Van Doormal, G.D. Raithby, Enhancement of the SIMPLE method for predicting incompressible flows, *Numer. Heat Transfer*, 7 (1984) 147.
- [61] R.I. Issa, Solution of implicitly discretized fluid flow equation by Operator-Splitting, *J. Comput. Phys.*, 62 (1985) 40.
- [62] E. Erturk, T.C. Corke and C. Gokcol, Numerical solutions of 2-D steady incompressible driven cavity flow at high Reynolds numbers, *Int. J. Numer. Meth. Fluids*, 48 (2005) 747-774.
- [63] E. Erturk, and C. Gokcol, Fourth-order compact formulation of Navier-Stokes equations and driven cavity flow at high Reynolds numbers, *Int. J. Numer. Meth. Fluids*, 50 (2005) 421-436.
- [64] E. Erturk, Discussion on driven cavity flow and steady solutions at high Reynolds numbers, Submitted.
- [65] M. Sahin and R.G. Owens, A novel fully implicit finite volume method applied to the lid-driven cavity problem- Part I: High Reynolds number flow calculations, *Int. J. Numer. Fluids*, 42 (2003) 57-77.
- [66] U. Ghia, K.N. Ghia and C.T. Shin, High-Re solutions for incompressible flow using the Navier-Stokes equations and a multigrid method, *J. Comput. Phys.*, 48 (1982) 387-411.
- [67] O. Botella and R. Peyret, Benchmark spectral results on the lid-driven cavity flow, *Computers & Fluids* 27(4) (1998) 421-433.
- [68] C.-H. Bruneau and C. Jouron, An efficient scheme for solving steady incompressible Navier-Stokes equations, *Journal of Computational Physics*, 89(2) (1990) 389-413.

- [69] E. Barragy, G.F. Carey, Stream function-vorticity driven cavity solutions using p finite elements, *Computers & Fluids*, 26 (1997) 453-468.
- [70] S.J. Liao, Higher-order stream function-vorticity formulation of 2-D steady Navier-Stokes equations, *Int. J. Numer. Fluids*, 15 (1992) 595-612.
- [71] Q-H. Deng and G-F. Tang, Special treatment of pressure correction based on continuity conservation in a pressure based algorithm, *Numer. Heat Transfer, Part B*, 42 (2002) 73-92.
- [72] M.D. Waters, M.J. King, Unsteady flow of an elastico-viscos liquid, *Rheol. Acta*, 9 (1970) 345.
- [73] J. Rosenberg, Numerical integration of differential viscoelastic models, *J. Non-Newtonian Fluid Mech.*, 39 (1991) 269-290.
- [74] P. T. F. Baaijens, Numerical experiments with a Discontinuous Galerkin method including monotonicity enforcement on the stick-slip, *J. Non-Newtonian Fluid Mech.*, 51 (1994) 141-159.
- [75] Chin-Chin Tsai, Ta-Ju Liu, Comparison of three solvers for viscoelastic fluid flow problems, *J. Non-Newtonian Fluid Mech.*, 60 (1995) 155-177.
- [76] H. A. Moatassime, C. Jouron, A multigrid method for solving steady viscoelastic fluid flow, *Comput. Methods Appl. Mech. Engrg.*, 190 (2001) 4061-4080.
- [77] J. J. Stickel, The modeling of microstructure and total stress in particulate suspensions, Ph. D Thesis, University of California Davis (2006).
- [78] F. Gadala-Maria, A. Acrivos, Shear-induced structure in a concentrated suspension of solid spheres, *J. Rheol.* 24 (1980) 799-814.
- [79] V. Breedveld, D. van den Ende, R. Jongschaap, Shear-induced diffusion and rheology of noncolloidal suspensions: Time scales and particle displacements, *J. Chem. Phys.* 114 (2001) 5923-5936.
- [80] T. Narumi, H. See, Y. Honma, T. Hasegawa, T. Takahashi, N. Phan-Thien, Transient response of concentrated suspensions after shear reversal, *J. Rheol.* 46 (2002) 295-305.

- [81] V. G. Kolli, E. J. Pollauf, F. Gadala-Maria, Transient normal stress response in concentrated suspension of spherical particles, *J. Rheol.* 46 (2002) 321-334.
- [82] I. Zarraga, D. A. Hill, D.T. Leighton, The characterization of the total stress response in concentrated suspensions of noncolloidal spheres in Newtonian fluids, *J. Rheol.* 44 (2000) 185-220.
- [83] D. R. Foss, J. F. Brady, Structure diffusion and rheology of Brownian suspensions by stokesian dynamics, *J. Fluid Mech.* 181 (1987) 415-439.
- [84] D. Leighton, A. Acrivos, The shear-induced migration of particles in concentrated suspensions, *J. Fluid Mech.* 181 (1987) 415-439.
- [85] R. J. Phillips, R. C. Armstrong, R. A. Brown, A. L. Graham, J. R. Abbott, A constitutive equation for concentrated suspensions that accounts for shear-induced particle migration. *Phys. Fluids A* 4 (1992) 30-40.
- [86] C. J. Koh, P. Hookham, L. G. Leal, An experimental investigation of concentrated suspension flow rectangular channel, *J. Fluid Mech.* 266 (1994) 1-32.
- [87] M. K. Lyon, L. G. Leal, An experimental study of the motion of concentrated suspensions in two-dimensional channel flow. Part 1. Monodisperse systems, *J. Fluid Mech.* 363 (1998) 25-56.
- [88] J. E. Butler, P. D. Majors, R. T. Bonnecaze, Observation of shear-induced particle migration for oscillatory flow of a suspension within a tube. *Phys. Fluids* 11 (1999) 2865-2877.
- [89] A. M. Corbett, R. J. Phillips, R. J. Kauten, K. L. McCarthy, Magnetic resonance imaging of concentration and velocity profiles of pure fluids and solid suspensions in rotating geometries, *J. Rheol.* 39 (1995) 907-924.
- [90] P. R. Nott, J. F. Brady, Pressure-driven flow of suspensions. Simulation and theory, *J. Fluid Mech.* 275 (1994) 157-199.
- [91] N. C. Shapley, R. A. Brown, R. C. Armstrong, Laser Doppler velocimetry measurements of particle velocity fluctuations in a concentrated suspension, *J. Rheol.* 46 (2002) 241-272.

- [92] J. F. Morris, F. Boulay, Curvilinear flows of noncolloidal suspensions: The role normal stresses, *J. Rheol.* 43 (1999) 1213-1237.
- [93] R. M. Miller, J. F. Morris, Normal stress-driven migration and axial development in pressure-driven flow of concentrated suspensions, *J. Non-Newtonian Fluid Mech.* 135 (2006) 149-165.
- [94] N. Phan-Thien, Constitutive equation for concentrated suspensions in Newtonian liquids, *J. Rheol.* 39 (1995) 679-695.
- [95] J. Goddard, A dissipative anisotropic fluid model for non-colloidal particle dispersions, *J. Fluid Mech.* 568 (2006) 1-17.
- [96] J. J. Stickel, R. J. Phillips, R. L. Powell, A constitutive equation for microstructure and total stress in concentrated suspensions, *J. Rheol.* 50 (2006) 379-413.
- [97] J. J. Stickel, R. J. Phillips, R. L. Powell, Application of a constitutive model for particulate suspensions: Time dependent viscometric flows, *J. Rheol.* 51 (2007) 1271-1302.
- [98] J. F. Brady, J. F. Morris, Microstructure of strongly sheared suspensions and its impact on rheology and diffusion, *J. Fluid Mech.* 348 (1980) 103-139.
- [99] J. F. Brady, I. Carpen, Second normal stress jump instability in non-Newtonian fluids, *J. Non-Newtonian Fluid Mech.* 102 (2002) 219-232.
- [100] J. F. Morris, Anomalous migration in simulated oscillatory pressure-driven flow of a concentrated suspension, *Phys. Fluids.* 13 (2001) 2457-2462.
- [101] A. Einstein, *Investigation on the Theory of the Brownian Movement*, Dover, New York, 1956.
- [102] S. I. Madanshetty, A. Nadim, H. A. Stone, Experimental measurement of shear-induced diffusion in suspension using long-time data, *Phys. Fluids.* 9 (1996) 2011-2018.
- [103] H. J. M. Hanley, J. C. Rainwater, S. Hess, Shear-induced angular dependence of the liquid pair correlation function, *Phys. Rev. A* 36 (1987) 1795-1802.
- [104] C. Truesdell, W. Noll, *The Non-Linear Field Theories of Mechanics*, Springer-Verlag, New York, 2004

- [105] R. R. Huilgol, N. Phan-Thien, Fluid Mechanics of Viscoelasticity, Elsevier, Amsterdam, 1997.
- [106] L. G. Leall, Laminar Flow and Convective Transport Processes, Butterworth-Heinemann, Boston, 1992.
- [107] J. J. D. Anderson, Computational Fluid Dynamics: The Basics with Applications, McGraw Hill, New York, 1994.
- [108] W. H. Press, B. P. Flannery, S. A. Teukolsky, W. T. Vetterling, Numerical Recipes, Cambridge University Press, New York, 1989.
- [109] R. R. Huilgol, N. Phan-Thien, Fluid Mechanics of Viscoelasticity, Elsevier, Amsterdam, 1997.
- [110] S. E. Phan, D. Leighton, Measurement of the shear-induced tracer diffusivity in concentrated suspensions, (1993), J. Fluid Mech., submitted.

CURRICULUM VITAE

PERSONAL INFORMATION

Surname, Name: Yapıcı, Kerim
Nationality: Turkish (TC)
Marital Status: Married
Phone: +90 312 210 43 84
Fax: +90 312 210 26 00

EDUCATION

| Degree | Institution | Year of Graduation |
|--------|------------------------------|--------------------|
| Master | METU, Chemical Engineering | 2003 |
| BS | Ankara, Chemical Engineering | 1998 |

WORK EXPERIENCE

| Year | Place | Enrollment |
|--------------|------------------------------|--------------------|
| 2001-Present | Ankara, Chemical Engineering | Teaching Assistant |
| 2000-2001 | Land Logistic Command | Lieutenant |

ABROAD EXPERIENCE

| Place | Project | Year |
|------------------------------------|------------------------------------------------------------------------------------|-----------------------|
| The University of California Davis | Particle migration and suspension structure in steady and oscillatory channel flow | April 2007-April 2008 |

PUBLICATIONS

1. Yapıcı, K., Powell, R. L., Phillips, R. J., Particle migration and suspension structure in steady and oscillatory plane Poiseuille flow, Physics of Fluids, submitted.
2. Yapıcı, K., Karasözen, B., Schäfer, M., Uludag, Y., Numerical Investigation of the effect of the Rushton type turbine design factors on agitated tank flow characteristics, Chemical engineering and Processing, 47, (2008), 1346-1355.

3. Uğur Ö., Karasözen, B., Schäfer, M., and Yapici, K., Derivative Free Optimization Methods for Optimizing Stirrer Configurations, *European Journal of Operational Research*, 191 (2008) 855-863.
4. Schäfer, M., Karasözen, B., Uludag, Y., Yapici, K., and Uğur Ö., Numerical method for optimizing stirrer configurations, *Computers and Chemical Engineering*, 30, (2005) 183-190.
5. Schäfer M., Karasözen B., Uğur Ö., and Yapıcı K., Derivative Free Optimization of Stirrer Configurations, *ENUMATH*, 981-988, 2005.